The Astrophysical Journal, 927:9 (49pp), 2022 March 1 https://doi.org/10.3847/1538-4357/ac474f

The Gas–Star Formation Cycle in Nearby Star-forming Galaxies. II. Resolved Distributions of CO and Hα Emission for 49 PHANGS Galaxies

Hsi-An Pan, (潘璽安)[1,2], Eva Schinnerer[1], Annie Hughes[3], Adam Leroy[4], Brent Groves[5], Ashley Thomas Barnes[6], Francesco Belfiore[7], Frank Bigiel[6], Guillermo A. Blanc[8,9], Yixian Cao[10], Mélanie Chevance[11], Enrico Congiu[9], Daniel A. Dale[12], Cosima Eibensteiner[6], Eric Emsellem[13,14], Christopher M. Faesi[15], Simon C. O. Glover[16], Kathryn Grasha[17], Cinthya N. Herrera[18], I-Ting Ho[1], Ralf S. Klessen[16,19], J. M. Diederik Kruijssen[11], Philipp Lang[1], Daizhong Liu[1], Rebecca McElroy[20], Sharon E. Meidt[21], Eric J. Murphy[22], Jérôme Pety[18,23], Miguel Querejeta[24], Alessandro Razza[9], Erik Rosolowsky[25], Toshiki Saito[1], Francesco Santoro[1], Andreas Schruba[26], Jiayi Sun[4], Neven Tomičić[27], Antonio Usero[24], Dyas Utomo[22], and Thomas G. Williams[1]

[1] Max-Planck-Institut für Astronomie, Königstuhl 17, D-69117 Heidelberg, Germany; hapan@gms.tku.edu.tw
[2] Department of Physics, Tamkang University, No.151, Yingzhuan Road, Tamsui District, New Taipei City 251301, Taiwan
[3] CNRS, IRAP, Av. du Colonel Roche BP 44346, F-31028 Toulouse cedex 4, France
[4] Department of Astronomy, The Ohio State University, 140 West 18th Avenue, Columbus, OH 43210, USA
[5] International Centre for Radio Astronomy Research, The University of Western Australia, Crawley, WA 6009, Australia
[6] Argelander-Institut für Astronomie, Universität Bonn, Auf dem Hügel 71, D-53121, Bonn, Germany
[7] INAF—Osservatorio Astrofisico di Arcetri, Largo E. Fermi 5, I-50157, Firenze, Italy
[8] Observatories of the Carnegie Institution for Science, 813 Santa Barbara Street, Pasadena, CA 91101, USA
[9] Departamento de Astronomía, Universidad de Chile, Camino del Observatorio 1515, Las Condes, Santiago, Chile
[10] Aix Marseille Université, CNRS, LAM (Laboratoire d'Astrophysique de Marseille), F-13388 Marseille, France
[11] Astronomisches Rechen-Institut, Zentrum für Astronomie der Universität Heidelberg, Mönchhofstraße 12-14, D-69120 Heidelberg, Germany
[12] Department of Physics and Astronomy, University of Wyoming, Laramie, WY 82071, USA
[13] European Southern Observatory, Karl-Schwarzschild Straße 2, D-85748 Garching bei München, Germany
[14] Univ Lyon, Univ Lyon 1, ENS de Lyon, CNRS, Centre de Recherche Astrophysique de Lyon UMR5574, F-69230 Saint-Genis-Laval, France
[15] University of Massachusetts—Amherst, 710 N. Pleasant Street, Amherst, MA 01003, USA
[16] Universität Heidelberg, Zentrum für Astronomie, Institut für Theoretische Astrophysik, Albert-Ueberle-Str 2, D-69120 Heidelberg, Germany
[17] Research School of Astronomy and Astrophysics, Australian National University, Canberra, ACT 2611, Australia
[18] Institut de Radioastronomie Millimétrique (IRAM), 300 Rue de la Piscine, F-38406 Saint Martin d'Hères, France
[19] Universität Heidelberg, Interdisziplinäres Zentrum für Wissenschaftliches Rechnen, Im Neuenheimer Feld 205, D-69120 Heidelberg, Germany
[20] Sydney Institute for Astronomy, School of Physics A28, The University of Sydney, NSW 2006, Australia
[21] Sterrenkundig Observatorium, Universiteit Gent, Krijgslaan 281 S9, B-9000 Gent, Belgium
[22] National Radio Astronomy Observatory, 520 Edgemont Road, Charlottesville, VA 22903-2475, USA
[23] Sorbonne Université, Observatoire de Paris, Université PSL, CNRS, LERMA, F-75014, Paris, France
[24] Observatorio Astronómico Nacional (IGN), C/Alfonso XII, 3, E-28014 Madrid, Spain
[25] Department of Physics, University of Alberta, Edmonton, AB T6G 2E1, Canada
[26] Max-Planck-Institut für extraterrestrische Physik, Giessenbachstraße 1, D-85748 Garching, Germany
[27] INAF-Osservatorio Astronomico di Padova, Vicolo Osservatorio 5, I-35122 Padova, Italy
Received 2021 June 7; revised 2021 December 27; accepted 2021 December 29; published 2022 March 2

Abstract

The relative distribution of molecular gas and star formation in galaxies gives insight into the physical processes and timescales of the cycle between gas and stars. In this work, we track the relative spatial configuration of CO and Hα emission at high resolution in each of our galaxy targets and use these measurements to quantify the distributions of regions in different evolutionary stages of star formation: from molecular gas without star formation traced by Hα to star-forming gas, and to H II regions. The large sample, drawn from the Physics at High Angular resolution in Nearby GalaxieS ALMA and narrowband Hα (PHANGS-ALMA and PHANGS-Hα) surveys, spans a wide range of stellar masses and morphological types, allowing us to investigate the dependencies of the gas–star formation cycle on global galaxy properties. At a resolution of 150 pc, the incidence of regions in different stages shows a dependence on stellar mass and Hubble type of galaxies over the radial range probed. Massive and/or earlier-type galaxies in our sample exhibit a significant reservoir of molecular gas without star formation traced by Hα, while lower-mass galaxies harbor substantial H II regions that may have dispersed their birth clouds or formed from low-mass, more isolated clouds. Galactic structures add a further layer of complexity to the relative distribution of CO and Hα emission. Trends between galaxy properties and distributions of gas traced by CO and Hα are visible only when the observed spatial scale is $\ll$500 pc, reflecting the critical resolution requirement to distinguish stages of the star formation process.

Unified Astronomy Thesaurus concepts: Galaxies (573); Interstellar medium (847)

1. Introduction

The conversion from gas to stars is a complex process that ultimately determines many observed properties of a galaxy, such as its observed morphology at different wavelengths and stellar mass. In star-forming galaxies, stars form through the collapse of

dense cores inside giant molecular clouds (GMCs). Therefore, the rate at which stars form is determined by the properties of GMCs, such as their level of turbulence, chemical composition, strength and structure of magnetic fields, or the flux of cosmic rays (Mac Low & Klessen 2004; McKee & Ostriker 2007).

Schmidt (1959) observed a tight correlation between the star formation rate (SFR) and the volume density of gas in the Milky Way. Later on, Kennicutt (1998) showed that the SFR and gas surface densities ($\Sigma_{\rm SFR}$ and $\Sigma_{\rm gas}$) are tightly correlated on the scales of integrated galaxies, a relationship that is now known as the Kennicutt–Schmidt relation. Many recent studies have shown that the Kennicutt–Schmidt relation, at least when considering the surface density of molecular gas ($\Sigma_{\rm H_2}$), holds down to kiloparsec scales, but with significant variation among galaxies (e.g., Bigiel et al. 2008; Leroy et al. 2008, 2013; Schruba et al. 2011; Momose et al. 2013). The Kennicutt–Schmidt relation has also become a commonly used prescription for implementing star formation in numerical simulations of galaxies (e.g., Katz 1992; Teyssier 2002; Schaye et al. 2015).

However, cloud-scale ($\sim$100 pc) observations in the Local Group and a few nearby star-forming galaxies reveal that the relationship between cold gas and stars is more complex. The correlation between $\Sigma_{\rm SFR}$ and $\Sigma_{\rm H_2}$ develops considerable scatter when the spatial resolution is sufficiently high to spatially separate the individual elements of the surface densities: GMCs and star-forming (H II) regions (e.g., Onodera et al. 2010; Schruba et al. 2010; Kreckel et al. 2018; Querejeta et al. 2019). This breakdown of the scaling relation has been attributed to the evolution of GMCs (Schruba et al. 2010; Feldmann et al. 2011; Kruijssen & Longmore 2014). The separation between GMCs and star formation tracers is now regularly used as an empirical probe of the cycle between gas and star formation (Kawamura et al. 2009; Schruba et al. 2010; Kruijssen & Longmore 2014; Kruijssen et al. 2018), including the timescale of evolutionary cycling between GMCs and star formation (Kruijssen et al. 2019; Chevance et al. 2020; Kim et al. 2021) and the impact of destructive stellar feedback (e.g., photoionization, stellar winds, and supernova explosions) on the structure of interstellar medium (ISM) and future star formation (Barnes et al. 2020, 2021; Chevance et al. 2022).

Moreover, recent cloud-scale studies of extragalactic GMCs have found evidence that GMCs are diverse in their physical properties, such as surface density and dynamical state (Hughes et al. 2013; Colombo et al. 2014; Rosolowsky et al. 2021). Various environmental mechanisms, such as galactic shear, differential noncircular motions, gas flows along and through stellar dynamical structures (e.g., bars and spiral arms), and accretion flows (Klessen & Hennebelle 2010; Meidt et al. 2013, 2018; Colombo et al. 2018; Jeffreson & Kruijssen 2018; Jeffreson et al. 2020), determine when and which pockets of the GMCs collapse. Theoretical study predicts that these mechanisms have different timescales and cause the star formation process to vary from galaxy to galaxy and from place to place within a galaxy (Jeffreson et al. 2021). Therefore, to understand how star formation works in galaxies, a large sample size is indispensable to cover a range of galactic environments and ISM properties/conditions.

In our previous paper (Schinnerer et al. 2019, hereafter Paper I), we developed a simple, robust method that quantifies the relative spatial distributions of molecular gas and recent star formation, as well as the spatial scale dependence of the relative distributions. The method considers the presence or absence of molecular gas traced by CO emission and star formation traced by Hα emission in a given region (i.e., sight line or pixel) at a given observed resolution. The method was applied to eight nearby galaxies with $\sim$1″ resolution molecular gas observations from the Physics at High Angular resolution in Nearby GalaxieS survey (PHANGS; Leroy et al. 2021a, 2021c) and the PdBI Arcsecond Whirlpool Survey (PAWS; Schinnerer et al. 2013) that have matched-resolution narrowband Hα observations. However, most of the galaxies in Paper I have similar global properties—they are massive, star-forming, spiral galaxies.

Given that GMC properties vary between and within galaxies, we extend this work to link the gas–star formation cycle and several secular and environmental probes. In this paper, we apply the method to 49 galaxies with high-resolution CO and Hα observations selected from PHANGS. Galaxies in our extended sample cover a wider range in stellar mass (M_*) and morphology (Hubble type) compared to the galaxies in Paper I. The extended sample allows us to investigate how the distribution of different star formation phases—from non- or pre-star-forming gas, to star-forming clouds, and to regions forming massive stars—depends upon global galaxy properties (i.e., M_*, morphology, and dynamical structures). This is the first time that the relative distribution of molecular and ionized (Hα) gas has been quantified across such a large and diverse sample of galaxies at high resolution (150 pc). The resolution of 150 pc is sufficiently high to sample individual star-forming units and to separate such regions.

This paper is organized as follows. In Section 2, we describe the observations of molecular gas and star formation tracers, CO and Hα, respectively. Section 3 introduces the methodology for measuring the presence or absence of different tracers. Section 4 presents the distribution of molecular gas and star formation tracers as a function of galaxy properties and at a series of resolutions, from our 150 pc to 1.5 kpc. Section 5 discusses the main results. The conclusions are presented in Section 6.

2. Data

PHANGS[28] is a multiwavelength campaign to observe the tracers of the star formation process in a diverse but representative sample of nearby ($\lesssim$19 Mpc) low-inclination galaxies. The typical spatial resolution achieved with the multiwavelength observations is $\sim$100 pc. The combination of ALMA (Leroy et al. 2021a, 2021c), Very Large Telescope (VLT)/MUSE (Emsellem et al. 2021), narrowband Hα (A. Razza et al. 2022, in preparation), and HST (Lee et al. 2022) observations yields an unprecedented view of star formation at different phases, from gas to star clusters. The galaxies were selected to have $\log(M_*/M_\odot) \gtrsim 9.75$ and to be visible to ALMA, but with the current best approach for mass estimation, the sample extends down to $\log(M_*/M_\odot) \approx 9.3$. The galaxies are lying on or near the star-forming main sequence. More details on the survey design and scientific motivation are presented in Leroy et al. (2021c). In this work, we focus on the molecular gas and ionized (Hα) gas observed by the PHANGS-ALMA and PHANGS-Hα (narrowband) surveys, respectively.

[28] www.phangs.org

2.1. CO Images: PHANGS-ALMA

The 90 PHANGS-ALMA galaxies were observed in CO(2–1) using the ALMA 12 m and 7 m arrays and total-power antennas. The data were imaged in CASA (McMullin et al. 2007) version 5.4.0. We use the spectral line cubes delivered in the internal data release version 3.4. The data have native spatial resolutions of ∼25–180 pc, depending on the source distance. The typical 1σ noise level is ∼0.3 K per 2.5 km s^{-1} channel but varies slightly between galaxies. We use the "broad mask" integrated intensity maps. These maps include most CO emission (98% with a 5th–95th percentile range of 73%–100%) in the cube, meaning that they have high completeness. For full details of the sample, observing and reduction processes, and final data products, see Leroy et al. (2021a).

We create maps of molecular gas surface density (Σ_{H_2}) by applying a radially varying CO-to-H_2 conversion factor (α_{CO}) to the CO-integrated intensity map, following the method described in Sun et al. (2020a). We briefly summarize the steps here.

Many studies have shown that α_{CO} increases with decreasing metallicity (Z) (e.g., Wilson 1995; Arimoto et al. 1996; Leroy et al. 2011; Schruba et al. 2012). Our adopted radially varying α_{CO} takes into account the radial metallicity gradient of galaxies. The metallicity at one effective radius (R_e) in each galaxy is predicted according to the global M_* and the global M_*–Z relation reported by Sánchez et al. (2019) based on the Pettini and Pagel (2004) metallicity calibration. Then, the Z at $1R_e$ is extended to cover the entire galaxy assuming a universal radial metallicity gradient of -0.1 dex R_e^{-1} (Sánchez et al. 2014). Finally, α_{CO} at each galactocentric radius is calculated via the relation determined by Accurso et al. (2017):

$$\alpha_{CO} = 4.35\, Z'^{-1.6}\, M_\odot\ \mathrm{pc}^{-2}\ (\mathrm{K\ km\ s^{-1}})^{-1}, \quad (1)$$

where Z' is the local gas-phase abundance normalized to the solar value ($12 + \log[\mathrm{O/H}] = 8.69$; Asplund et al. 2009). Because α_{CO} is defined for the ^{12}CO($J = 1 \rightarrow 0$) transition, we apply a constant ^{12}CO($J = 2 \rightarrow 1$) to ^{12}CO($J = 1 \rightarrow 0$) brightness temperature ratio of $R_{21} = 0.65$. We do not account for galaxy-to-galaxy (and also inside a galaxy) variations in this ratio, which are typically ∼0.1 dex (Leroy et al. 2013, 2021b; den Brok et al. 2021; Yajima et al. 2021). We test our results against using a constant Galactic α_{CO} and discuss the choice of R_{21} in Appendices A.1 and A.2, respectively.

2.2. Hα Images: PHANGS-Hα

To create maps of recent star formation in our PHANGS galaxies, we obtained R-band and Hα-centered narrowband imaging for our sample. The 65 PHANGS-Hα galaxies were observed by the Wide Field Imager (WFI) instrument at the MPG-ESO 2.2 m telescope at the La Silla Observatory or by the Direct CCD at the Irénée du Pont 2.5 m telescope at the Las Campanas Observatory. Among the 65 galaxies, 32 were observed by the 2.2 m telescope and 36 by du Pont telescope, including 3 galaxies that were observed by both instruments. For galaxies with repeated observations, we use the observation that has the best spatial resolution. The field of view (FoV) of the WFI and du Pont observations are $34' \times 33'$ and $8\farcm5 \times 8\farcm5$, respectively. Full details of the observations, data reduction, and map construction can be found in A. Razza et al. (2022, in preparation). The images used in this work correspond to the internal release version 1.0 of the PHANGS-Hα survey. The main steps are summarized here (see also Paper I).

The data frames were astrometrically and photometrically calibrated using Gaia DR2 catalogs (Gaia Collaboration et al. 2018) cross-matched to all stars in the full FoV of the images. Typical seeing for the data is $\sim 1''$, and the final astrometric accuracy is $\lesssim 0\farcs1$. The sky background is computed in each exposure by masking all the sources $>2\sigma$ above the sigma-clipped mean, including an elliptical area around the galaxies based on the galaxy geometric parameters. A 2D plane is then fit to this background and subtracted, with this process occurring for each exposure frame. Each background-subtracted frame is then combined using inverse-variance weighting.

Then, the stellar continuum is subtracted from the combined images. The flux scale is determined using the median of the flux ratios for a selection of nonsaturated stars that are matched between the Hα and the R-band images. Using this flux ratio as a basis, we obtain a first estimate of the Hα + [N II] flux by subtracting the R-band image from the Hα + [N II] + continuum image.

However, the blended Hα + [N II] line also contributes to the R-band data. Using the estimated Hα + [N II] image, we determine the Hα + [N II] contribution to the R-band image. We subtract this estimated Hα + [N II] contamination from the R-band image and iterate this process until successive continuum estimates differ by less than 1%. Then, we subtract this continuum estimate to obtain a flux-calibrated line (H α + [N II]) image.

We correct the measured Hα flux for the loss due to the filter transmission, using the spectral shape of the narrowband filter and the position of the Hα line within the filter. We also correct for the contribution of the [N II] lines at 654.8 and 658.3 nm to the narrowband filter flux, assuming a uniform [N II]/Hα ratio of 0.3. This value is derived from high-spectral-resolution observations of H II regions in NGC 0628 with the VLT/MUSE instrument, with a typical scatter of ±0.1 (Kreckel et al. 2016; Santoro et al. 2021). We treat this as a characteristic spectrum for all of our targets but note the possible variation in [N II]/Hα as a source of uncertainty. Finally, we correct all images for foreground Galactic extinction using Schlafly & Finkbeiner (2011), who assume a Fitzpatrick (1999) reddening law with $R_V = 3.1$.

2.3. Sample Selection from PHANGS

The sample of galaxies used in this work is a subset of the full PHANGS-ALMA and PHANGS-Hα observations. Because our main analysis is performed at a fiducial resolution of 150 pc, the selected galaxies are required to be detected in both CO and Hα, and that a physical resolution better than 150 pc is achieved for both observations. Moreover, we only include galaxies that had been observed by all ALMA arrays (i.e., 12 m + 7 m + total power) by the time of internal data release v3.4. No additional cut (e.g., on M_*) is applied to the sample, besides the selection criteria that are inherited from the parent sample (see above). This results in a sample of 51 galaxies. Among these, NGC 2566 has many foreground stars that impact the reliability of the Hα data, and NGC 6744 has incomplete ALMA coverage. These two galaxies are therefore also excluded from our analysis, resulting in a final sample of 49 galaxies. Global properties of the sample are presented in Table 1.

Table 1
Galaxy Sample Used in This Work

Galaxy	(a) dist. (Mpc)	(b) incl. (°)	(c) R_{25} ($''$)	(d) log(SFR) ($M_\odot$ yr^{-1})	(e) log(M_*) ($M_\odot$)	(f) log(M_{H_2}) ($M_\odot$)	(g) log($M_{H\,I}$) ($M_\odot$)	(h) ΔMS	(i) T Type	(j) GD Spiral Arms	(k) bar
IC 1954	12.0	57.1	89.8	−0.52	9.6	8.7	9.0	−0.08	3.3	0	1
IC 5273	14.2	52.0	91.9	−0.28	9.7	8.6	9.0	0.08	5.6	0	1
NGC 0628	9.8	8.9	296.6	0.23	10.3	9.4	9.7	0.22	5.2	1	0
NGC 1087	15.9	42.9	89.1	0.11	9.9	9.2	9.0	0.34	5.2	0	1
NGC 1300	19.0	31.8	178.3	0.04	10.6	9.4	9.7	−0.19	4.0	1	1
NGC 1317	19.1	23.2	92.1	−0.4	10.6	8.9	...	−0.61	0.8	0	1
NGC 1365	19.6	55.4	360.7	1.22	10.9	10.3	9.9	0.79	3.2	1	1
NGC 1385	17.2	44.0	102.1	0.3	10.0	9.2	9.4	0.51	5.9	0	0
NGC 1433	12.1	28.6	185.8	−0.38	10.4	9.3	9.3	−0.51	1.5	1	1
NGC 1511	15.3	72.7	110.9	0.34	9.9	9.2	9.6	0.6	2.0	0	0
NGC 1512	17.1	42.5	253.0	−0.03	10.6	9.1	9.8	−0.25	1.2	1	1
NGC 1546	17.7	70.3	111.2	−0.11	10.3	9.3	8.7	−0.17	−0.4	1	0
NGC 1559	19.4	65.4	125.6	0.55	10.3	9.6	9.5	0.51	5.9	0	1
NGC 1566	17.7	29.5	216.8	0.64	10.7	9.7	9.8	0.32	4.0	1	1
NGC 2090	11.8	64.5	134.6	−0.5	10.0	8.7	9.4	−0.34	4.5	1	0
NGC 2283	13.7	43.7	82.8	−0.35	9.8	8.6	9.5	−0.04	5.9	1	1
NGC 2835	12.4	41.3	192.4	0.06	9.9	8.8	9.3	0.26	5.0	0	1
NGC 2997	14.1	33.0	307.7	0.64	10.7	9.8	9.7	0.34	5.1	1	0
NGC 3351	10.0	45.1	216.8	0.04	10.3	9.1	8.9	−0.01	3.1	0	1
NGC 3511	13.9	75.1	181.2	−0.08	10.0	9.0	9.1	0.09	5.1	0	1
NGC 3596	11.0	25.1	109.2	−0.56	9.6	8.7	8.8	−0.12	5.2	1	0
NGC 3626	20.0	46.6	88.3	−0.63	10.4	8.6	8.9	−0.76	−0.8	0	1
NGC 3627	11.3	57.3	308.4	0.57	10.8	9.8	9.0	0.21	3.1	1	1
NGC 4207	15.8	64.5	45.1	−0.71	9.7	8.7	8.6	−0.32	7.7	0	0
NGC 4254	13.0	34.4	151.1	0.47	10.4	9.9	9.7	0.4	5.2	1	0
NGC 4293	15.8	65.0	187.1	−0.24	10.4	9.0	7.7	−0.37	0.3	0	0
NGC 4298	13.0	59.2	76.1	−0.48	9.9	9.2	9.0	−0.23	5.1	0	0
NGC 4321	15.2	38.5	182.9	0.53	10.7	9.9	9.4	0.23	4.0	1	1
NGC 4424	16.2	58.2	91.2	−0.53	9.9	8.4	8.3	−0.28	1.3	0	0
NGC 4457	15.0	17.4	83.8	−0.5	10.4	9.0	8.4	−0.58	0.3	1	0
NGC 4496A	14.9	53.8	101.2	−0.21	9.5	8.6	9.2	0.31	7.4	0	1
NGC 4535	15.8	44.7	244.4	0.31	10.5	9.6	9.6	0.14	5.0	0	1
NGC 4540	15.8	28.7	65.8	−0.77	9.8	8.6	8.5	−0.46	6.2	0	1
NGC 4548	16.2	38.3	166.4	−0.27	10.7	9.2	8.8	−0.55	3.1	1	1
NGC 4569	15.8	70.0	273.6	0.13	10.8	9.7	8.9	−0.23	2.4	1	1
NGC 4571	14.0	32.7	106.9	−0.57	10.0	8.9	8.7	−0.4	6.4	0	0
NGC 4689	15.0	38.7	114.6	−0.39	10.1	9.1	8.6	−0.31	4.7	0	0
NGC 4694	15.8	60.7	59.9	−0.89	9.9	8.3	8.6	−0.63	−1.8	0	0
NGC 4731	13.3	64.0	189.7	−0.31	9.4	8.6	9.4	0.24	5.9	1	1
NGC 4781	11.3	59.0	111.2	−0.34	9.6	8.8	9.2	0.08	7.0	0	1
NGC 4941	15.0	53.4	100.7	−0.38	10.2	8.7	8.4	−0.32	2.1	0	1
NGC 4951	15.0	70.2	94.2	−0.49	9.8	8.6	9.0	−0.18	6.0	0	0
NGC 5042	16.8	49.4	125.6	−0.23	9.9	8.8	9.0	−0.01	5.0	0	1
NGC 5068	5.2	35.7	224.5	−0.55	9.3	8.4	8.8	0.07	6.0	0	1
NGC 5134	19.9	22.7	81.3	−0.37	10.4	8.8	8.9	−0.47	2.9	0	1
NGC 5530	12.3	61.9	144.9	−0.48	10.0	8.9	9.1	−0.31	4.2	0	0
NGC 5643	12.7	29.9	157.4	0.39	10.2	9.4	9.1	0.4	5.0	0	1
NGC 6300	11.6	49.6	160.0	0.27	10.4	9.3	9.2	0.18	3.1	0	1
NGC 7456	15.7	67.3	123.3	−0.59	9.6	9.3	8.7	−0.16	6.0	0	0

Note. (a) Distance (Anand et al. 2021). (b) Inclination (Lang et al. 2020). (c) Optical radius from the Lyon–Meudon Extragalactic Database (LEDA). (d) and (e) SFR and M_* (Leroy et al. 2021c). (f) Aperture-corrected total molecular gas mass based on the PHANGS-ALMA observations (Leroy et al. 2021a). (g) Atomic gas mass from LEDA. (h) Offset from the star-forming main sequence ΔMS (Catinella et al. 2018; Leroy et al. 2021c). (i) Hubble type from LEDA. (j) and (k) Presence (=1) and absence (=0) of grand-design spiral arms and stellar bar (Querejeta et al. 2021).

The left panel of Figure 1 shows the SFR–M_* relation for our sample overlaid on a sample of local galaxies from the xCOLD GASS survey (gray circles; Saintonge et al. 2017). The integrated SFR and M_* are derived based on GALEX and WISE (Leroy et al. 2019, 2021c). The line in the figure represents the local star-forming main sequence derived by Leroy et al. (2019). There are roughly equal numbers of galaxies above and below the main sequence. The offset from the main sequence (ΔMS) spans ±0.8 dex (∼a factor of 6). Galaxies already included in the sample of Paper I are highlighted by a green circle (NGC 0628, NGC 3351, NGC 3627, NGC 4254, NGC 4321, NGC 4535, and NGC 5068).

We further classify our galaxies based on the presence of a bar and grand-design (GD) spiral arms. In Figure 1, blue and

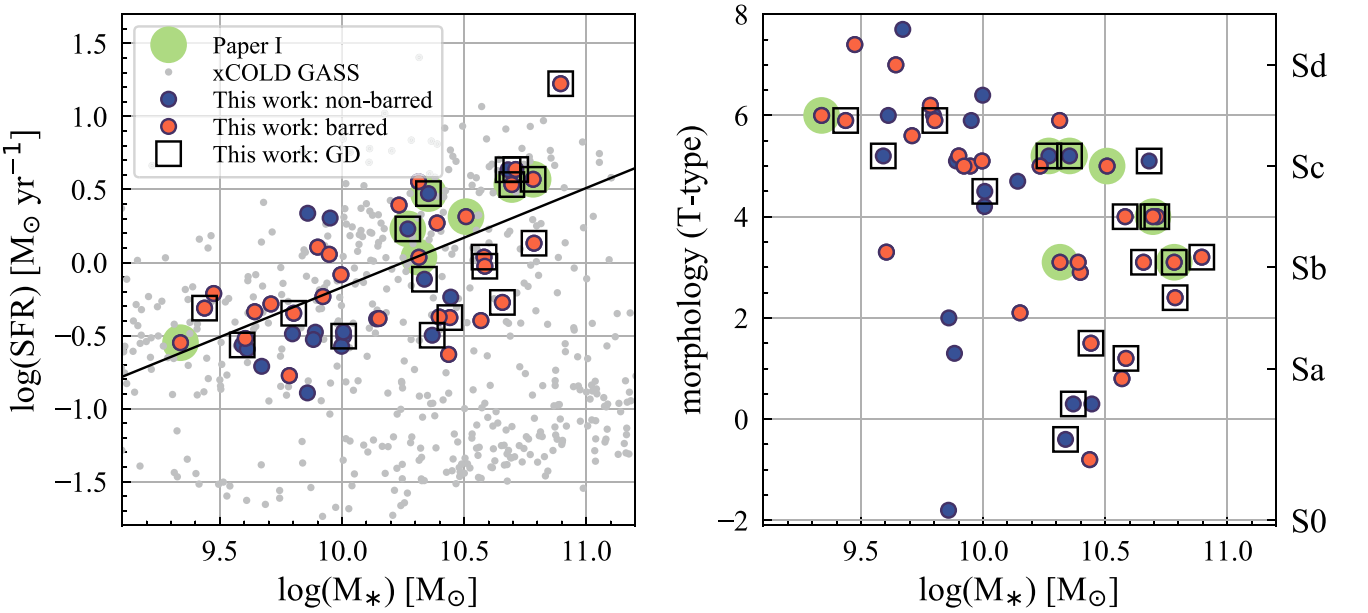

Figure 1. Left: Integrated star formation rate (SFR) vs. stellar mass (M_*). Gray dots represent local galaxies in the xCOLD GASS survey (Saintonge et al. 2017). Large colored circles represent the PHANGS galaxies used in this work. Galaxies with a bar are shown in red, while galaxies without a bar are shown in blue. Further, galaxies with grand-design (GD) spiral arms are marked by open squares. The integrated SFR and M_* of PHANGS galaxies are derived from GALEX and WISE (Leroy et al. 2019, 2021c). The black line represents the local star-forming main sequence (Catinella et al. 2018; Leroy et al. 2019, 2021c). Right: Hubble type vs. M_*. The symbols are the same as in the left panel. Note that the Hubble T type considers the ellipticity and strength of spiral arms and does not reflect the presence or absence of the bar. Galaxies already included in the sample of Paper I are highlighted by a green circle.

red circles denote nonbarred and barred galaxies, respectively, while the galaxies with GD spiral arms are marked by open squares. Information on the galactic structures is provided in Table 1. We define a galaxy as barred if a bar component was implemented in the PHANGS environmental masks (Querejeta et al. 2021) (`morph_bar_flag` in the PHANGS sample table version 1.5). These bar identifications mostly follow Herrera-Endoqui et al. (2015) and Menéndez-Delmestre et al. (2007), with some modifications based on the multiwavelength and kinematic information available in PHANGS. For spiral arms, we adopt the flags `morph_spiral_arms` (i.e., GD spiral arms) from the PHANGS sample table, which comes from visual inspection of multiwavelength data by four PHANGS collaboration members. Strictly speaking, the `morph_spiral_arms` flag in the sample table indicates whether the environmental masks include spiral masks or not. It is generally true that we implemented spiral arms mostly for GD spirals (and did not attempt to do so for flocculent arms). However, in some cases, e.g., due to inclination, we found that the spiral mask was not reliable even though the galaxy shows clear spiral arms and was classified as GD by Buta et al. (2015). Therefore, our classification does not always agree with arm classifications from the literature (e.g., Buta et al. 2015 for S4G[29]).

Morphology classification is presented by the Hubble morphological T type in this work. The T-type values for S0 and Sa–Sd galaxies are approximately −2, 1, 3, 5, and 7, respectively. Note that T type considers the ellipticity and strength of spiral arms but does not reflect the presence or absence of the bar. The right panel of Figure 1 displays the Hubble type of our target galaxies as a function of M_*. The Hubble type of the galaxies in our sample ranges from −1.8 to 7.7 (approximately equivalent to S0–Sd). Our sample shows the expected trend: earlier types (i.e., galaxies with smaller Hubble type values in our sample) are generally more massive (e.g., Kelvin et al. 2014; González Delgado et al. 2015; Laine et al. 2016), but the correlation is rather poor at the high-mass end of our sample of $\log(M_*/M_\odot) > 10$. In this work, we use the term "earlier" to denote galaxies with lower values of Hubble type, but note that our working sample does not contain elliptical galaxies; the earliest-type galaxy in our sample is NGC 4694, with a Hubble type of −1.8 (∼S0).

[29] S4G: Spitzer Survey of Stellar Structure in Galaxies.

3. Methodology

This section introduces the method used to quantify the relative distribution of molecular gas traced by CO emission and recent star formation traced by Hα emission. The method is identical to that used in Paper I, with some changes in tuning parameter values.

3.1. Hα: Filtering Out Emission from Diffuse Ionized Gas

Our analysis uses Hα as a tracer for the location of recent high-mass star formation. However, Hα not only arises from H II regions surrounding the massive stars that ionize them, but also from the larger scale diffuse ionized gas (DIG). To correctly correlate the sites of star formation with molecular gas, our analysis must remove this diffuse component. DIG is the warm ($\sim 10^4$ K) and low-density (<0.1 cm^{-3}) gas found in the ISM of galaxies, which seems similar to the warm ionized medium observed in the Milky Way (see the review by Haffner et al. 2009). The energy sources of DIG are still not well understood. Spectral features, such as the emission-line ratios and ionizing spectrum, of DIG are different from those of H II regions powered by massive young stars (e.g., Hoopes & Walterbos 2003; Blanc et al. 2009; Tomičić et al. 2017, 2019; Zhang et al. 2017), indicating the presence of additional sources of ionization. Because DIG constitutes a substantial

fraction of the Hα flux in star-forming galaxies (e.g., Oey et al. 2007; Tomičić et al. 2021), one must remove the DIG contribution from the Hα fluxes when using Hα as a star formation tracer.

Following the approach utilized in Paper I, a two-step unsharp masking technique is used to remove the DIG from the Hα images. We first identify diffuse emission on scales larger than H II regions and then we take into account higher levels of DIG contribution and clustering of H II regions that are often found in galactic structures (e.g., spiral arms, Kreckel et al. 2016). More specifically, the following steps are undertaken to remove DIG in the original Hα images.

1. *Unsharp mask with a kernel of 200 pc*. We smooth our original image with a Gaussian kernel with an FWHM size of 200 pc, slightly larger than the largest H II regions (Oey et al. 2003; Azimlu et al. 2011; Whitmore et al. 2011). Then we subtract this smoothed image from the original image. We identify initial H II regions as the parts of the map still detected at a high signal-to-noise ratio (S/N) in this filtered map. Specifically, first of all, peaks above 5σ are identified, and then the mask is expanded to contain all connected regions that are above 3σ. H II regions are identified as pixels enclosed within the masks.
2. *Subtract a scaled version of the initial H II regions from the DIG map*. We subtract a scaled version of the H II regions identified in the previous step from the original map. The scaling factor is an arbitrary choice, but we do not want to oversubtract at this stage. A scaling factor of 0.1 is adopted in this work.
3. *Unsharp mask with a kernel of 400 pc*. We smooth our H II region-subtracted image with a Gaussian kernel that has an FWHM of 400 pc, larger than that in Step 1. This scale is set as such to detect higher levels of DIG contribution and clustering of H II regions. Then, we subtract this smooth version of the image from the original image. We identify our final set of H II regions in this filtered map using the same S/N criteria in Step 1.

On average, the DIG removal process removes ∼65% of the Hα emission across the sample, consistent with the DIG fractions of PHANGS galaxies measured by different approaches (Chevance et al. 2020; Belfiore et al. 2021). Moreover, our mean DIG fraction is in good agreement with the mean DIG fraction (∼60%) derived from the Hα-surface-brightness-based method for the 109 nearby star-forming galaxies in Oey et al. (2007). A similar mean DIG fraction is also suggested for The Calar Alto Legacy Integral Field Area Survey (Sánchez et al. 2012) galaxies based on integral-field-spectroscopy (IFS)-based H II/DIG separator (Lacerda et al. 2018). The DIG fractions of our sample galaxies are provided in Table 2. We note that the tuning parameters adopted in this work are different from what was used in Paper I. The choice of parameters in this work is optimized to reproduce H II regions identified with our PHANGS-MUSE IFS Hα-line images, which have a similar spatial resolution (Santoro et al. 2021). Changing the adopted kernel sizes only has a minor impact on the number of H II regions but does affect their sizes. Therefore, a key assessment of the performance of the DIG removal strategy is to avoid H II region overgrowth. This can be evaluated using emission-line ratios accessible via spectroscopic observations: for example, the [N II]/Hα and [S II]/Hα ratios are higher in the DIG relative to H II regions (e.g., Hoopes et al. 1999; Blanc et al. 2009; Kreckel et al. 2016; Tomičić et al. 2017, 2021). The full catalog of H II regions identified in our narrowband Hα maps, including a detailed description of how we verified the narrowband H II regions using PHANGS-MUSE spectroscopic information and the dependence of DIG fraction on galaxy properties will be presented in a forthcoming paper (H.-A. Pan et al. 2022, in preparation). Our results remain qualitatively unchanged when using the tuning parameters in Paper I, as discussed in Appendix A.3. In this work, we assume all the Hα emission surviving from the DIG removal process is from H II regions, and the contribution from other powering sources, such as active galactic nuclei (AGNs), post-asymptotic-giant-branch stars, and shocks, are statistically minor in the analysis. Separating these sources from H II regions relies on emission-line diagnostics and therefore spectroscopic observations.

Table 2
Fraction (%) of Diffuse Ionized Gas inside $<0.6\,R_{25}$ for Each Galaxy in Our Sample

Galaxy	DIG (%)	Galaxy	DIG (%)	Galaxy	DIG (%)
IC 1954	70	NGC 2997	46	NGC 4569	62
IC 5273	73	NGC 3351	62	NGC 4571	68
NGC 0628	51	NGC 3511	65	NGC 4689	77
NGC 1087	49	NGC 3596	52	NGC 4694	91
NGC 1300	66	NGC 3626	86	NGC 4731	65
NGC 1317	80	NGC 3627	64	NGC 4781	74
NGC 1365	60	NGC 4207	74	NGC 4941	84
NGC 1385	49	NGC 4254	50	NGC 4951	80
NGC 1433	69	NGC 4293	88	NGC 5042	92
NGC 1511	64	NGC 4298	58	NGC 5068	52
NGC 1512	65	NGC 4321	58	NGC 5134	88
NGC 1546	79	NGC 4424	87	NGC 5530	66
NGC 1559	62	NGC 4457	81	NGC 5643	71
NGC 1566	48	NGC 4496A	55	NGC 6300	58
NGC 2090	74	NGC 4535	78	NGC 7456	87
NGC 2283	57	NGC 4540	69		
NGC 2835	41	NGC 4548	87		

Note. On average, the DIG removal process (Section 3.1) removes ∼65% of the Hα emission across the sample.

Here we note two important caveats of our DIG removal process. We use an S/N threshold when identifying H II regions during the unsharp masking step. Because the noise and native resolution of the input Hα images vary, the effective Hα surface-brightness threshold applied to our fiducial maps therefore also varies, corresponding to SFR surface densities of $\sim 10^{-3}$–10^{-2} $M_{\odot}$ yr^{-1} kpc^{-2} depending on the galaxy target.[30] For a point source at the native resolution of our Hα data, the effective sensitivity limits in terms of Hα surface-brightness threshold applied to the fiducial maps corresponds to H II region luminosities ($\log(L_{\rm H\,II\,region}^{\rm sensitivity}/{\rm erg\ s^{-1}})$) between 36.7 and 38.4, with most (∼80%) being between 37 and 38. The $L_{\rm H\,II\,region}^{\rm sensitivity}$ for our galaxies are listed in Table 3. The H II region sensitivity limits are comparable to the turnover point of the H II region luminosity function measured by narrowband Hα imaging in the literature (e.g., Bradley et al. 2006; Oey et al. 2007), but we may miss the low-luminosity H II regions detected by optical integral field units (Kreckel et al. 2016; Rousseau-Nepton et al. 2018; Santoro et al. 2021), which are unavailable at the

[30] We adopt Equation (6) in Calzetti et al. (2007) for the relation between SFR and Hα emission, which assumes a Kroupa initial mass function.

Table 3
Parameters of Hα and CO Observations

Galaxy	Hα res. (pc)	CO res. (pc)	$L_{\rm H\,II\ region}^{\rm sensitivity}$ (log(erg s^{-1}))	$1\sigma\ \Sigma_{\rm H_2}$ ($M_\odot$ pc^{-2})	Galaxy	Hα res. (pc)	CO res. (pc)	$L_{\rm H\,II\ region}^{\rm sensitivity}$ (log(erg s^{-1}))	$1\sigma\ \Sigma_{\rm H_2}$ ($M_\odot$ pc^{-2})
IC 1954	88	91	37.6	0.9	NGC 4293	53	88	36.7	1.5
IC 5273	77	120	37.4	0.8	NGC 4298	71	105	37.3	1.0
NGC 0628	41	53	37.0	1.5	NGC 4321	47	121	37.0	2.1
NGC 1087	69	123	36.9	1.8	NGC 4424	81	89	37.7	1.7
NGC 1300	73	95	36.8	3.1	NGC 4457	91	80	37.8	2.2
NGC 1317	74	147	37.3	1.6	NGC 4496A	73	90	37.2	1.3
NGC 1365	58	130	36.9	2.4	NGC 4535	87	119	37.6	1.6
NGC 1385	85	105	36.9	2.6	NGC 4540	77	104	37.3	2.8
NGC 1433	74	62	37.1	1.6	NGC 4548	73	132	37.1	1.0
NGC 1511	84	107	37.8	0.9	NGC 4569	89	128	37.3	0.7
NGC 1512	67	90	36.8	1.4	NGC 4571	85	79	37.3	1.8
NGC 1546	125	114	37.6	0.7	NGC 4689	97	85	37.4	1.9
NGC 1559	129	117	37.7	1.5	NGC 4694	73	88	37.9	1.3
NGC 1566	62	104	36.9	2.0	NGC 4731	61	98	37.2	0.5
NGC 2090	52	73	36.9	1.0	NGC 4781	52	72	37.5	0.9
NGC 2283	54	87	37.5	1.5	NGC 4941	94	115	37.4	0.7
NGC 2835	56	50	37.2	1.7	NGC 4951	83	91	37.6	0.8
NGC 2997	64	92	36.8	1.3	NGC 5042	84	107	37.7	1.0
NGC 3351	56	70	37.4	1.4	NGC 5068	32	24	37.4	2.0
NGC 3511	75	121	37.4	0.4	NGC 5134	91	118	37.8	1.7
NGC 3596	63	65	37.4	3.0	NGC 5530	65	66	37.5	1.2
NGC 3626	148	114	38.4	2.5	NGC 5643	73	75	37.6	1.6
NGC 3627	80	86	37.3	1.3	NGC 6300	60	60	37.2	1.7
NGC 4207	70	93	37.6	2.0	NGC 7456	84	127	37.4	0.4
NGC 4254	59	107	37.2	3.1					

Note. Hα res. and CO res. denote the native physical resolution of Hα and CO observations. $L_{\rm H\,II\ region}^{\rm sensitivity}$ is the effective sensitivity limits in terms of the H II region luminosity at the native resolution (Section 3.1). The sensitivity of the CO observation is represented by $1\sigma\ \Sigma_{\rm H_2}$ at 150 pc resolution (Section 3.2).

necessary resolution for the bulk of the galaxies in our sample. Therefore, we may underestimate the number of sight lines with Hα emission (see Appendix A.4 for a detailed discussion on the impact of Hα sensitivity). Moreover, our Hα-line images are not corrected for dust attenuation, thus the maps may miss the most heavily embedded regions. Because our main analysis focuses mostly on the location (rather than the amount) of massive star formation, we consider internal extinction as a secondary issue. However, for some analysis based on flux, we may underestimate Hα flux for the regions where CO (and therefore dust) is present.

3.2. CO: Applying a Physical Threshold

The CO images are treated using a similar scheme. We clip the CO images at our best-matching resolution of 150 pc using a $\Sigma_{\rm H_2}$ threshold of $10\,M_\odot$ pc^{-2} accounting for galaxy inclination. This corresponds to a $3\sigma\ \Sigma_{\rm H_2}$ sensitivity of our CO map with the lowest sensitivity at this spatial scale (Table 3). The applied threshold value is lower than the threshold used in Paper I (i.e., 12.6 $M_\odot$ pc^{-2}) due to the lower sensitivity of the PAWS M51 observations. To have a data sample with homogeneous observational properties, M51 is not included in this work. Our results remain qualitatively unchanged if different $\Sigma_{\rm H_2}$ clipping values are adopted (see Appendix A.5).

3.3. Measuring Sight-line Fractions

First of all, the thresholded Hα maps are regridded to match the pixel grid of the CO maps because the FoV of our ALMA observations is considerably smaller than that of narrowband observations. We convolve each thresholded CO and Hα image by a Gaussian to a succession of resolutions, ranging from our highest common resolution of 150 to 1500 pc, in steps of 100 pc. Then, we clip the low-intensity emission in the convolved images. For each convolved image, we blank the faintest sight lines that collectively contribute 2% of the total flux in the image to suppress convolution artifacts. The results remain robust to small variations (1%–4%) of this threshold.

Finally, we measure the presence or absence of the two tracers at each resolution in an FoV extending to $0.6\,R_{25}$, which is the largest radial extent probed by our data in all galaxies, corresponding to ∼6.4 kpc on average (5–22 kpc, mostly <15 kpc). We divide each sight line (pixel) within $0.6\,R_{25}$ in the thresholded and artifact-clipped CO and Hα images into one of four categories:

1. *CO-only*: only CO emission is present
2. *Hα-only*: only Hα emission is present
3. *Overlap*: both CO and Hα emission are present
4. *empty*: neither CO nor Hα emission is present.[31]

The fraction of sight lines with (i.e., *CO-only*+*Hα-only*+*Overlap*) and without (i.e., *empty*) any emission are given in Table 4. At the highest common resolution of 150 pc, the median fraction of sight lines without any emission within $0.6\,R_{25}$ of our galaxies is as high as 70%, ranging from 13% to 97%. Moreover, the fractions of *empty* sight lines decrease with increasing spatial scales (Figure B1; see also Pessa et al. 2021).

[31] We note that the *empty* pixels in the filtered maps may contain DIG and/or CO emission with a surface density below the applied threshold in the original maps.

Table 4
Fraction of Sight Lines with (and without) Any CO or Hα Emission inside <0.6 R_{25} for Our Sample Galaxies, Measured at 150 pc Resolution

IC 1954	48(52)	NGC 1512	8(92)	NGC 3596	46(54)	NGC 4496A	24(76)	NGC 4941	20(80)
IC 5273	33(67)	NGC 1546	30(70)	NGC 3626	7(93)	NGC 4535	19(81)	NGC 4951	30(70)
NGC 0628	27(73)	NGC 1559	50(50)	NGC 3627	31(69)	NGC 4540	40(60)	NGC 5042	9(91)
NGC 1087	58(42)	NGC 1566	22(78)	NGC 4207	40(60)	NGC 4548	11(89)	NGC 5068	31(69)
NGC 1300	14(86)	NGC 2090	40(60)	NGC 4254	71(29)	NGC 4569	15(85)	NGC 5134	21(79)
NGC 1317	12(88)	NGC 2283	46(54)	NGC 4293	3(97)	NGC 4571	32(68)	NGC 5530	42(58)
NGC 1365	13(87)	NGC 2835	29(71)	NGC 4298	87(13)	NGC 4689	45(55)	NGC 5643	49(51)
NGC 1385	39(61)	NGC 2997	36(64)	NGC 4321	41(59)	NGC 4694	10(90)	NGC 6300	48(52)
NGC 1433	16(84)	NGC 3351	22(78)	NGC 4424	11(89)	NGC 4731	10(90)	NGC 7456	14(86)
NGC 1511	37(63)	NGC 3511	39(61)	NGC 4457	26(74)	NGC 4781	53(47)		

The distributions of empty pixels among galaxies is a potentially interesting diagnostic of ISM evolution and host-galaxy properties. We defer a detailed analysis of the statistics relating to empty pixels to a future investigation because the main focus of this paper is the impact of host-galaxy properties and observing scale on the relative distribution of molecular and ionized gas.

We measure the fraction of sight lines and the fraction of flux in each region type, i.e., *CO-only*, *Hα-only*, and *Overlap*, at each resolution. All galaxies in our sample have nonzero fractions for the three region types at the highest common resolution of 150 pc (Appendix B). Because we do not consider the sight lines where neither CO nor Hα emission is present, the sum of *CO-only*, *Hα-only*, and *Overlap* sight lines is 100%. We also define *CO sight lines* as regions that are classified as either *CO-only* or *Overlap* (i.e., sight lines with CO emission, regardless of whether they are associated with Hα emission or not), while *Hα sight lines* are defined as regions of *Hα-only* or *Overlap* (i.e., sight lines with Hα emission, regardless of whether they are associated with CO emission).

4. Results

4.1. CO and Hα Fractions at 150 pc Resolution

There are significant galaxy-to-galaxy variations in the CO and Hα distributions. Figure 2 presents some examples of the distribution of different sight-line categories at 150 pc resolution (maps for the full sample are provided in Appendix B). The blue, red, and yellow regions denote *CO-only*, *Hα-only*, and *Overlap* sight lines, respectively. We define the galactic center as the region within 1 kpc (i.e., 2 kpc in diameter) of the galaxy nucleus. The region that we define as the center is indicated in each panel as a magenta ellipse in Figure 2, while the region that we use to measure the global sight fraction is indicated by a white ellipse (i.e., 0.6 R_{25}).

The histograms of Figure 3, from left to right, show the distribution of *CO-only*, *Hα-only*, and *Overlap* fractions within the fiducial FoV at 150 pc scale, respectively. The box plots shown at the top of each panel summarize the statistics for the sight-line fractions. The sight-line fractions for each individual galaxy are provided in Table B1 of Appendix B). The median and mean sight-line fractions are given in the upper-right corner of the panels. In the rest of the paper, we will use the median as the measure of the central tendency because the mean is more sensitive to extreme values. The mean values are given in the relevant figures and tables for reference.

We find a wide range of *CO-only* fractions in our sample from 3% to 78%, with a median of 36%. While the *Hα-only* fraction peaks at the lower end (<20%), *Hα-only* sight lines show a wider range of spatial coverage than the *CO-only* sight lines, from nearly 0 to almost 95%. The median *Hα-only* fraction is 20%. The *Overlap* region exhibits a narrower range than the *CO-only* or *Hα-only* regions and shows a preference for intermediate values from 20% to 50%, with a median of 30%.

In terms of the relative frequency of the three types of sight lines, our results are qualitatively consistent with the conclusions of Paper I based on a smaller sample of only eight galaxies. However, Paper I reports considerably higher median values for *CO-only* and *Overlap* sight lines (42% for *CO-only* and 37% for *Overlap*) and a slightly higher median for *Hα-only* (23%). We ascribe this difference to the combined effect of different thresholds for CO and Hα images and sample composition (e.g., M_* distribution; see Figure 1 and the next subsection).

4.1.1. Trends with Host-galaxy Properties

To explore the potential origin of the galaxy-to-galaxy variation in the spatial distributions of CO and Hα, we first compute the Spearman rank correlation coefficients between the sight-line fractions and various host-galaxy and observational properties. The correlation coefficients are given in Table 5. In this work, a significant correlation is defined as a correlation coefficient of absolute value greater than 0.3.

The strongest correlations are found with M_* and Hubble type for *CO-only* and *Hα-only* fractions. The fractions of *CO-only* and *Hα-only* regions are moderately correlated with M_*, with correlation coefficients of 0.53 and −0.44, respectively. The *CO-only* and *Hα-only* fractions also correlate with Hubble type, with correlation coefficients of −0.59 and 0.38, respectively. In contrast to the *CO-only* and *Hα-only* regions, *Overlap* fractions show no significant correlation with M_* and Hubble type in terms of correlation coefficients, −0.01 and 0.24, respectively.

To further visualize the dependence of the sight-line fractions on M_* and Hubble type, Figure 4 shows box plots of sight-line fractions as a function of M_* (left) and Hubble type (right). Galaxies are divided into three groups according to their M_* or Hubble type. The darker colors indicate increasing M_* or decreasing Hubble-type value. The median and mean sight-line fractions for a given M_* or Hubble type are given in Table 6.

The left panel of Figure 4 shows a tendency for more massive galaxies to have higher *CO-only* fractions. The median *CO-only* fractions increase from 14% to 33% and to 50% from our lowest- to highest-M_* bin. This dependency partially explains the higher median *CO-only* fractions in Paper I because that sample is largely dominated by galaxies with $\log(M_*/M_\odot) > 10.2$. The opposite trend is exhibited by

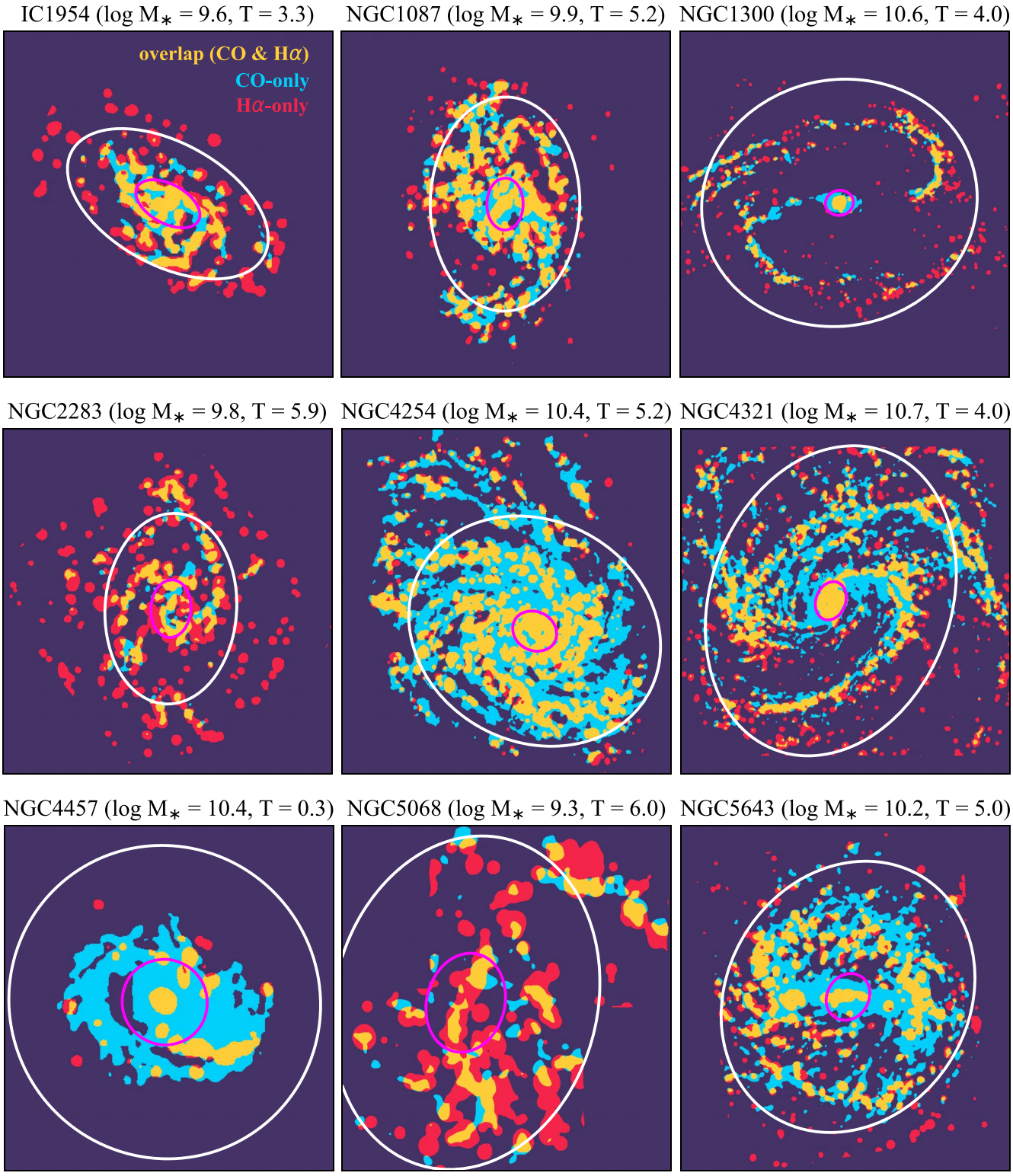

Figure 2. Examples of the spatial distribution of different sight lines. Galaxy maps show the regions of *CO-only* (blue), *Hα-only* (red), and *Overlap* (yellow) sight lines at 150 pc resolution. The inner ellipses (magenta) mark the central region, defined as the central 2 kpc in deprojected diameter. The outer ellipses (white) indicate the $0.6R_{25}$ regions where we measure the global sight-line fractions. The M_* (in units of solar mass in log scale) and Hubble type of each galaxy are given at the top of each panel.

Hα-only fractions, with the median fraction decreasing gradually from 61% to 21% and to 13%. Moreover, the two lower-M_* bins reveal a scatter in *Hα-only* fractions larger than that for the highest-M_* bin, while the opposite trend is observed for *CO-only* sight lines. We note that the median *Hα-only* fraction in our highest-M_* bin is lower than the median *Hα-only* fraction of galaxies with similar mass in Paper I because the H II regions in this work are generally smaller than those in Paper I. This is driven by the different kernel sizes used in the unsharp masking technique to remove

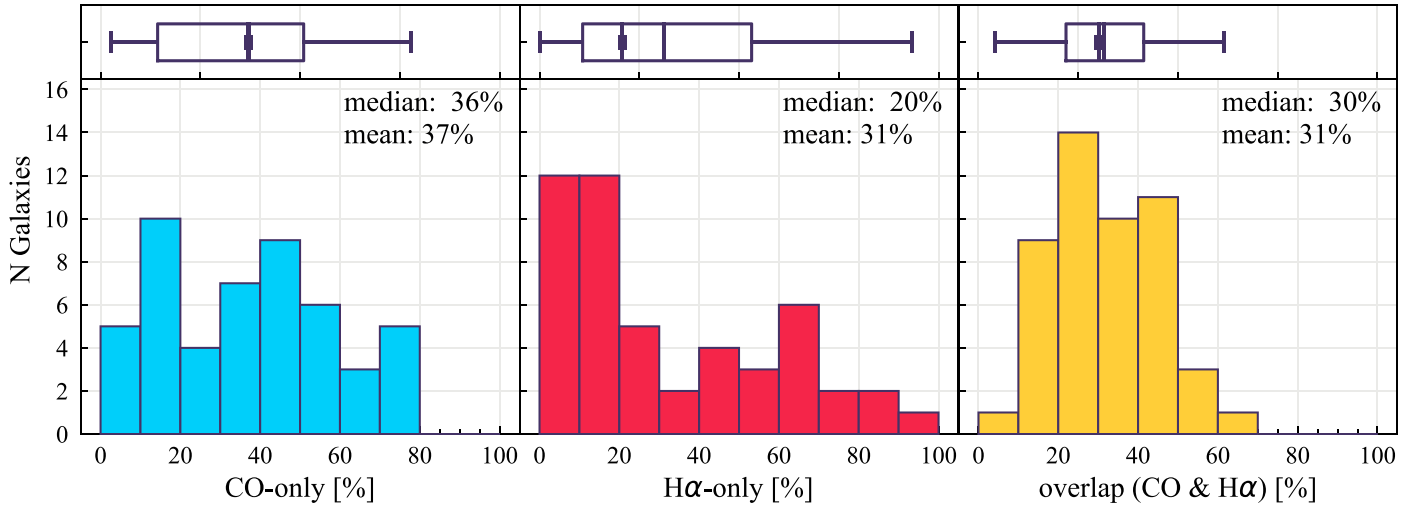

Figure 3. Distribution of global *CO-only* (left), *Hα-only* (middle), and *Overlap* (right) sight-line fractions at a resolution of 150 pc. Corresponding box plots are shown at the top of each panel. The boxes show the interquartile ranges (IQR; the Q1/25 percentile to Q3/75 percentile), and the horizontal whiskers extend to Q1 − 1.5 × IQR and Q3 + 1.5 × IQR. The inner vertical belt-like symbol and line in the boxes represent the median and mean of the distribution, respectively; the values are also given in the upper right of each panel. Substantial galaxy-to-galaxy variations are seen for all sight-line categories.

Table 5
Spearman Correlation Coefficients between Sight-line Fractions at 150 pc Resolution and Global Properties

	CO-only	*Hα-only*	*Overlap*
Galaxy properties			
M_*	**0.53**	**−0.44**	−0.01
Hubble type	**−0.59**	**0.38**	0.24
Distance	**0.39**	−0.28	−0.09
R_{25}	0.08	0.02	−0.17
Inclination	−0.09	0.15	−0.16
DIG fraction	**0.31**	−0.08	**−0.37**
Observations			
Effective Hα sensitivity	**0.30**	−0.18	−0.14
Hα native resolution	**0.38**	−0.25	−0.13
Effective CO sensitivity	0.25	**−0.39**	**0.36**
CO native resolution	0.29	−0.25	0.02
Star formation			
sSFR	**−0.32**	0.17	0.20
ΔMS	−0.15	0.02	0.21

Note. The significant correlations, which we define as |coefficient| ⩾ 0.3, are highlighted in boldface. Scatter plots for each pair of variables are presented in Appendix C.

emission associated with the DIG. The median *Overlap* fractions remain at a nearly constant value as a function of M_* (27% to 35% and to 30%), but the scatter in the *Overlap* fraction decreases with increasing M_*.

The trends with Hubble type and M_* are consistent in the sense that late-type galaxies tend to be less massive (right panel of Figure 4). The three Hubble-type bins in the right panel of Figure 4 roughly correspond to earlier types than Sab ($T \leqslant 2$), around Sb–Sc ($2 < T \leqslant 5$), and later than Sc ($T > 5$). Unlike for M_*, the *Overlap* fraction shows an increasing trend toward later-type galaxies. However, the differences in the *Overlap* fraction between the different galaxy types are still significantly smaller than those for the *CO-only* and *Hα-only* fractions, and the correlation coefficient (0.20) indicates a nonsignificant correlation.

We use partial rank correlation to examine whether the dependence of *CO-only* and *Hα-only* fractions on Hubble type is entirely due to the correlation with M_* or the other way around. The partial rank correlation coefficient $r_{12,3}$ measures the strength of the correlation between x_1 and x_2 when excluding the effect of x_3. The partial rank correlation can be computed based on the Spearman rank correlation coefficient between the three variables as follows:

$$r_{12,3} = \frac{r_{12} - r_{13}r_{23}}{\sqrt{(1 - r_{13}^2)(1 - r_{23}^2)}}, \quad (2)$$

where r_{ij} denotes the correlation between variables i and j. Using the rank correlation coefficients in Table 5 and Equation (2), the partial rank correlations between *CO-only* and *Hα-only* with M_* become 0.35 and −0.32, respectively, when Hubble type is controlled. The correlations between *CO-only* and *Hα-only* with Hubble type are −0.45 and 0.21 while holding M_*. The partial correlation coefficients between these two sight-line fractions with M_* and Hubble type are lower than those of the bivariate coefficients. We therefore conclude that the correlations between the *CO-only* and *Hα-only* fractions and both M_* and Hubble type are physical in nature, but the correlation between M_* and Hubble type may come between them. Such dependencies of the sight-line fractions (*CO-only* and *Hα-only*) on M_* and Hubble type have also been hinted at by the small (eight) sample of galaxies in Paper I.

We also compute the correlation coefficients for the sight-line fractions with other host-galaxy and observational properties: galaxy distance, optical size (R_{25}), disk inclination, native resolution, and effective sensitivity of the Hα ($\log(L_{\rm H\,II\,region}^{\rm sensitivity}$ in Section 3.1) and CO ($1\sigma\,\Sigma_{\rm H_2}$ at 150 pc resolution) observations, specific SFR (sSFR = SFR/M_*), and offset from the star-forming main-sequence (ΔMS) (Table 5). Scatter plots of the sight-line fractions as a function of all the properties we explore in this section are shown in Appendix C. Galaxies with lower M_* are generally more nearby in our sample, caused by a potential sample-selection bias. Therefore, the dependence of sight-line fractions on distance, sensitivity, and resolution might be a result of this selection effect. In principle, sight-line

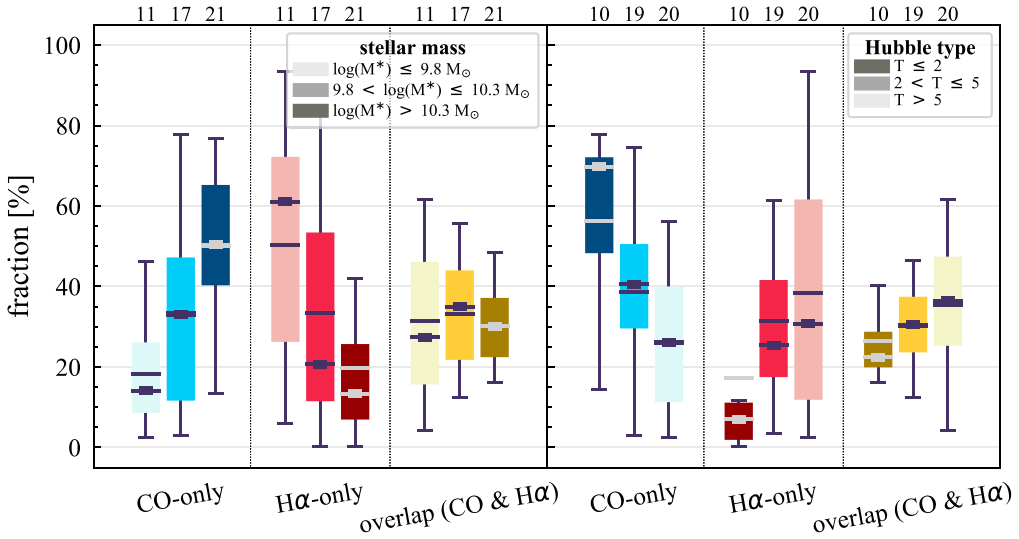

Figure 4. Variations of the global sight-line fractions at 150 pc resolution as a function of M_* (left) and Hubble type (right). For a given type of sight line, the color darkness of the box plots resembles increasing M_* (from left to right) or decreasing Hubble-type value (from right to left). The number of galaxies in each M_* and Hubble-type bin are shown at the top of the plots. Symbols of the box plot are the same as in Figure 3. The *CO-only* and *Hα-only* sight-line fractions are correlated with M_* and Hubble type, while the *Overlap* fractions are less sensitive to galaxy properties.

Table 6
Median (Mean) Sight-line Fractions at the 150 pc Spatial Scale for Different Stellar-mass and Hubble-type Bins

	$\log(M_*/M_\odot) \leqslant 9.8$	$9.8 < \log(M_*/M_\odot) \leqslant 10.3$	$\log(M_*/M_\odot) > 10.3$
CO-only [%]	14 (18)	33 (33)	50 (50)
Hα-only [%]	61 (50)	21 (33)	13 (20)
Overlap [%]	27 (32)	35 (33)	30 (30)
	$T \leqslant 2$	$2 < T \leqslant 5$	$T > 5$
CO-only [%]	70 (56)	41 (39)	26 (26)
Hα-only [%]	7 (17)	25 (31)	31 (38)
Overlap [%]	22 (26)	31 (30)	36 (35)
$\log(M_*/M_\odot)$	10.4 (10.3)	10.4 (10.4)	9.8 (9.9)

Note. The median (mean) stellar mass for each Hubble type bin is provided in the bottom row.

fractions could correlate with the DIG fraction, in the sense that removing a higher fraction of Hα flux would lead to a higher *CO-only* fraction and lower *Hα-only* and *Overlap* sight lines. Such a dependence is seen in terms of correlation coefficients, but only for *CO-only* (0.31) and *Overlap* regions (−0.37). The sight-line fractions show no significant correlation with other galaxy and observational properties we explore.

The *CO-only* fraction shows a correlation with sSFR (−0.32). At the same time, sSFR is correlated with M_*, in the sense that along the star-forming main sequence, galaxies with higher M_* tend to have lower sSFR (Brinchmann et al. 2004; Salim et al. 2007). We checked the partial correlation of the *CO-only* fraction and sSFR, taking M_* as the control variable. The correlation between the *CO-only* fraction and sSFR no longer exists (−0.17) when M_* is controlled for, but the correlation between *CO-only* and M_* still holds while controlling for the effect of sSFR (0.47). This suggests that the correlation with sSFR is an outcome of the dependence on M_*. There is no correlation between the sight-line types and ΔMS, which we discuss further in Section 5.3.

4.1.2. Radial Distribution of CO and Hα Sight Lines

We quantify the radial trends of *CO-only*, *Hα-only*, and *Overlap* fractions (from left to right) in Figure 5. Here, box plots showing the galaxy distributions for each of the sight-line fractions are shown as a function of deprojected galactocentric radius normalized to R_{25} in annuli of width $0.2\,R_{25}$. For each galaxy, we only compute its radial sight-line fractions out to the maximum radius of complete azimuthal [0, 2π] coverage. For each radial bin, the light to dark box plots represent the distributions for the lowest (later) to highest (earlier) bins of M_* (Hubble type). The three boxes at a given radius are offset by $0.05\,R_{25}$ on the plot for clarity. The number of galaxies in each radial bin is indicated above each panel. Some galaxies have a maximum complete radius up to $1.2\,R_{25}$. For reference, we show the sight-line fractions of each individual galaxy at these radii using symbols rather than box plots. Note that the data points at the $R > 0.6\,R_{25}$ regime are dominated by large spiral galaxies. Due to the biased sample and low number statistics, data at $>0.6\,R_{25}$ are not included in our discussion. The color-coding of each symbol is the same as for the box plots at $R < 0.6\,R_{25}$.

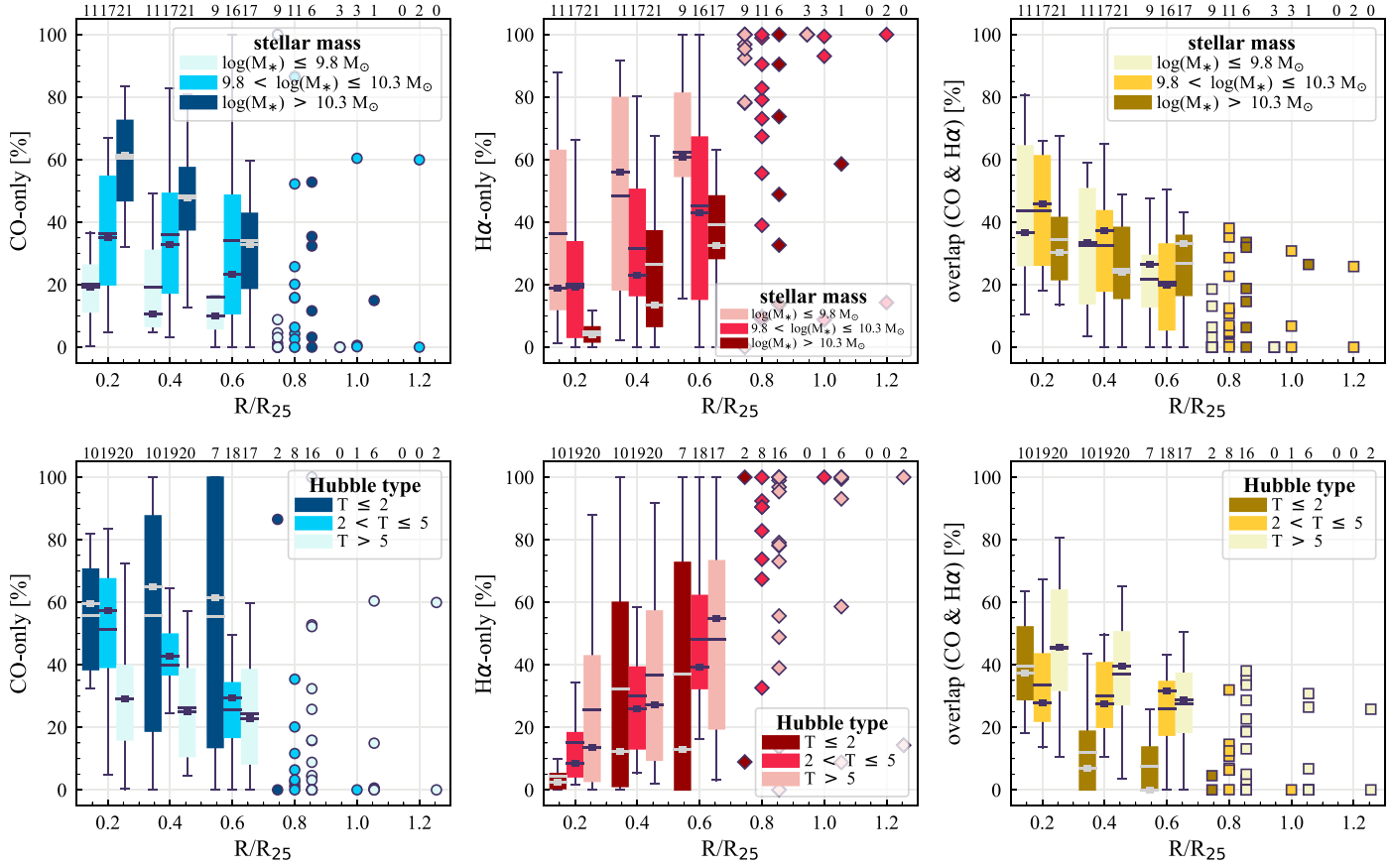

Figure 5. Radial profiles of the *CO-only* (left), *Hα-only* (middle), and *Overlap* (right) sight lines for galaxies with different global properties at 150 pc resolution. Top row: radial profiles of sight-line fractions from 0.2 to 1.2 times R_{25} stacked in bins of stellar mass. Line and color styles are the same as in Figure 4. The number of galaxies in each radial bin is shown at the top of the plots. Because the number of galaxies with a maximum radius of $> 0.6R_{25}$ is low, we show the sight-line fractions of each individual galaxy at these radii with symbols rather than box plots. The color-coding of the symbols is the same as for the box plots at $R < 0.6R_{25}$. Bottom row: radial profiles of sight-line fractions for galaxies in the three Hubble-type bins. All sight-line categories show a strong radial dependence. These trends observed for global sight-line fractions in Figure 4 are almost preserved radially from the center out to 0.6 R_{25} (corresponding to ∼6 kpc on average).

The sight-line fractions show a strong radial dependence. *CO-only* sight lines decrease with increasing radius and the fractions of *Hα-only* sight lines increase with radius. The ordering between sight-line fractions and M_* is observed in each radial bin at $R \lesssim 0.6\,R_{25}$, suggesting that the dependence (or lack of dependence) of the total sight-line fractions on M_* and Hubble type in Figure 4 is driven by the local trends at all radii. The median *CO-only* fractions at $R \lesssim 0.6\,R_{25}$ are at least doubled when moving from the lowest to the highest-M_* bins. The radial profiles of *Hα-only* sight lines also show a clear ranking with M_* at $R \lesssim 0.6\,R_{25}$, increasing from the highest- to the lowest-M_* bins. The differences between M_* bins are considerably smaller for the *Overlap* regions, but it can be seen that the radial profile of the *Overlap* sight lines is shallower for the highest-M_* bin than for the two lower-M_* bins. This is at least partially due to the fact that lower-mass galaxies generally have lower *CO-only* fractions at larger radii than high-mass galaxies; given that the *Overlap* regions appear to be embedded in the *CO-only* regions (Figure 2), the chance of having *Overlap* sight lines at large radii of lower-mass galaxies is small.

The observed correlation between the sight-line fractions and Hubble type in Figure 4 is also seen in most of the radial bins, but the rankings are not as obvious as for M_*, partially due to the lower number statistics for the earliest bin.

4.2. Trends with Galactic Structure

Molecular gas is preferentially formed or collected efficiently in galactic structures such as bars and spiral arms. Because the distribution of molecular gas subsequently determines the potential sites of star formation, it is natural to expect that the distributions of CO and Hα emission are also regulated by galactic structures.

We classify our target galaxies into four groups according to the presence and absence of bar and GD spiral arms:

1. *no structures (NS):* galaxies without a bar and GD spiral arms (e.g., galaxies with flocculent/multiple arms are in this category)
2. *Bar:* galaxies with a bar but no GD spiral arms
3. *Bar+GD:* galaxies with a bar and GD spiral arms
4. *GD:* galaxies with GD spiral arms but without a bar.

The number of galaxies in groups (1) to (4) is 12, 19, 11, and 7, respectively. The statistics of sight-line fractions for each category at 150 pc resolution are provided in Table 7; the corresponding box plots are shown in Figure 6. While the sight-line fractions for NS, Bar, and Bar+GD span a similar range, GD galaxies exhibit a distinct sign of higher *CO-only* and *Overlap* fractions and lower *Hα-only* fractions than the other populations. Because GD galaxies have a lower median M_* ($\log(M_*/M_\odot) = 10.3$) than the Bar+GD galaxies (10.7)

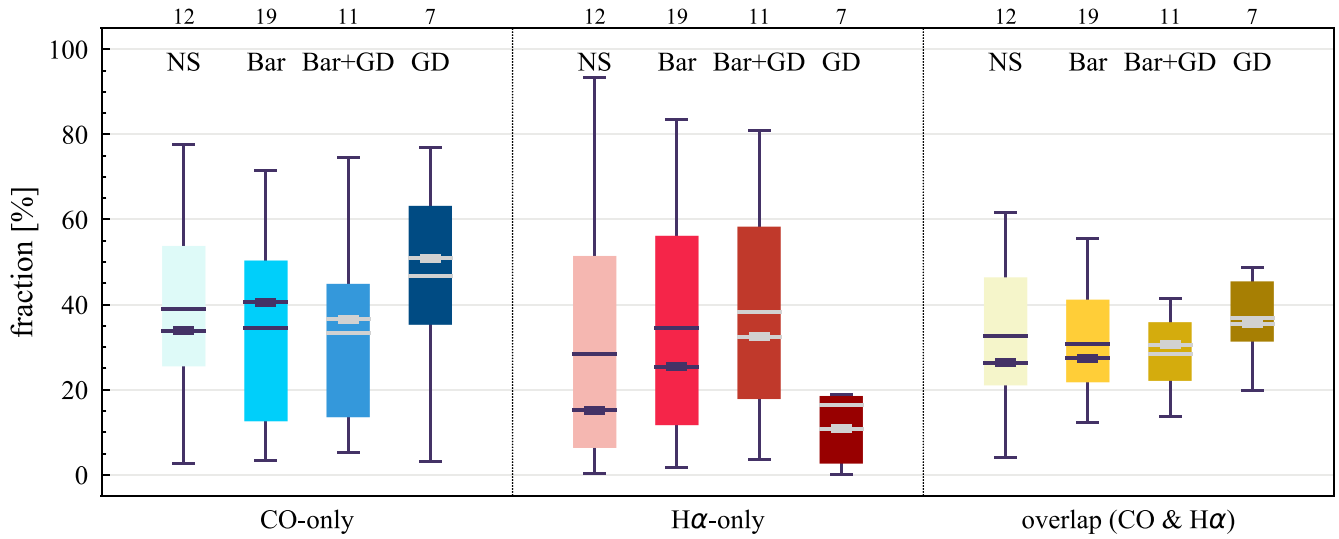

Figure 6. Sight-line fractions at 150 pc resolution for galaxies without structures (bar or grand-design spiral arms; NS), galaxies with a bar but without grand-design spiral arms (Bar), galaxies with both a bar and grand-design spiral arms (Bar+GD), and galaxies with grand-design spiral arms but no bar (GD). GD exhibits a distinct sign of higher *CO-only* and *Overlap* fractions and lower *Hα-only* fractions than the other populations.

Table 7
Median (Mean) Sight-line Fractions and Stellar Masses for Galaxies with Different Structures at 150 pc Resolution

	No Structure (NS)	Bar Only (Bar)	Bar and GD Spiral Arms (Bar+GD)	GD Spiral Arms Only (GD)
CO-only	34 (39)	41 (35)	37 (33)	51 (47)
Hα-only	15 (28)	25 (35)	32 (38)	11 (16)
Overlap	26 (33)	27 (31)	31 (28)	36 (37)
$\log(M_*/M_\odot)$	9.9 (9.9)	10.0 (10.0)	10.7 (10.5)	10.3 (10.2)

Note. The median (mean) stellar mass for galaxies with different structures is given in the bottom row. The number of galaxies in NS, Bar, Bar+GD, and GD is 12, 19, 11, and 7, respectively.

(Table 7), the differences in the *CO-only* and *Hα-only* fractions between GD and Bar+GD are opposite to what one would expect if M_* is the dominant driver of the sight-line fractions and point to the potential importance of galactic structure on regulating the star formation process.

Figure 7 presents the radial sight-line fractions for each structure type at 150 pc resolution. The bar length in our galaxy sample ranges from ∼0.1 to 0.9 R_{25}, with most bar lengths around 0.1−0.5 R_{25}. The median bar length of Bar+GD galaxies (0.3 R_{25}) is slightly longer than that of Bar galaxies (0.2 R_{25}). Galaxies with a bar (Bar and Bar+GD) visually show stronger radial dependence of *CO-only* sight lines than galaxies without a bar (NS and GD), in the sense that their median *CO-only* fraction gradually decreases with increasing radius. The opposite trend is observed for *Overlap* regions. Moreover, Figure 7 suggests that the high total *CO-only* fraction in GD galaxies (Figure 6) is due to the increased fraction at ∼0.4–0.6 R_{25}. On the other hand, the low total *Hα-only* fraction can be attributed to a lack of *Hα-only* regions at <0.4 R_{25}.

In summary, the results in this section show that, in addition to global galaxy properties, galactic dynamics add a further layer of complexity to the distribution of CO and Hα emission. We note that the FoV covering fraction of galactic structures could affect the sight-line fractions. For example, while bars are fully covered by our FoV, we may miss the outer part of some GD spiral arms. This analysis could be taken further by counting the sight lines within individual fully sampled structures, but that is beyond the scope of this paper. We refer the reader to Querejeta et al. (2021) for a comprehensive empirical characterization of the molecular gas and star formation properties in different galactic environments of PHANGS galaxies.

4.3. CO and Hα Flux in Single-tracer and Overlap Regions

In this section, we explore whether there is any difference between regions where both tracers are observed (*Overlap*) and regions where only one tracer is observed (*CO-only* and *Hα-only*). We estimate the fractional contribution of *CO-only* (i.e., only one tracer is observed) and *Overlap* (two tracers are observed; *CO-overlap*) to the total *CO sight lines*, and the fractional contribution of *Hα-only* and *Overlap* (*Hα-overlap*) to the total *Hα sight lines*. In other words, the sum of *CO-only* and *CO-overlap* is normalized to 100%, and so is the sum of *Hα-only* and *Hα-overlap*. To compare with the results based on the number of sight lines (our default fraction), the corresponding fractions for *flux* are also estimated.

Figure 8(a) shows the comparison of sight-line fractions with flux fractions. Specifically, for each data point, the values on the *x*- and *y*-axes are calculated based on exactly the same pixels (sight lines), but the *x*-axis shows their fractional contribution to the total sight line of the tracer and the *y*-axis shows their fractional contribution to the total flux of the tracer. The black line indicates a one-to-one correlation.

The median sight-line fractions of *CO-only* and *CO-overlap* are approximately equal (*x*-axes in the upper panels of Figure 8(a)), but the latter contributes a larger portion to the overall flux (66%; *y*-axis of the upper-right panel). Nonetheless, *CO-only* regions still contribute one-third of the CO flux (33%; *y*-axis of the upper-left panel). The difference between the fractions by the number of sight lines and by flux is larger for Hα, as shown in Figure 8(a) (lower panels). Taking all the pixels in our galaxies, *Hα-only* accounts for 36% of the area of Hα-emitting regions but

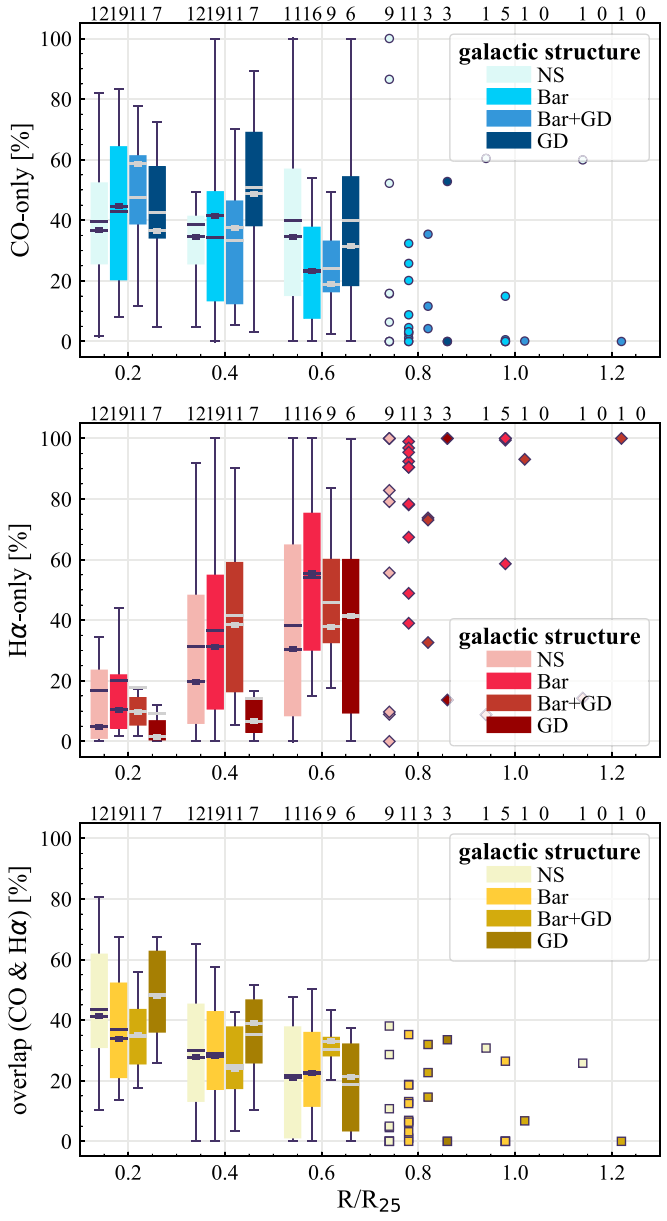

Figure 7. Different radial sight-line profiles for galaxies with different galactic structures at 150 pc resolution. The abbreviations are as follows: NS—galaxies without structures (bar or grand-design spiral arms); Bar—galaxies with a bar but without grand-design spiral arms; Bar+GD—galaxies with both bar and grand-design spiral arms; and GD—galaxies with grand-design spiral arms only. The plot style is analogous to Figure 5. The figure implies the importance of galactic dynamics in regulating star formation.

contributes only ∼14% of the Hα flux. On the other hand, *Hα-overlap* contributes 85% to the total Hα flux, and it is higher than the 64% sight-line fraction. Because the *Hα-overlap* regions are by definition cospatial with CO-emitting molecular gas, they likely suffer from dust attenuation that we do not account for in the processing of our Hα maps due to the lack of extinction tracers (Section 2.2). Therefore, the true flux contribution of *Hα-overlap* is probably higher.

While covering only a small area, galaxy centers often substantially contribute to the total flux (Querejeta et al. 2021). Because the flux in the central region of galaxies is not necessarily associated with star formation, we therefore repeat the analysis while excluding the central 2 kpc in deprojected diameter (Figure 8(b)). For CO, the agreement between area and flux is much tighter; the deviation from the one-to-one line for high CO fractions almost vanishes, implying that galactic centers drive the difference. On the other hand, Hα fractions appear less dominated by the centers. This is at least partially due to the higher extinction present in the centers. The trend of higher flux in *Hα-overlap* regions than in *Hα-only* regions persists even when excluding the centers.

Figure 9 compares the fractions by the number of sight lines (upper panel) and flux (lower panel) for galaxies in different M_* and Hubble-type bins. The distributions of *CO-only* and *CO-overlap* are shown by blue and green boxes, respectively, while *Hα-only* and *Hα-overlap* are shown by red and orange boxes. For each M_* or Hubble-type bin (indicated by the darkness of the boxes), the sum of a data point in the blue (red) box and the corresponding data point in the green (orange) box is normalized to 100. The median and mean for each M_* and Hubble-type bin are summarized in Table 8. The trends with M_* and Hubble type are the same for sight lines and flux, but the difference among the M_* and Hubble-type bins are slightly larger when considering flux instead of the number of sight lines. For all M_* and Hubble-type bins, the *Overlap* regions contribute to a larger proportion of CO and Hα flux than regions with only one type of emission.

Interestingly, *CO-only* becomes dominant in the highest-M_* galaxies, occupying ∼60% of the CO-emitting regions. However, they are almost as equivalently low in flux contribution as other populations, implying a generally (i.e., more extended distributed) low H_2 surface density in the highest-M_* galaxies in our sample. The same feature is seen for the earliest-type galaxies, hinting that star formation ceases to prevail over a significant area of a galaxy while gas remains there. However, we cannot rule out that this result arises from our methodology. Some *CO-only* gas in the low-mass galaxies may not pass our threshold due to its intrinsically low Σ_{H_2}, while in higher-mass galaxies, their *CO-only* gas is slightly brighter than our threshold. This would potentially add many CO-emitting sight lines but very little flux. Such a possibility again highlights the differences in molecular gas properties among galaxies with different M_* and Hubble types.

In summary, at 150 pc spatial scale, the fluxes of CO and Hα emission are higher in *Overlap* regions where emission from both tracers is observed compared to regions where only one tracer is observed, consistent with the finding of Paper I. This trend holds for galaxies with different M_* and Hubble type. Nonetheless, the contribution from regions with only one tracer (*CO-only* and *Hα-only*) to the total flux remains substantial for most systems.

4.4. Distributions of CO and Hα as a Function of Spatial Scale

We investigate the impact of spatial scale on the distributions of CO and Hα emission. Figure 10 shows the sight-line fractions for individual galaxies as a function of spatial scale from 150 pc to 1.5 kpc. For most of the galaxies, their *CO-only* sight lines decrease to $\lesssim$20% at spatial scales $\gtrsim$800 pc, regardless of their *CO-only* fractions at a spatial scale of 150 pc. The *Overlap* regions substantially increase and become the dominant sight lines when resolution is degraded. This is the case for all galaxies in our sample, and the vertical ordering of *Overlap* fractions among the galaxies is almost maintained until 1.5 kpc resolution. At the lowest resolution we consider, more than half of the regions are populated by both CO and Hα emission in most galaxies. While the variations of *CO-only* and *Overlap* sight-line fractions with spatial scale are rather uniform across the sample, the relation between the *Hα-only* fractions and spatial scale is more diverse.

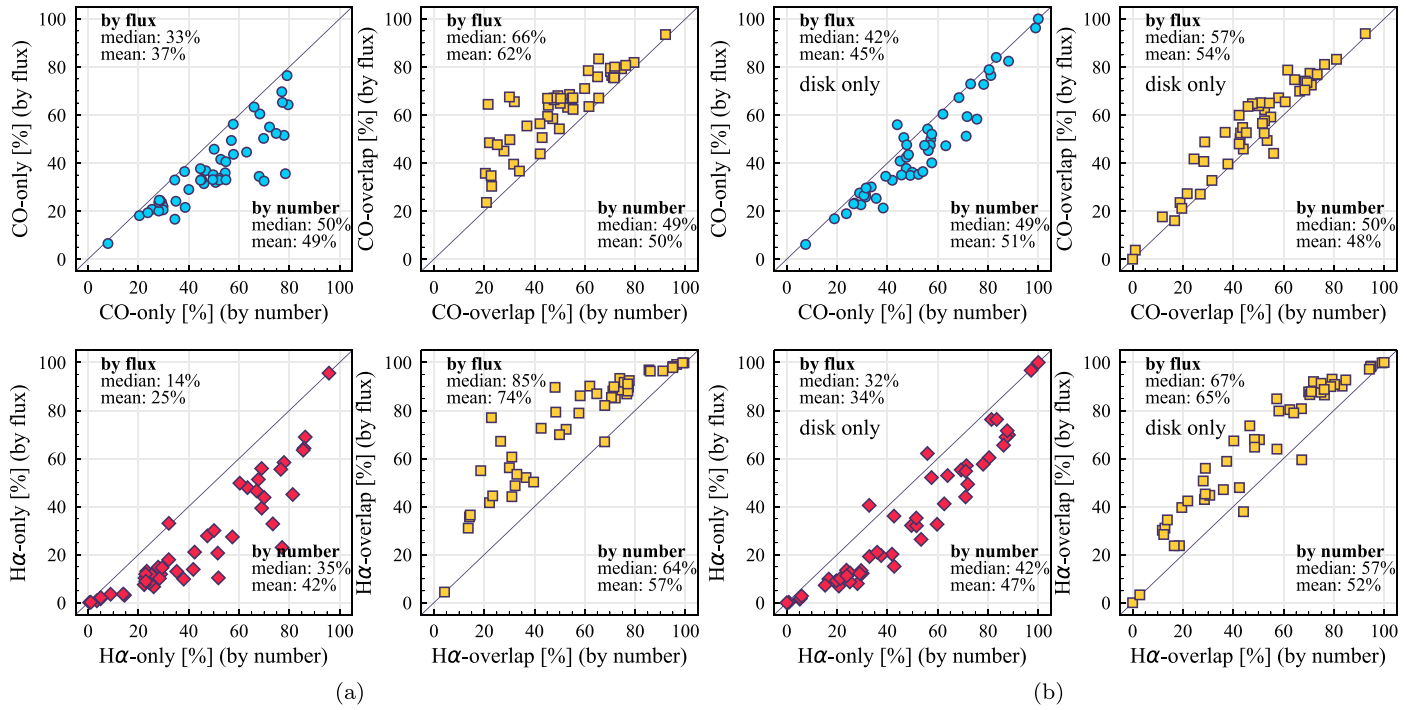

Figure 8. Comparison of the fractions of sight line (*x*-axis) and flux (*y*-axis) per tracer at 150 pc scale. We estimate the fractional contribution of *CO-only* (i.e., only one tracer is observed) and *Overlap* regions (two tracers are observed; *CO-overlap*) to the total number of sight lines with CO and total CO flux, and the fractional contribution of *Hα-only* and *Overlap* regions (*Hα-overlap*) to the total Hα sight line and flux. In other words, the sum of *CO-only* and *CO-overlap* is normalized to 100, and so is the sum of *Hα-only* and *Hα-overlap*. Specifically, for each data point, the values on the *x*- and *y*-axes are calculated based on exactly the same pixels (sight lines), but the *x*-axis shows their fractional contribution to all sight lines of the tracer and the *y*-axis shows their fractional contribution to the total flux of the tracer. The solid line indicates the one-to-one correlation. Panels (a) show the comparisons within the fiducial field of view of the 150 pc resolution images, and panels (b) present the results excluding the central 1 kpc (radius) regions. Overall, the fluxes of CO and Hα emission are higher in *Overlap* regions where emissions from both tracers are observed compared to regions where only one tracer is observed.

Specifically, galaxies with low *Hα-only* fractions at 150 pc scale exhibit a low, roughly constant fraction toward large spatial scales (lower resolution); galaxies with the highest *Hα-only* fractional percentages at the best 150 pc scale decrease rapidly toward low resolutions; and some galaxies show increasing *Hα-only* fractions with decreasing resolutions. For all sight-line categories, the variations with spatial scale become less evident at >500 pc resolution. The flattening point determines the critical resolution at which we stop resolving the CO and Hα distributions.

Figure 11 sheds light on the nature of the different *Hα-only* versus spatial scale relation. These figures are analogous to Figure 10, except that now galaxies are binned by their M_* and Hubble type. The high global *Hα-only* fractions at 150 pc scale, which tend to be relatively isolated toward the outer parts of low-M_* and/or later-type galaxies, become quickly contaminated by other types of sight lines in the inner regions when the resolution is lowered. In other words, we see that the *CO-only* and *Overlap* regions increase in size and expand toward outer disks when the resolution decreases, e.g., NGC 2090, NGC 2835, and NGC 4951 in Figure B1), leading to a rapid decrease of the *Hα-only* fraction as a function of increasing spatial scale. On the other hand, the *Hα-only* fraction of galaxies with low-*Hα-only* is less sensitive to resolution. They tend to be higher-M_* galaxies. Their *Hα-only* sight lines populate both outer and/or inner disks (e.g., interarm regions, NGC 1300 and NGC 4321 in Figure 2 and NGC 2997 and NGC 3627 in Figure B1). Whether a galaxy's *Hα-only* fractions increase or decrease with resolution depends on the relative distribution of gas traced by CO and Hα.

By contrast, *CO-only* sight lines vary relatively uniformly as a function of spatial scale among different galaxy populations. The profiles show a clear ranking with M_* and Hubble type at spatial scale <500 pc. At spatial scale $\gtrsim$500 pc, the dependence of the *CO-only* fraction on M_* and Hubble type becomes less pronounced. While we find no strong dependence of *Overlap* regions with M_* at a resolution of 150 pc (Figure 4), Figure 11 shows that galaxies in the highest-M_* bin tend to have lower *Overlap* fractions when the spatial scales are larger than ∼300 pc. On the other hand, the trend with Hubble type at 150 pc resolution only holds when the spatial scale is smaller than ∼500 pc.

In summary, the results of this section demonstrate the important role that spatial scale can play when characterizing the distribution of CO and Hα emission and their dependence on host-galaxy properties. The trend between sight-line fractions and spatial scale was also observed in Paper I for individual galaxies; here we further show that the resolution dependence depends on galaxy type and the underlying high-resolution CO and Hα emission structure, indicating that there may be no simple (universal) prescription to infer the physical connection between gas and star formation from kiloparsec-scale measurements.

5. Discussion

We have analyzed a sample of 49 resolution-matched CO and Hα maps, which trace molecular gas and high-mass star formation, respectively. At the best resolution we consider,

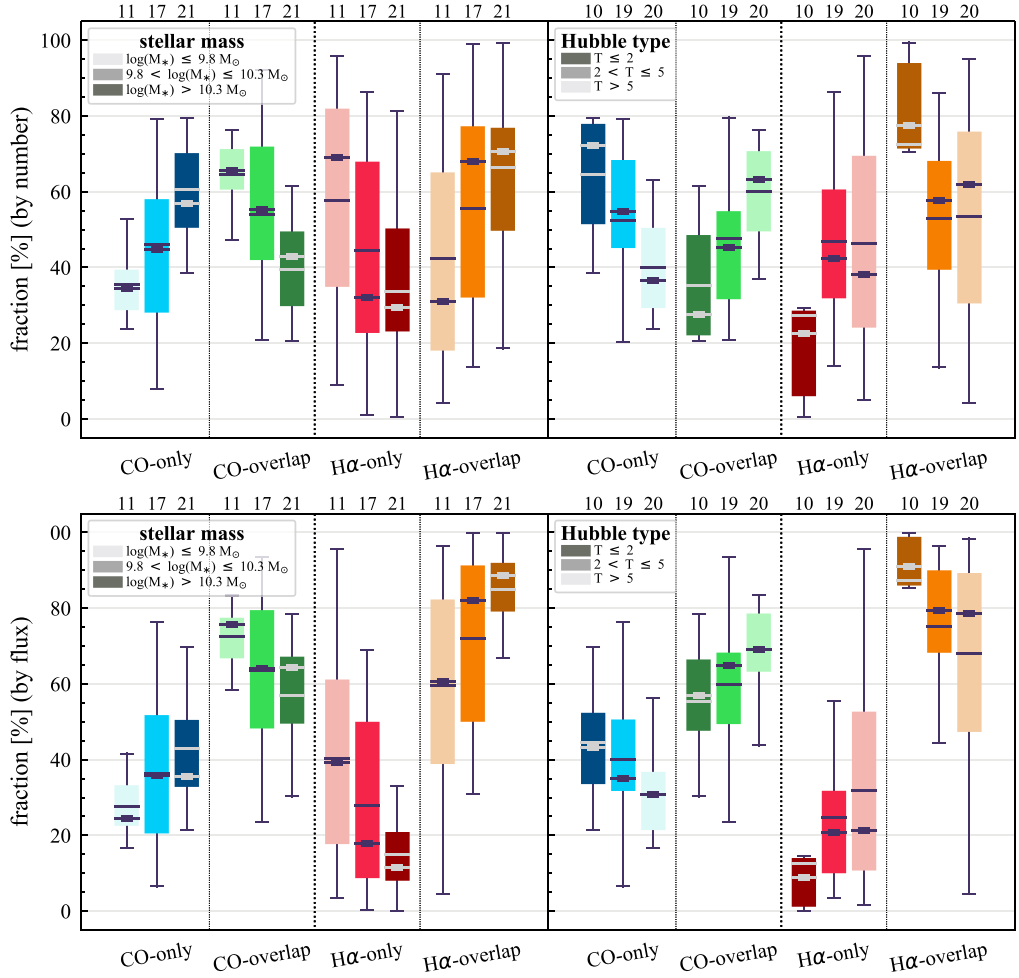

Figure 9. Fractional contribution to the number of sight lines (top row) and flux (bottom row) per tracer for different stellar-mass bins (left column) and Hubble types (right column) at 150 pc resolution. For each panel, CO and Hα are shown on the left-hand and right-hand sides, respectively. *CO-only CO-overlap*, *Hα-only,* and *Hα-overlap* are shown in blue, green, red, and orange, respectively. As in previous figures, the color darkness of the boxes increases with increasing M_* and decreasing Hubble-type value. For a given galaxy in a given M_* or Hubble-type bin, the sum of values in the blue and green boxes (i.e., CO without and with Hα) is normalized to 100, and the sum in red and orange ones (i.e., Hα without and with CO) is also normalized to 100. It is true for all M_* and Hubble-type bins that *Overlap* regions contribute to a larger proportion of CO and Hα flux than regions with only one type of emission.

Table 8
Median (Mean) Fractions of Sight Lines and Flux per Tracer for Different Stellar-mass and Hubble-type Bins at 150 pc Resolution

	$\log(M_*/M_\odot) \leqslant 9.8$	$9.8 < \log(M_*/M_\odot) \leqslant 10.3$	$\log(M_*/M_\odot) > 10.3$
	Sight line % median (mean) flux % median (mean)		
CO-only	34 (35) **24** (**28**)	45 (46) **36** (**36**)	57 (61) **36** (**43**)
CO-overlap	66 (65) **76** (**72**)	55 (54) **64** (**64**)	43 (39) **64** (**57**)
Hα-only	69 (58) **39** (**41**)	32 (44) **18** (**28**)	29 (34) **11** (**15**)
Hα-overlap	31 (42) **61** (**59**)	68 (56) **82** (**72**)	71 (66) **89** (**85**)
	$T \leqslant 2$	$2 < T \leqslant 5$	$T > 5$
	Sight line % median (mean) flux % median (mean)		
CO-only	72 (65) **43** (**45**)	55 (52) **35** (**40**)	37 (40) **31** (**31**)
CO-overlap	28 (35) **57** (**55**)	45 (48) **65** (**60**)	63 (60 **69** (**69**)
Hα-only	22 (27) **09** (**13**)	42 (47) **21** (**25**)	38 (46) **21** (**32**)
Hα-overlap	78 (73) **91** (**87**)	58 (53) **79** (**75**)	62 (54) **79** (**68**)

Note. Regular and bold fonts denote the fraction of the number of sight lines and flux, respectively. Note that for each individual galaxy, the sum of *CO-only* and *CO-overlap* is normalized to 100 and so is the sum of *Hα-only* and *Hα-overlap* (see the text for details).

150 pc, we find that the distributions of both CO and Hα emission depend on galaxy stellar mass and Hubble type (Section 4.1). Specifically, the *CO-only* fractions increase with stellar mass and earlier Hubble type, while the converse is seen for *Hα-only* fractions. The fraction of *Overlap* regions remains roughly constant with both quantities.

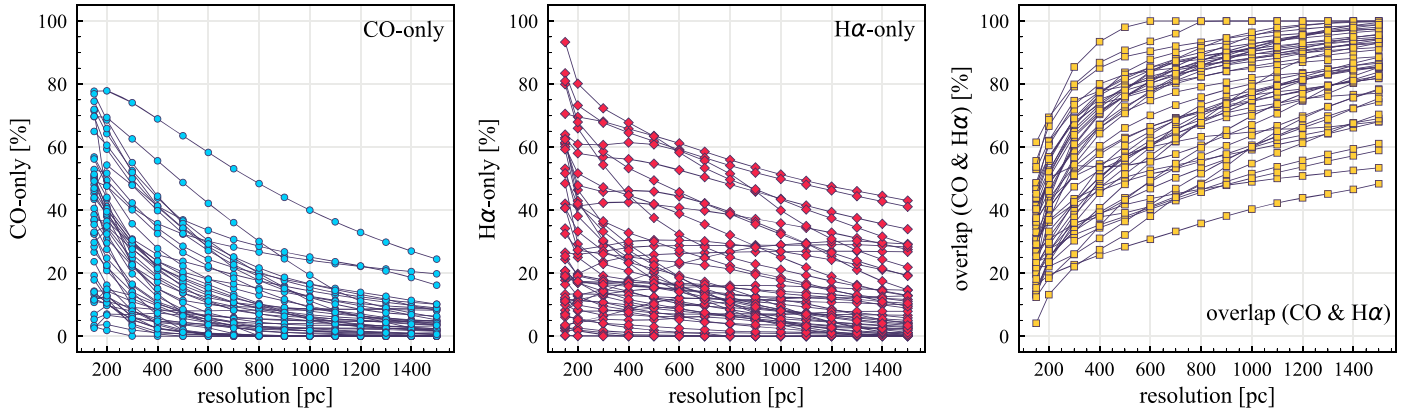

Figure 10. Fractions of sight lines as a function of spatial scale (observing resolution) from 150 pc to 1.5 kpc for each individual galaxy (i.e., one line per galaxy). From left to right, the panels show the variation of *CO-only* regions, *Hα-only* regions, and CO and Hα *Overlap* regions, respectively. The variations of *CO-only* and *Overlap* sight-line fractions with spatial scale are rather uniform across the sample, while the relation between *Hα-only* fractions and spatial scale is more diverse.

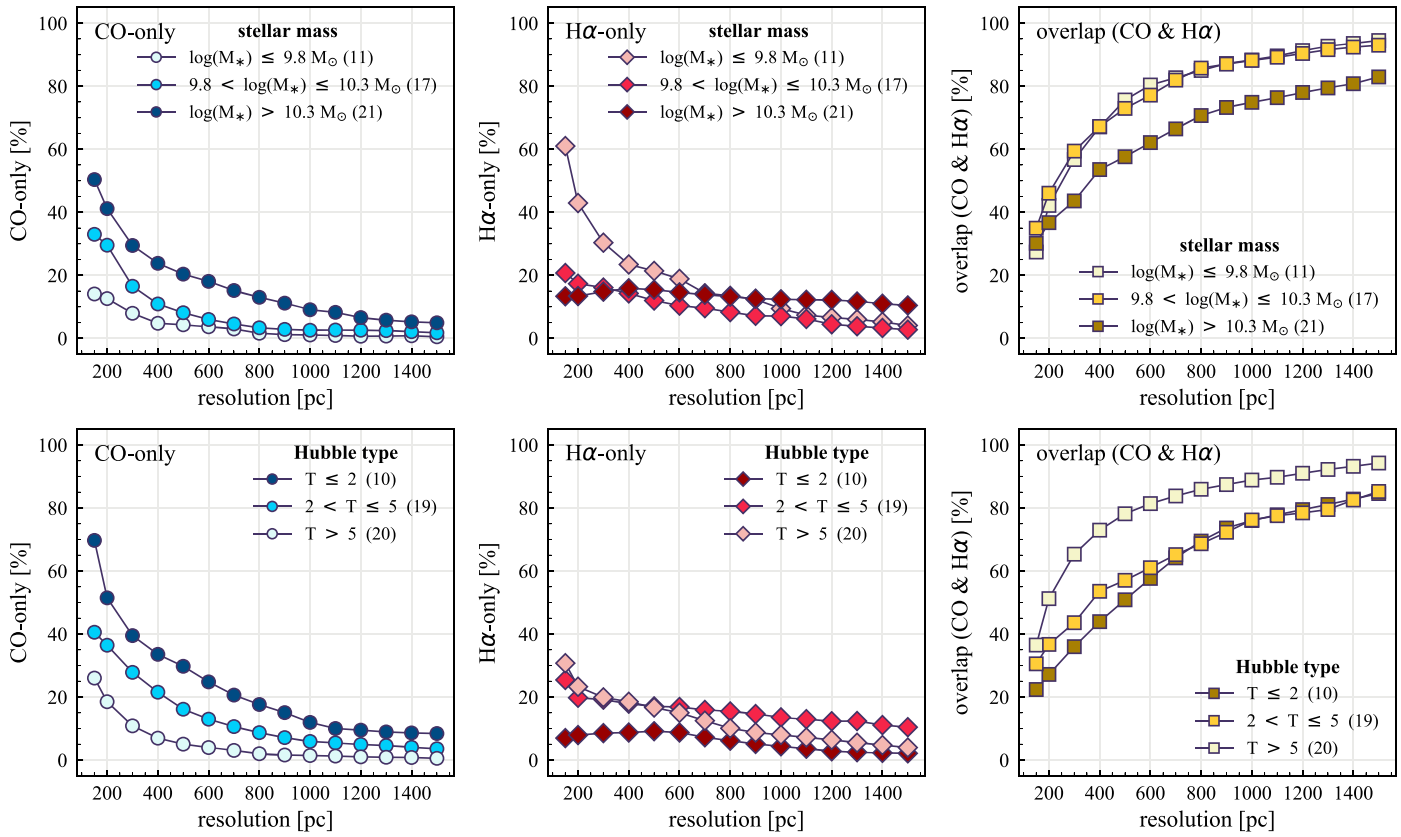

Figure 11. Fractions of sight lines as a function of spatial scale (observing resolution) in different stellar-mass (top row) and Hubble-type (bottom row) groups. From left to right, the three columns show the variation of *CO-only* regions, *Hα-only* regions, and CO and Hα *Overlap* regions. The figures demonstrate the important role that observing resolution can play when characterizing the distribution of CO and Hα emission and their dependence on host-galaxy properties.

Galactic structures act as an additional factor controlling the distribution of the CO and Hα emission (Section 4.2). GD galaxies exhibit a distinct sign of higher *CO-only* and *Overlap* fractions and lower *Hα-only* fractions than the other populations; galaxies with a bar (Bar and Bar+GD) visually show stronger radial dependence of *CO-only* sight lines than galaxies without a bar (NS and GD).

However, probing the dependence of CO and Hα distributions on galaxy properties requires observations with a resolution high enough to distinguish between regions where only one tracer is observed and regions where both tracers are observed (Section 4.4). Our results also show that, at 150 pc resolution, both CO and Hα tend to have higher flux in regions where both CO and Hα are found (*Overlap*) than in regions where only a single tracer (*CO-only* and *Hα-only*) can be found (Section 4.3).

5.1. CO-only *Sight Lines*

We find that galaxies in our sample contain a substantial reservoir of *CO-only* molecular gas not associated with optical

tracers of high-mass star formation (or above SFR surface densities of $\sim 10^{-3}$–10^{-2} $M_\odot$ yr^{-1} kpc^{-2} depending on the galaxy target). Our result is qualitatively consistent with studies of Local Group galaxies. In these galaxies (the Small and Large Magellanic Clouds (SMC and LMC) and M33), about 20%–50% of GMCs are not associated with H II regions or young clusters[32] (e.g., Mizuno et al. 2001; Engargiola et al. 2003; Kawamura et al. 2009; Gratier et al. 2012; Corbelli et al. 2017). Our results further reveal that these starless clouds are not restricted to lower-mass spiral and irregular galaxies, as in the Local Group, but are observed across the whole range of the galaxy population.

Non-star-forming gas: The sensitivity of PHANGS-ALMA is able to detect GMCs with a mass of $\gtrsim 10^5$ $M_\odot$; moreover, the *CO-only* sight lines are found at all surface densities from the adopted threshold to a few thousands of $M_\odot$ pc^{-2}. Massive star formation is certainly expected to proceed in these relatively high-mass and high-density regions. This implies that part of the *CO-only* gas consists of non-star-forming clouds; the gas is unable to form stars because of its intrinsic properties. For example, molecular gas in some *CO-only* regions might be a diffuse, dynamically hot component (Pety et al. 2013) that is not prone to star formation or may be analogous to the gas in the centers of early-type (elliptical) galaxies that do not seem to be forming stars (Crocker et al. 2011; Davis et al. 2014). Nonetheless, we note that although the non-star-forming gas does not currently participate in the local ongoing star formation cycle, it may participate in star formation at some point in the future, i.e., made possible by relocating to a different, favorable site in the galactic potential that prompts a change in its dynamical state and/or organization, for example.

Low-mass star formation: It is possible that high-mass star formation is suppressed in the *CO-only* regions, forming stars that are not massive enough to produce detectable Hα emission. Such molecular clouds have been found in the LMC (Indebetouw et al. 2008).

Embedded star formation: Massive stars may be formed in part of the *CO-only* gas, but their Hα emission is obscured by dust. However, the embedded phase is relatively short, lasting only for a few to several megayears (Kim et al. 2021), and therefore may not account for all *CO-only* regions.

Pre- and/or post-star formation: The *CO-only* gas might be in the process of collapsing or may be remnant molecular gas dispersed from previous star-forming sites by stellar feedback (e.g., photoionization, stellar winds, and supernova explosions).

Distinguishing these scenarios requires the analysis of multiwavelength data, such as line widths and surface densities of molecular clouds, dense gas tracers, better tracers of obscured star formation (e.g., infrared emission), and extinction tracers, but such an analysis is beyond the scope of this paper. Future James Webb Space Telescope (JWST) observations will also provide crucial insight into the complex processes of star formation and the nature of our *CO-only* sight lines.

In Section 4.4, we saw that the observed sight-line fractions depend on spatial scale. We repeated our analysis for a subsample of 17 galaxies for which our observations achieve a common 90 pc resolution to test whether the fraction of *CO-only* sight lines in galaxies is larger at even higher physical resolution. A CO threshold of $13\,M_\odot$ pc^{-2} is adopted, corresponding to the 3σ of the lowest sensitivity of these galaxies at 90 pc resolution. The *CO-only* fractions in all galaxies show an increase by $\sim$14% (median) as the resolution improves from 150 to 90 pc, while the fraction of *Hα-only* and *Overlap* regions for the 90 pc maps decreases by $\sim$4% and 8%. This suggests that there remains a non-negligible fraction of *CO-only* gas that is not well resolved at our fiducial scale of 150 pc. If we increased the resolution even more, e.g., to 10 pc, we might expect to find even more *CO-only* sight lines, but testing this will require higher-resolution ALMA observations. At some point, such observations will highly resolve individual clouds or other star-forming structures, and we might even detect that individual regions within a molecular cloud remain quiescent (e.g., genuinely non-star-forming or pre-star-forming) while stars already form elsewhere. This is not yet the case for our data, however.

5.2. Effect of Galactic Dynamics

Both bar and GD spiral arms are known to stabilize the gas against collapse and thus star formation under certain circumstances (Reynaud & Downes 1998; Zurita et al. 2004; Verley et al. 2007; Meidt et al. 2013). However, while we indeed observe a higher fraction of *CO-only* sight lines in GD spiral galaxies (Figure 6), the *CO-only* fractions of Bar and Bar+GD are comparable to those of NS galaxies. It is probably because we do not consider bar strength in this work, which is known to be correlated with the SFR and star formation history of galaxies (Martinet & Friedli 1997; Carles et al. 2016; Kim et al. 2017). An alternative explanation could be that the gas distribution in barred galaxies is evolving heavily over time (e.g., Donohoe-Keyes et al. 2019), leading to a wide variety in the gas distribution in the barred galaxies seen in PHANGS (Leroy et al. 2021c).

Nonetheless, our results show a possible trend for galaxies with bars (Bar and Bar+GD) to exhibit a stronger radial dependence in the fraction of *CO-only* sight lines (Figure 7). This may be attributed to bar-driven gas inflows that increase the gas concentrations in the central regions (Sakamoto et al. 1999; Sheth et al. 2005; Sun et al. 2020b). Moreover, the Bar and Bar+GD galaxies show a weaker radial dependence of the *Overlap* fraction than the NS and GD galaxies in terms of median values. Star-forming complexes are often observed at bar ends. Although bar footprints are not necessarily forming stars, the star-forming bar ends may smooth the profiles of the *Overlap* sight lines (James et al. 2009; Beuther et al. 2017; Díaz-García et al. 2020). Finally, we note that we did not control for other trends (e.g., M_*) when comparing sight-line fractions between galaxies with different structures. A very large sample is required in order to distinguish the effects of global galaxy properties and galactic dynamics.

Some galaxies show a pronounced offset between the different sight-line types with a sequence of *CO-only* to *Overlap* and to *Hα-only* when going from up- to downstream (assuming the spiral arms are trailing, e.g., NGC 4321 in Figure 2 and NGC 0628, NGC 1566, and NGC 2997 in Figure B1), consistent with expectations for a spiral density wave (see Figure 1 of Pour-Imani et al. 2016). These offsets are almost exclusively found in well-defined GD spiral arms and presumably lead in turn to the high (or even highest) *CO-only* fraction in the disk (0.4 and 0.6 R_{25}) of GD in Figure 7, suggesting that most GD structures may indeed be density

[32] Note that one should not compare the fraction of non-star-forming "GMCs" in the Local Group galaxies with our "sight-line" fractions directly due to the different counting methods, i.e., object-based or pixel-based approaches. Direct comparison is only possible if we assume that GMCs have a fixed size, which is unlikely to be true (e.g., Hughes et al. 2013; Colombo et al. 2014; Rosolowsky et al. 2021).

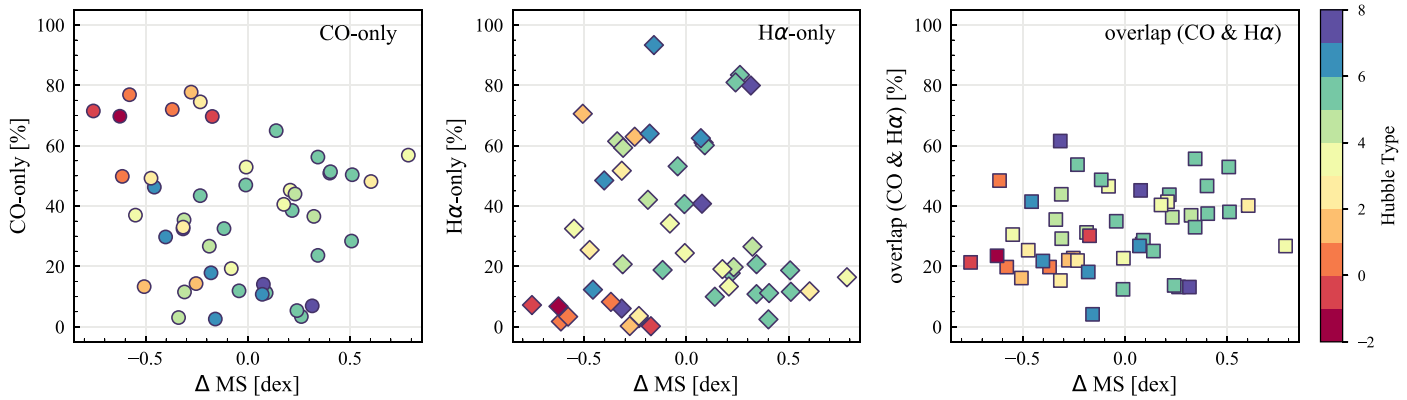

Figure 12. Fractions of sight lines at 150 pc resolution vs. ΔMS, color-coded by Hubble type. From left to right, the three panels show the results for *CO-only* regions, *Hα-only* regions, and CO and Hα *Overlap* regions, respectively. We find no correlation between the global sight-line fractions with ΔMS. Correlation coefficients of each sight-line category relative to ΔMS are given in Table 5.

waves. This demonstrates the potential of the sight-line method as a diagnostic of the relationship between ISM condition and galactic dynamics. Detailed analysis of individual galaxies would be necessary to confirm the (dynamical) nature of our GD spiral arms.

Besides, the offsets between molecular gas and star formation tracers also allow the measurement of the angular rotation velocity of a spiral pattern and the timescale for star formation (e.g., Egusa et al. 2004, 2009; Louie et al. 2013). While such analyses have been restricted to small-sample studies in the past, PHANGS allows for a systematic exploration of the spatial offset between the gas spiral arms and star-forming regions. Some barred galaxies also exhibit such *CO-only* and *Overlap* offsets along their spiral arms, e.g., NGC 4321 and NGC 3627 in Figure 2 and NGC 1365 in Figure B1, suggesting a dynamical link between spiral arms and stellar bar (Meidt et al. 2009; Hilmi et al. 2020).

5.3. Sight-line Fractions and Star Formation

We find no correlation between sight-line fractions and star formation properties (Section 4.1.1) and no correlation with the fractions of flux contributed by the *CO-only*, *Hα-only*, *CO-overlap*, and *Hα-overlap* regions (correlation coefficients $\lesssim$0.2). Figure 12 shows the sight-line fractions against ΔMS, color-coded by Hubble type. Although there is no statistical relationship between the sight-line fractions and ΔMS, galaxies with low ΔMS in our sample, $\lesssim -0.58$ dex or ∼4 times below the main sequence (NGC 1317, NGC 3626, NGC 4457, and NGC 4694), tend to have high *CO-only* sight-line fractions (∼50%–80%). These low-ΔMS galaxies are all earlier types with Hubble type $T \leqslant 1$ (S0–Sa). The spatial distribution of their *CO-only* regions is relatively compact inner disks, analogs to the molecular gas in elliptical galaxies (e.g., Crocker et al. 2011; Davis et al. 2014). In contrast, among the six highest-ΔMS galaxies (>0.4 dex or 2.5 times above the main sequence) in our sample, four show relatively high *CO-only* sight-line fractions ($\gtrsim$50%; NGC 1365, NGC 1559, NGC 4254, and NGC 5643). All these high-*CO-only* and high-ΔMS galaxies have GD spiral arms and/or a bar; moreover, their *CO-only* sight lines follow well these galactic structures, implying a dynamic origin of the high *CO-only* fractions. Although both galaxies with the highest- and lowest-ΔMS in our sample show substantial CO-emitting regions not associated with star formation, the spatial distribution of their *CO-only* regions is markedly different, potentially pointing to different underlying causes for the suppressed star formation in these regions.

The other two highest-ΔMS galaxies (NGC 1385 and NGC 1511) have lower, but not necessarily low, *CO-only* fractions (28% and 48%). Both of them happen to be peculiar systems. In fact, four out of the six highest-ΔMS galaxies (NGC 1365, NGC 1385, NGC 1511, and NGC 4254) show signs of interactions with other galaxies.

In our working sample, 33 galaxies show signs of interactions in terms of their morphology. The median *Overlap* sight-line fraction of the merger candidates (28%) is slightly lower than that of isolated galaxies (36%). However, the *Overlap* sight lines in the merger candidates contribute a higher fraction of flux (90%) to the total Hα flux than the apparently undisturbed galaxies (73%). Taking these numbers at face value, a given unit of the star-forming region (*Overlap*) in merger candidates contributes more significantly to the total SFR of a galaxy than a given unit of a star-forming region in undisturbed galaxies, assuming that all the Hα emission is powered by star formation. We should note that galaxy interactions may trigger the central AGN (e.g., Ellison et al. 2019) and shocks prevailing over the disks, which could contribute to Hα emission. However, we are not able to cleanly separate H II regions from other Hα-emitting sources when using only narrowband data. Spectroscopic observations are necessary to confirm the differences between merger candidates and undisturbed galaxies.

5.4. Hα Sight Lines at Large Galactocentric Radii

The *Hα-only* sight lines are preferentially found at large galactocentric radii and even become dominant at $R > 0.4\,R_{25}$ ($\geqslant$60%) in low-M_* galaxies. Moreover, the fraction of *Hα-only* sight lines is always higher for low-M_* galaxies than higher-M_* galaxies at all radii (Figure 5). The lack of *CO* sight lines at large radii may be due to (1) the lack of gas and/or (2) the existence of low-Σ_{H_2} gas that drops below our applied Σ_{H_2} threshold (Section 3.2).

To gain insight into the extent of cold gas reservoirs in our galaxies, we compute the radial profiles of gas fractions (f_{gas}) and molecular-to-atomic gas-mass ratio (R_{mol}) for galaxies that have spatially resolved measurements of atomic gas and stellar-mass surface densities ($\Sigma_{H\,I}$ and Σ_*). f_{gas} is defined as the ratio of the total gas mass ($\Sigma_{H_2} + \Sigma_{H\,I}$) to Σ_*, while R_{mol} is defined

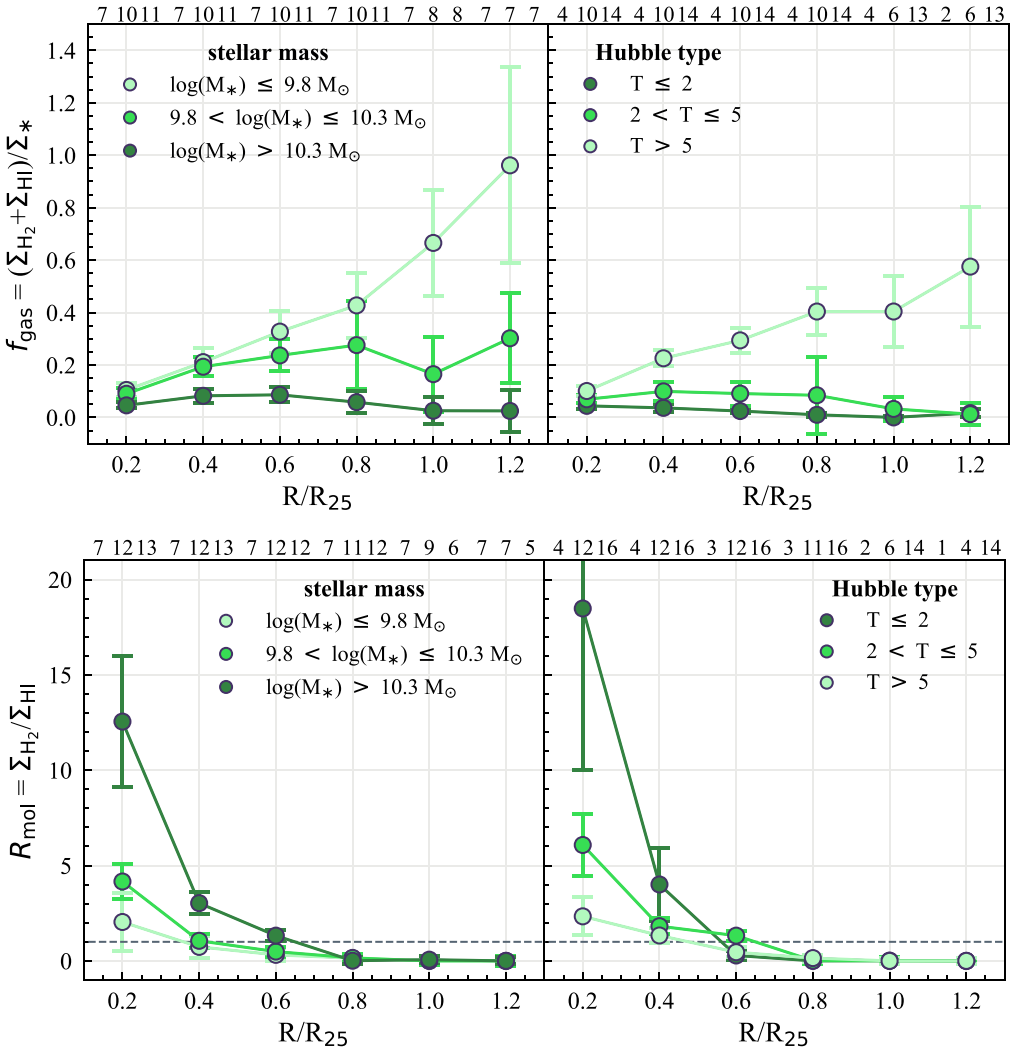

Figure 13. Radial ISM properties for different bins of stellar mass (left) and Hubble type (right). The top and bottom rows show the radial gas fraction ($f_{\rm gas}$) and molecular-to-atomic gas-mass ratio ($R_{\rm mol}$), respectively. The dashed lines in the bottom panels indicate $R_{\rm mol} = 1.0$. The symbol darkness is proportional to M_* or Hubble type. The error bars represent the error of the mean. The figure is created for the subsample of galaxies that have spatially resolved H I and stellar-mass measurements. At the $R > 0.4\,R_{25}$ regime where *Hα-only* regions dominate the sight lines in lower-mass galaxies, there is still a significant reservoir of gas with respect to stellar mass ($f_{\rm gas} \gtrsim 0.2$), but the gas is predominantly atomic ($R_{\rm mol} < 1$).

as the ratio between $\Sigma_{\rm H_2}$ and $\Sigma_{\rm H\,I}$. The spatially resolved H I data are taken from various sources in the literature, including the PHANGS-VLA (D. Utomo et al. 2022, in preparation), VLA THINGS (Walter et al. 2008) and VIVA (Chung et al. 2009) surveys, and VLA archive. The spatially resolved Σ_* is measured from Spitzer IRAC 3.6 μm or WISE 3.4 μm (Leroy et al. 2019, 2021c). The typical resolution of the $\Sigma_{\rm H\,I}$ and Σ_* measurements is 1–2 kpc. Because we are interested in the general trend of the $f_{\rm gas}$ and $R_{\rm mol}$ distributions, high spatial resolution is not needed for this purpose. In total, for 28 and 32 galaxies, we can compute their radial $f_{\rm gas}$ and $R_{\rm mol}$, respectively. For this analysis, we rely on radial measurements at matched kiloparsec resolution from the PHANGS multi-wavelength database presented in Sun et al. (2020b) and J. Sun et al. (2022, in preparation).

Figure 13 shows the radial $f_{\rm gas}$ (upper row) and $R_{\rm mol}$ (lower row) for galaxies with different M_* (left) and Hubble types (right). Our sample shows a gradual decrease of $f_{\rm gas}$ with increasing M_* at all radii. Moreover, $R_{\rm mol}$ increases with M_* (when looking at $R \lesssim 0.6\,R_{25}$). The trends with Hubble types are consistent in the sense that later-type galaxies are less massive. The results in Figure 13 are in good agreement with Saintonge et al. (2011, 2016) based on integrated measurements for a large sample of galaxies

Furthermore, Figure 13 shows that the high-*Hα-only* regime ($R > 0.4R_{25}$) of low-mass galaxies still harbors a significant reservoir of gas with respect to stellar mass ($f_{\rm gas} \gtrsim 0.2$), but the gas is predominantly atomic ($R_{\rm mol} < 1$). Therefore, it is likely that there are molecular clouds in the outer atomic-dominated, high-*Hα-only* regions, but their $\Sigma_{\rm H_2}$ is low and below our applied threshold.

For galaxies with $\log(M_*/M_\odot) > 10.3$, around 70%–98% of the total CO emission (both median and mean are ∼90%) are included in our analysis of sight-line fractions (i.e., $\Sigma_{\rm H_2} > 10\ M_\odot\ {\rm pc}^{-2}$), while the fraction of CO emission above our applied threshold decreases to ∼40%–90% (both median and mean are ∼65%) for $\log(M_*/M_\odot) < 10.3$. We also observe a stronger variation in the *Hα-only* fractions for low-M_* galaxies when lowering the CO threshold while keeping the Hα threshold fixed. These imply a prevalence of lower-mass molecular clouds ($\sim 10^4$–$10^5\ M_\odot$) in lower-mass galaxies and significant galaxy-to-galaxy variations in their molecular cloud properties

(e.g., Hughes et al. 2013; Schruba et al. 2019; Sun et al. 2020a, 2020b; Rosolowsky et al. 2021). The galaxy-to-galaxy variations in cloud properties also lead to correlations, albeit relatively weak, between the sight-line fractions and CO effective sensitivity in Table 5. Moreover, the gas depletion time of molecular gas ($\tau_{\rm dep}$) is found to anticorrelate with galaxy M_*, with lower-M_* galaxies showing shorter $\tau_{\rm dep}$ even after accounting for the metallicity dependence of $\alpha_{\rm CO}$ (Utomo et al. 2018). The $\tau_{\rm dep}$–M_* relation also causes substantial Hα emission not associated with molecular gas in low-M_* galaxies.

Finally, dissociation is presumably more efficient in low-$\Sigma_{\rm H_2}$ environments due to less dust shielding (e.g., Wolfire et al. 2010). Therefore, CO emission is preferentially seen in high-extinction regions (e.g., inner galactic disks). The need for high extinction to form CO may lead to the consequence that the radial profiles of CO are steeper than those of Hα (e.g., Leroy et al. 2008). Because $\Sigma_{\rm H_2}$ decreases rapidly with increasing galactocentric radii, the choice of $\Sigma_{\rm H_2}$ threshold has a significant impact on the *Overlap* fractions at large galactocentric radii, especially for low-M_* galaxies, whose $\Sigma_{\rm H_2}$ are systematically lower (e.g., Hughes et al. 2013; Sun et al. 2020b).

5.5. Relative Timescale of the Gas–Star Formation Cycle

If we assume that all the *CO-only* sight lines are pre-star-forming clouds, the three categories of regions we define roughly sample the evolutionary sequence of star-forming regions, in the sense that a cold molecular gas cloud (*CO-only*) evolves into a star-forming molecular cloud (*Overlap*), and then to a region of (exposed) massive young stars (*Hα-only*) where the molecular gas has been largely dispersed and/or dissociated. In this scenario, the areal fractions that we measure are an approximate reflection of the time spent by a star-forming region in each of these different evolutionary phases. Similar frameworks (i.e., counting the number of GMCs and H II regions) have been applied previously to estimate the duration over which the molecular cloud traced by CO emission is visible in the LMC (Kawamura et al. 2009), constrain the cloud lifecycle in M33 (Gratier et al. 2012; Corbelli et al. 2017), and determine the timescales for dense molecular clumps to evolve from being starless to star-forming in the Milky Way (Battersby et al. 2017).

The evolution of molecular clouds provides constraints on the mechanisms triggering or halting star formation at a specific location in a galaxy. In Paper I, we apply a simple version of the approach to estimate the duration for which the molecular gas traced by CO emission is visible ($t_{\rm gas}$):

$$t_{\rm gas} = t_{\rm H\alpha} \times \frac{f_{\rm CO\text{-}only} + f_{\rm overlap}}{f_{\rm H\alpha\text{-}only} + f_{\rm overlap}} = t_{\rm H\alpha} \times f_{\rm scale}\,, \qquad (3)$$

where $t_{\rm H\alpha}$ represents the duration for which Hα emission from H II regions is visible. $f_{\rm CO\text{-}only}$, $f_{\rm H\alpha\text{-}only}$, and $f_{\rm overlap}$ denote the fractions of *CO-only*, *Hα-only*, and *Overlap* sight lines, respectively. Then, $f_{\rm scale}$ represents the scaling factor to translate from the fiducial timescale, here $t_{\rm H\alpha}$, to $t_{\rm gas}$.[33] We emphasize that, by applying Equation (3), we are implicitly assuming that our individual pixels are discrete star-forming units and all the *CO-only* sight lines contain pre-star-forming clouds (see Section 5.1).

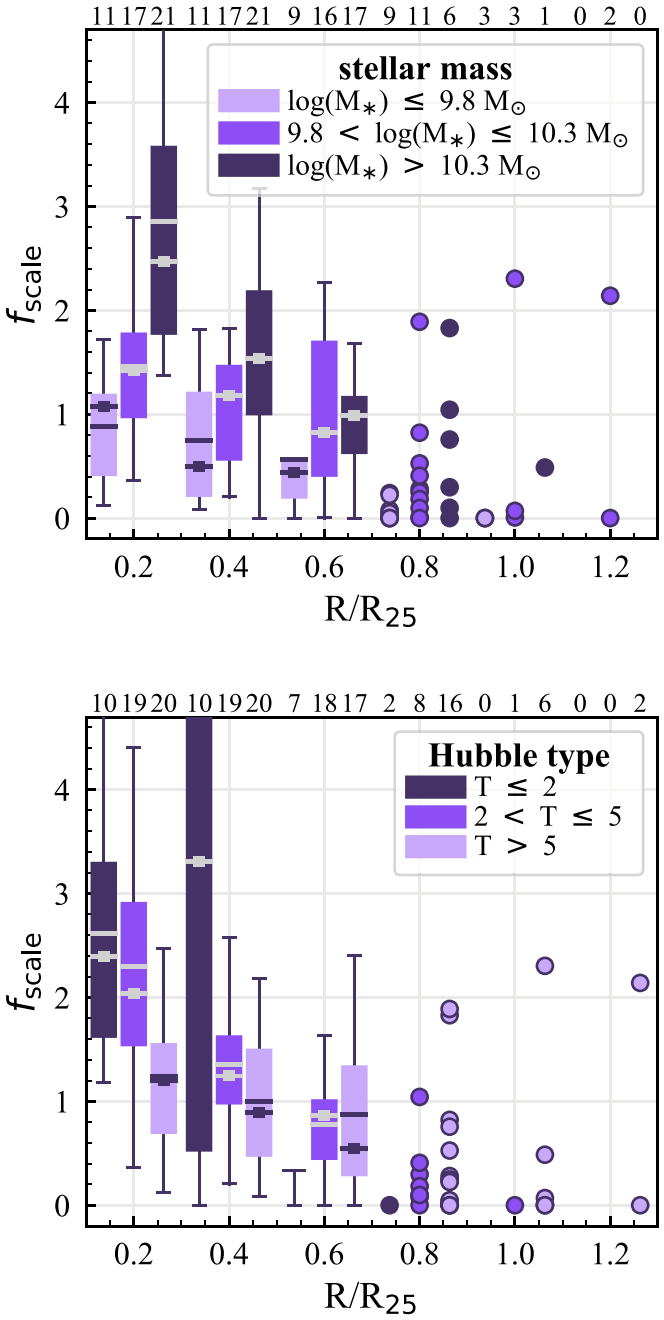

Figure 14. Radial distribution of $f_{\rm scale}$ for different bins of M_* (upper panel) and Hubble type (lower panel) at 150 pc resolution. $f_{\rm scale}$ represents, to first order, the scaling factor to translate from the fiducial timescale $t_{\rm H\alpha}$ (the visibility time of the Hα emission of H II regions; ~5–10 Myr) to the lifetime for a cold gas structure (see the main text for details). The plot style is the same as in Figure 5. There is a ranking of cloud lifetime or $f_{\rm scale}$ along M_*, but the trend with Hubble type is not as strong as that for M_*.

Figure 14 shows the radial trend in $f_{\rm scale}$ averaged in bins of M_* (upper panel) and Hubble type (lower panel).[34] There is a ranking of $f_{\rm scale}$ along M_* where molecular clouds in high-M_*

[33] We note that the cloud visibility time $t_{\rm gas}$ is different from the dynamic timescale or the depletion time. A comparison of various relevant timescales, such as cloud visibility time, freefall time, crossing time, and the characteristic timescale for star formation regulated by galactic dynamical processes has been discussed in Chevance et al. (2020) for a subset of PHANGS galaxies. A further discussion will also be presented in the upcoming paper by J. Sun et al. (2022, in preparation).

[34] $f_{\rm scale}$ has to be calculated in radial bins or in any region-by-region manner, otherwise, $f_{\rm scale}$ is heavily determined by the bright CO in the inner part and bright Hα in the outer part, but those regions do not form part of the same evolutionary cycle.

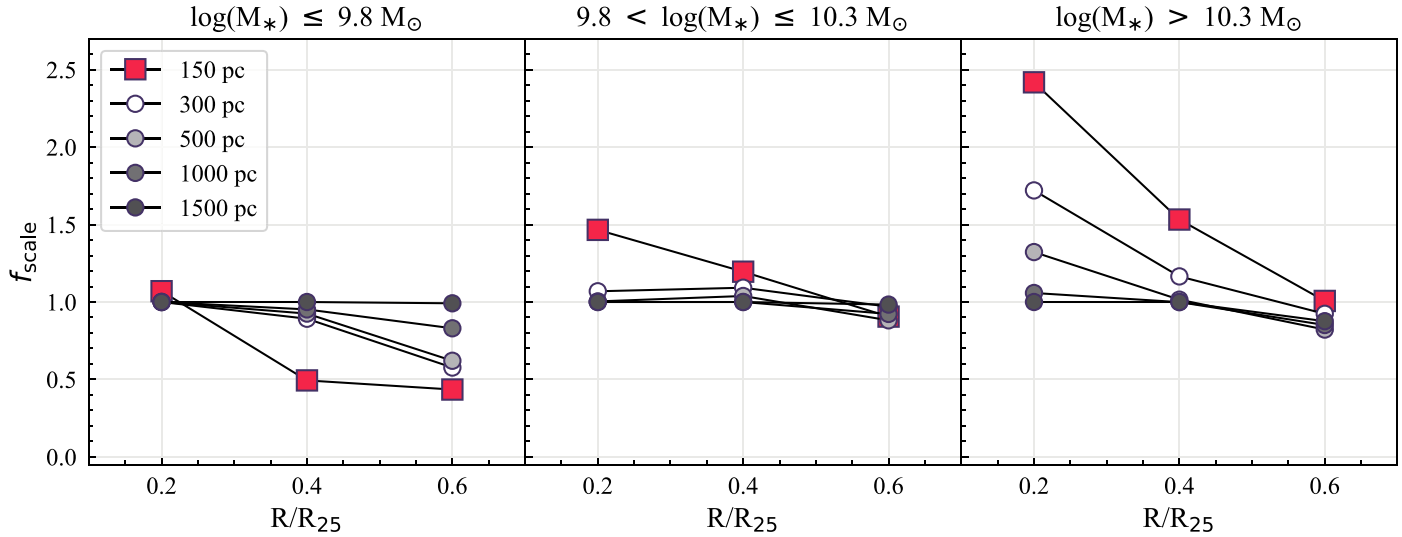

Figure 15. Median radial $f_{\rm scale}$ ($\propto$ cloud lifetime, at least to first order) for different M_* as a function of spatial scale (150, 300, 500, 1000, and 1500 pc). In each panel, the red square represents $f_{\rm scale}$ at our best-matching 150 pc resolution. $f_{\rm scale}$ at other spatial scales is shown by circles, where increasing color darkness resembles increasing spatial scale. At spatial scales $\leqslant$300 pc, there is a visible difference in $f_{\rm scale}$ between galaxy populations, but the differences between galaxies become considerably smaller at spatial scales of >300 pc due to the significant decrease in *CO-only* sight lines and increase in *Overlap* sight lines.

galaxies tend to have longer $f_{\rm scale}$ than clouds in low-M_* galaxies over the radial range probed. Given that typical estimates for $t_{\rm H\alpha}$ are 5–10 Myr (e.g., Kennicutt & Evans 2012; Leroy et al. 2012; Haydon et al. 2020), the $t_{\rm gas}$ of our sample at the 150 pc scale, therefore, decreases from $\sim$5 to 25 Myr for the high-M_* galaxies, to $\sim$5–15 Myr for the intermediate-M_* galaxies, and to a few megayears for the low-M_* galaxies in our sample when applying a CO threshold of 10 $M_\odot$pc^{-2}. $f_{\rm scale}$ also decreases from earlier- to later-type spiral galaxies, but the trend is not as strong as for M_*.

The dependence of $f_{\rm scale}$ on host-galaxy properties suggests the potential importance of the environment for regulating star formation (see also Paper I and Chevance et al. 2020). However, the evolution of star-forming regions is only visible when the spatial scale is close enough to the typical region separation length between molecular clouds and H II regions. Figure 15 shows the dependence of radial $f_{\rm scale}$ on the spatial scale as a function of M_*. Light- to dark-gray circles denote $f_{\rm scale}$ at different spatial scales of 300, 500, 1000, and 1500 pc, while $f_{\rm scale}$ at 150 pc resolution is indicated by red squares. At spatial scales $\leqslant$300 pc, there is a distinct difference in $f_{\rm scale}$ between galaxy populations, as parameterized by M_*. The differences between galaxies become considerably smaller at spatial scales of >300 pc due to the significant decrease in *CO-only* sight lines and increase in *Overlap* sight lines, indicating a critical resolution requirement to resolve the evolution of individual star-forming regions. The critical spatial scale of 300 pc is consistent with the characteristic separation length between independent clouds or star-forming regions reported by Chevance et al. (2020).

While there is a clear dependence on spatial scale, the derived $t_{\rm gas}$ at 150 pc resolution are in reasonable agreement within a factor of a few (2 to 3) in most radial bins with the cloud lifetime ($t_{\rm GMC}$), during which CO emission is visibly estimated by Chevance et al. (2020) for seven of our galaxies using the statistical method developed by Kruijssen et al. (2018). We present a direct comparison of the radial variation of our $t_{\rm gas}$ with $t_{\rm GMC}$ from Chevance et al. (2020) in Appendix D. The $t_{\rm gas}$ measured at 150 pc resolution also agrees well with the estimates of cloud (CO) visibility time based on counting the number of GMCs with and without H II regions (e.g., Kawamura et al. 2009).

Finally, there are several systematic differences in cloud properties and uncertainties to bear in mind when using Equation (3) to estimate the visibility time of molecular clouds traced by CO. First of all, more massive galaxies typically have larger midplane ISM pressures, which leads to higher molecular gas surface densities and thus larger GMC sizes traced by CO. On the other hand, in a high-pressure environment, H II regions might be smaller. Therefore, the number of CO and Hα sight lines may reflect not only the variation of cloud visibility time but also the intrinsic differences in GMC and H II region properties among galaxies. Moreover, our measurements of Hα sight lines (Section 3.1) are affected by internal extinction and non–H II powering mechanisms. In principle, the identification of H II sight lines could be refined by the use of optical IFS observations. Similarly, the fractions of CO sight lines depend on the applied surface-density threshold (Section 3.2). Though our filtering methods are verified by visual inspection of the filtered CO and Hα images and comparing with the H II regions identified in the PHANGS-MUSE images, the impact of the methodology remains a potential source of bias (see Appendix A). Finally, molecular clouds and H II regions may have not yet been fully resolved by our 150 pc resolution as discussed in Section 5.1. A handful of our galaxies have PHANGS-ALMA CO and PHANGS-MUSE Hα images with a resolution of $\sim$50 pc, comparable to the size of GMCs and H II regions (e.g., NGC 0628, NGC 2835, and NGC 5068). At such high resolution, the counting numbers of objects and sight lines should become almost identical and thus would provide a more robust estimate of cloud (CO) visibility time and even the actual lifetime of molecular clouds. In summary, in addition to cloud visibility time, the region sizes traced by CO and Hα emission, the ratio between the resolution and the region separation length, and the data-processing strategy may also contribute to the derived $f_{\rm scale}$.

5.6. Implication for the Kennicutt–Schmidt Relation

Many studies have shown that the Kennicutt–Schmidt relation between the surface densities of molecular gas and SFR is tight with an index $\sim$0.7–1.4 on kpc scales (e.g., Bigiel et al. 2008; Leroy et al. 2008, 2013; Schruba et al. 2011;

Momose et al. 2013). These findings resonate with our analysis, where the *Overlap* sight lines dominate the maps when the spatial scale is approximately or greater than 1 kpc; in other words, maps of molecular gas and star formation tracers become very similar.

The picture becomes more complex when the resolution increases. When the resolution is high enough to separate molecular clouds and star-forming regions, molecular gas and star formation surface densities become loosely correlated (e.g., Blanc et al. 2009; Onodera et al. 2010; Kreckel et al. 2018; Pessa et al. 2021) or even anticorrelated (e.g., Schruba et al. 2010) because the two components no longer coincide at all times. This spatial separation between different evolutionary stages of the star formation process is also evident in our sight-line maps at the resolution of 150 pc (Figures 2 and B1). The loosely (anti)correlated molecular gas and SFR tracers lead to an increasing scatter in the Kennicutt–Schmidt relation at small spatial scales, as a result of incomplete sampling of different evolutionary stages of the gas and star formation cycle (e.g., Schruba et al. 2010; Feldmann et al. 2011; Leroy et al. 2013; Kruijssen & Longmore 2014).

Our results at 150 pc resolution reveal an important dependence between host-galaxy properties and the relative distribution of molecular gas and star formation tracers on each other. Namely, how molecular gas and SFR tracers relate (or do not relate) to one another on the Kennicutt–Schmidt plane depends on the host-galaxy properties, such as M_* and Hubble type. However, any relation between the sight-line fractions and host-galaxy properties seen at 150 pc resolution is gradually diminished as resolution decreases and becomes unidentifiable when at resolutions coarser than ∼500 pc. Galactic structures add further complexity to the Kennicutt–Schmidt relation as the relation varies among galactic environments (Pan & Kuno 2017; Pessa et al. 2021; Querejeta et al. 2021). Because the contribution of the different environments varies as a function of galactic radius, the impact of environments could be transferred to the Kennicutt–Schmidt relation when averaging the environments.

Moreover, if the relative distributions of *CO-only* and *Hα-only* sight lines are complex at high resolution, we might be missing important $\tau_{\rm dep}$ variations (i.e., the slope and intercept of the Kennicutt–Schmidt relation) and change in cloud life cycle/time variations (i.e., scatter of the relation) when using the Kennicutt–Schmidt relation alone as a diagnostic of star formation process because the relation, by definition, only sees the *Overlap* regions.

6. Summary

The main goal of this study is to investigate how global galaxy properties affect the radial distribution of various stages in the star formation cycle using an unprecedented large sample of 49 star-forming main-sequence disk galaxies (Figure 1). We compare high-resolution (∼1″) observations of CO line emission and narrowband Hα maps of nearby galaxies selected from the PHANGS surveys (Section 2).

We adopt a simple and reproducible method developed in Paper I to quantify the relative spatial distributions of molecular gas and recent star formation (Section 3). The method has taken into account the contribution of diffuse ionized gas to the Hα emission and the metallicity dependence of CO-to-H_2 conversion factor when identifying star-forming regions and molecular clouds.

We classify each sight line (i.e., pixel) at each resolution according to the overlap between the tracers: *CO-only*, *Hα-only*, and *Overlap* (CO and Hα) (Figure 2). These three categories can be translated into the following star formation phases: *CO-only*—molecular gas currently not associated with star formation traced by Hα, *Overlap*—star-forming molecular clouds, and *Hα-only*—regions of young massive stars. We investigate whether the fractions of the different categories of sight lines vary with galaxy properties (stellar mass and Hubble type), galactocentric radius, and the presence of bars or GD spiral structure. We also measure the sight-line fractions at different resolutions ranging from 150 pc to 1.5 kpc. The best common resolution (150 pc) is sufficiently high to sample individual star-forming units and to separate such regions. A summary of the main results presented in this paper is as follows.

1. At our best-matching resolution of 150 pc for our sample, a median of 36% of detected sight lines in a galaxy are dominated by CO emission alone. The molecular gas surface densities of these *CO-only* regions are not necessarily low, ranging from our applied threshold ($10\ M_\odot\ {\rm pc}^{-2}$; see Section 3) to a few thousands $M_\odot\ {\rm pc}^{-2}$. This implies that there is a substantial fraction of molecular gas in galaxies that is currently not associated with young high-mass star formation traced by non-DIG optical tracers. Statistically, the second-most-common category is *Overlap* regions where both CO and Hα emission coincide, accounting for a median of 30% of the sight lines at 150 pc resolution. The *Overlap* sight lines show the least variation from galaxy to galaxy. The *Hα-only* sight lines are less common than the other two categories, with a median fraction of 20%, but also exhibit the largest galaxy-to-galaxy variations. The rank of the median sight-line fractions is consistent with Paper I, which used only eight galaxies (Section 4.1 and Figure 3).
2. At 150 pc resolution, we find strong correlations between the sight-line fractions (*CO-only* and *Hα-only*) and global galaxy properties. Such dependencies had already been hinted at in Paper I, which analyzed a small subset of our sample; in this work, we quantify the dependencies. Specifically, the fraction of *CO-only* sight lines within the fiducial FoV increases gradually with increasing M_* and also increases gradually from later- to earlier-type spiral galaxies. The opposite trend is observed for *Hα-only* sight lines. The fraction of *Overlap* regions is insensitive to M_* but increases toward later types. These trends observed for the global sight-line fractions are almost preserved radially from the center out to $0.6\,R_{25}$ (corresponding to ∼6 kpc). Our results at 150 pc resolution suggest that the relationship between molecular gas and SFR tracers in the Kennicutt–Schmidt plane depends on host-galaxy properties (Sections 4.1 and 5.6, Figures 4 and 5).
3. In addition to M_* and Hubble type, we also classify galaxies according to the presence of a stellar bar and/or GD spiral arms. Galaxies without these structures, galaxies with a stellar bar only, and galaxies with both a bar and GD spiral arms exhibit broadly similar sight-line fractions. Galaxies with GD spiral arms but no stellar bar, however, show a distinct signature of higher *CO-only* and *Overlap* fractions and lower *Hα-only* fraction than

the other populations. Moreover, galaxies with a bar show a stronger (weaker) radial dependence of *CO-only* (*Overlap*) sight lines than galaxies without a bar. These results suggest that galactic dynamics further contributes to organizing the spatial distribution of CO and Hα emission separately within galaxies (Sections 4.2 and 5.2, Figures 6 and 7).

4. Comparing the fractions of pixels (our "default" approach) with the fractions of flux shows that *Overlap* regions tend to have higher CO and Hα intensities compared to regions that emit CO or Hα alone. Yet the flux traced by *CO-only* and *Hα-only* regions cannot be ignored because they still contribute a median of 33% (mean: 37%) and 14% (mean: 25%) of the galaxy's total CO and Hα flux, respectively. The result is consistent with the finding of Paper I. (Section 4.3, Figures 8 and 9).
5. The sight-line fractions show a strong dependence on the spatial scale (resolution), confirming the finding of Paper I. Specifically, *CO-only* and *Hα-only* regions rapidly vanish as spatial scale increases. Therefore, any relation between the sight-line fractions and galaxy properties (M_* and Hubble type) are only evident when the resolution is $\ll$500 pc (Section 4.4, Figures 10 and 11).
6. We find no correlation between the global sight-line fractions with specific SFR and the offset from the star-forming main sequence (ΔMS). Nonetheless, galaxies with the highest or the lowest ΔMS in our sample both show significant molecular gas reservoirs that do not appear to be associated with star formation. However, the spatial distribution of their *CO-only* sight lines is different, pointing to different underlying causes for their high *CO-only* fractions (Section 5.3 and Figure 12).
7. *Hα-only* regions tend to be found in atomic-gas-dominated regions in low-M_* systems. It is very likely that lower-mass molecular clouds exist in these regions, but their Σ_{H_2} drops below our applied threshold, adding further evidence for prominent galaxy-to-galaxy variation in molecular cloud properties, in line with previous studies (e.g., Hughes et al. 2013; Sun et al. 2020b; Rosolowsky et al. 2021) (Section 5.4 and Figure 13).
8. We estimate the duration for which the molecular cloud traced by CO emission is visible following the statistical approach in Paper I. There is a ranking of cloud visibility time with M_* where molecular clouds in high-M_* galaxies tend to have a longer visibility time than clouds in low-M_* over the radial range probed. The trend is related to the fact that molecular clouds in high-M_* galaxies tend to have higher molecular-mass surface densities. However, the differences between galaxies become considerably smaller when the spatial scale is larger than 500 pc due to a significant decrease in *CO-only* sight line and increase in *Overlap* sight line, indicating a critical resolution that is required to resolve the evolution of individual star-forming regions. We also note several systematic differences in cloud properties and uncertainties to bear in mind when using Equation (3) to estimate the visibility time of molecular clouds (Section 5.5 and Figures 14 and 15).

The methodology presented in this paper offers a simple, physically motivated, and reproducible approach for quantifying the relative distribution of molecular gas traced by CO emission and H II regions traced by Hα emission. Several caveats related to the use of this approach should be kept in mind, including the choices of CO-to-H_2 conversion factor, CO(2–1)-to-CO(1–0) brightness temperature ratio, unsharp masking parameters, and Hα and CO(Σ_{H_2}) thresholds. These factors are discussed in detail in Appendix A. Although our results remain robust when accounting for the impact of these factors, care should be taken when interpreting the results based on our sight-line method. Moreover, because our main analysis focuses mostly on the location (rather than the amount) of massive star formation, we consider internal extinction as a secondary issue. Nonetheless, there is room for improvement with the use of optical IFS data, which allow for simultaneous correction for internal extinction and tools for distinguishing Hα emission emitted by various powering sources. A straightforward next step would be to test our results with a large, diverse, deep ($\log L_{H\alpha} \approx 36$ erg s^{-1}), and high-resolution ($\leqslant$100 pc) IFS sample. Other follow-up studies (utilizing a large IFS sample) include the detailed investigation of the nature of *CO-only* and *Hα-only* regions, the absolute timescale of each star formation phase, and the dependence of these properties on global galaxy properties and galactic dynamics.

We thank the anonymous referee for constructive comments that improved the paper. This work was carried out as part of the PHANGS collaboration.

H.A.P. acknowledges funding from the European Research Council (ERC) under the European Union's Horizon 2020 research and innovation program (grant agreement No. 694343), and the Ministry of Science and Technology (MOST) of Taiwan under grant 110-2112-M-032-020-MY3.

E.S., P.L., D.L., R.Mc.E., T.S., F.S., and T.G.W. acknowledge funding from the European Research Council (ERC) under the European Union's Horizon 2020 research and innovation program (grant agreement No. 694343).

A.H. was supported by the Programme National Cosmology et Galaxies (PNCG) of CNRS/INSU with INP and IN2P3, co-funded by CEA and CNES, and by the Programme National "Physique et Chimie du Milieu Interstellaire" (PCMI) of CNRS/INSU with INC/INP co-funded by CEA and CNES.

The work of A.K.L., J.S., and D.U. is partially supported by the National Science Foundation under grants No. 1615105, 1615109, and 1653300.

A.B. and F.B. acknowledge funding from the European Research Council (ERC) under the European Union's Horizon 2020 research and innovation program (grant agreement No. 726384/Empire).

M.C. gratefully acknowledges funding from the Deutsche Forschungsgemeinschaft (DFG) through an Emmy Noether Research Group, grant No. KR4801/1-1 and the DFG Sachbeihilfe, grant No. KR4801/2-1, and from the European Research Council (ERC) under the European Union's Horizon 2020 research and innovation program via the ERC Starting Grant MUSTANG (grant agreement No. 714907).

E.C. acknowledges support from ANID project Basal AFB-170002.

C.E. acknowledges funding from the Deutsche Forschungsgemeinschaft (DFG) Sachbeihilfe, grant No. BI1546/3-1.

C.M.F. is supported by the National Science Foundation under award No. 1903946 and acknowledges funding from the European Research Council (ERC) under the European

Union's Horizon 2020 research and innovation program (grant agreement No. 694343).

S.C.O.G. and R.S.K. acknowledge financial support from the German Research Foundation (DFG) via the collaborative research center (SFB 881, Project-ID 138713538) "The Milky Way System" (subprojects A1, B1, B2, and B8). They also acknowledge funding from the Heidelberg Cluster of Excellence "STRUCTURES" in the framework of Germany's Excellence Strategy (grant EXC-2181/1, Project-ID 390900948) and from the European Research Council via the ERC Synergy Grant "ECOGAL" (grant 855130).

J.M.D.K. gratefully acknowledges funding from the Deutsche Forschungsgemeinschaft (DFG) in the form of an Emmy Noether Research Group (grant No. KR4801/1-1) and the DFG Sachbeihilfe (grant No. KR4801/2-1), and from the European Research Council (ERC) under the European Union's Horizon 2020 research and innovation program via the ERC Starting Grant MUSTANG (grant agreement No. 714907).

J.P. acknowledges support from the Programme National "Physique et Chimie du Milieu Interstellaire" (PCMI) of CNRS/INSU with INC/INP co-funded by CEA and CNES.

M.Q. acknowledges support from the research project PID2019-106027GA-C44 from the Spanish Ministerio de Ciencia e Innovación.

E.R. acknowledges the support of the Natural Sciences and Engineering Research Council of Canada (NSERC), funding reference number RGPIN-2017-03987.

A.U. acknowledges support from the Spanish funding grants PGC2018-094671-B-I00 (MCIU/AEI/FEDER) and PID2019-108765GB-I00 (MICINN).

This paper makes use of the following ALMA data: ADS/JAO.ALMA#2012.1.00650.S, ADS/JAO.ALMA2013.1.01161.S, ADS/JAO.ALMA#2015.1.00925.S, ADS/JAO.ALMA#2015.1.00956.S, ADS/JAO.ALMA#2017.1.00392.S, ADS/JAO.ALMA#2017.1.00886.L, ADS/JAO.ALMA#2018.1.01651.S. ALMA is a partnership of ESO (representing its member states), NSF (USA) and NINS (Japan), together with NRC (Canada), MOST and ASIAA (Taiwan), and KASI (Republic of Korea), in cooperation with the Republic of Chile. The Joint ALMA Observatory is operated by ESO, AUI/NRAO and NAOJ.

This paper includes data gathered with the 2.5 m du Pont located at Las Campanas Observatory, Chile, and data based on observations carried out at the MPG 2.2 m telescope on La Silla, Chile.

Appendix A
Impact of Methodology

Here we discuss the potential impact of methodology on our results, including the choice of CO-to-H_2 conversion factor, CO(2–1)-to-CO(1–0) ratio, unsharp masking parameters, and Hα and CO thresholds. Figure A1 summarizes the sight-line fractions for each individual galaxy based on different methodologies. Bar graphs with darker colors make use of the default unsharp masking parameters, and adopted Σ_{H_2} threshold and α_{CO} described in Sections 2 and 3, while bar graphs with lighter colors demonstrate the impact of these three assumptions.

A.1. CO-to-H_2 Conversion Factor

We test whether our results are sensitive to the employed α_{CO} conversion factor by comparing the sight-line fractions based on the metallicity- and radius-dependent α_{CO} (default in this work; see Section 2.1) and the frequently used, constant Galactic α_{CO} of 4.35 $M_\odot$ pc^{-1} (K km s^{-1})$^{-1}$ (Bolatto et al. 2013). The metallicity- and radius-dependent α_{CO} values tend to be lower than the Galactic value at small galactocentric radii and higher than the Galactic value at large radii. Therefore, for a given H_2 surface-density threshold, applying the Galactic α_{CO} often increases the number of CO sight lines (*CO-only* and *Overlap*) at small galactocentric radii and decreases the number of CO sight lines at large galactocentric radii. The resulting impact on the sight-line fractions thus depends on the radial distribution of CO and Hα emission. The different α_{CO} prescriptions translate into a typical variation of the sight-line fractions of $\pm$10% (mostly within 5%). The median and mean differences are within $\pm$1% for all types of sight lines. We again repeat our analysis of the dependence on the sight-line fraction for M_*, Hubble type, and spatial scale, using the sight-line fractions estimated from the Galactic α_{CO}. We conclude that our results are robust against the choice of α_{CO}. The sight-line fractions based on the Galactic α_{CO} are presented in column Q in Figure A1.

A.2. CO (2–1)-to-CO(1–0) Ratio

In this work, we adopt a single ^{12}CO(2–1)-to-^{12}CO(1–0) brightness temperature ratio of $R_{21} = 0.65$ for all our sample galaxies. We do not account for galaxy-to-galaxy variations in R_{21}. Recent studies of nearby galaxies show that the R_{21} for individual galaxies is around 0.5 to 0.7, and the typical scatter is $\sim$0.1 dex within individual galaxies (e.g., den Brok et al. 2021; Leroy et al. 2021b; Yajima et al. 2021). Physically, R_{21} may increase with SFR and gas density because the higher-J transition becomes brighter when gas is warm and/or dense (e.g., Sakamoto et al. 1994, 1997; den Brok et al. 2021; Leroy et al. 2021b; Yajima et al. 2021). In other words, assuming a single R_{21} may result in the overestimation of Σ_{H_2} in *Overlap* regions (given that the CO and Hα emission are likely to coexist in high-SFR and/or high-density regions). Nonetheless, we do not expect the Σ_{H_2} in the *Overlap* regions to drop below the CO threshold (10 $M_\odot$ pc^{-2}) even when accounting for the varying R_{21}. Moreover, as shown in Figure 8(a)(top), the sight-line ratio between the *CO-only* and *CO-overlap* regions is $\sim$1:1, while their flux ratio is $\sim$1:2, suggesting that the *CO-overlap* regions are on average two times brighter than the *CO-only* regions. On the other hand, the typical $\sim$0.1 dex scatter of R_{21} corresponds to a $\sim$25% difference in flux. Therefore, the difference between the sight-line ratio and the flux ratio is unlikely to disappear even if the R_{21} variation were taken into account. Taken together, we conclude that our results should remain valid for the typical scatter in R_{21} (note again that our analysis focuses on the location, rather than the amount, of molecular clouds and star formation).

A.3. Unsharp Masking Parameters

As described in Section 3, the adopted unsharp masking parameters are optimized to reproduce the H II regions detected in the PHANGS-MUSE Hα images (Santoro et al. 2021). We have also identified two additional sets of parameters that also reasonably well reproduce the H II regions identified in PHANGS-MUSE. The second-best parameters (UM_{2nd_best}) have a 200 pc kernel for Step 1 in Section 3.1, a scaling factor of 0.33

Figure A1. Bar graphs summarizing the impact of methodology and assumptions on *CO-only* (blue), *Hα-only* (red), and *Overlap* (yellow) sight lines for individual galaxies at 150 pc resolution. Bar graphs with darker colors make use of the default unsharp masking parameters, adopted H_2 threshold, and α_{CO} conversion factor, while bar graphs with lighter colors demonstrate the impact of these three assumptions. Here we show (A–G) the number of sight lines for our FoV with H_2 threshold of 7–13 $M_\odot$ pc^{-2}, respectively; (H) the number of sight lines for a disk with a default H_2 threshold of 10 $M_\odot$ pc^{-2}; (I) and (J) relative contribution of the number of CO sight lines (*CO-only* and *Overlap*) for our FoV and disk; (K) and (L) relative contribution of the CO flux of CO sight lines (*CO-only* and *Overlap*) for our FoV and disk; (M) and (N) relative contribution of the number of Hα sight lines (*Hα-only* and *Overlap*) for our FoV and disk; (O) and (P) relative contribution of the Hα flux of Hα sight lines (*Hα-only* and *Overlap*) for our FoV and disk; (Q) three number of sight lines for our FoV with Galactic α_{CO}. (R) and (S) the number of sight lines for our FoV with unsharp masking parameters UM_{2nd_best} and $UM_{Paper\ I}$, respectively. The black dotted lines are used to guide the eye. Sight-line fractions in column D are the default fractions used for the main analysis in this work at 150 pc resolution.

for Step 2, and a kernel size of 400 pc for Step 3. The third best (UM_{paperI}) is the set of parameters used in Paper I: 300 pc for Step 1, 0.33 for Step 2, and 750 pc for Step 3.

We test how sight-line fractions relate to the DIG removal process by repeating the sight-line classification using H II region maps created with the other two sets of unsharp masking parameters. Overall, we find that the derived sight-line fractions are similar among the three sets of parameters. The median and mean differences in any sight-line fraction for any two sets of parameters are always <5%. For reference, the sight-line fractions estimated based on different unsharp masking parameters are presented in Figure A1, column D (this work), column R (UM_{2nd_best}), and column S (UM_{paperI}). We also repeat all analyses using the sight-line fractions estimated based on UM_{2nd_best} and UM_{paperI}. Our results are robust against the choice of different unsharp masking parameters, as far as they can reasonably reproduce the H II region properties identified in the VLT/MUSE IFU data. A detailed description of how we verified the narrowband H II regions using PHANGS-MUSE spectroscopic information will be presented in a forthcoming paper (H.-A. Pan et al. 2022, in preparation).

A.4. Hα Threshold

For a point source at the native resolution of our Hα data, the effective sensitivity limits in terms of the Hα surface-brightness threshold applied to the fiducial maps correspond to H II region luminosities ($\log(L_{\mathrm{H\,II\ region}}^{\mathrm{sensitivity}})$) between 36.7 and 38.4 erg s^{-1}. Here we carried out two tests to examine the impact of the varying Hα threshold (which originates from the nonuniform Hα sensitivity among the sample) on the results.

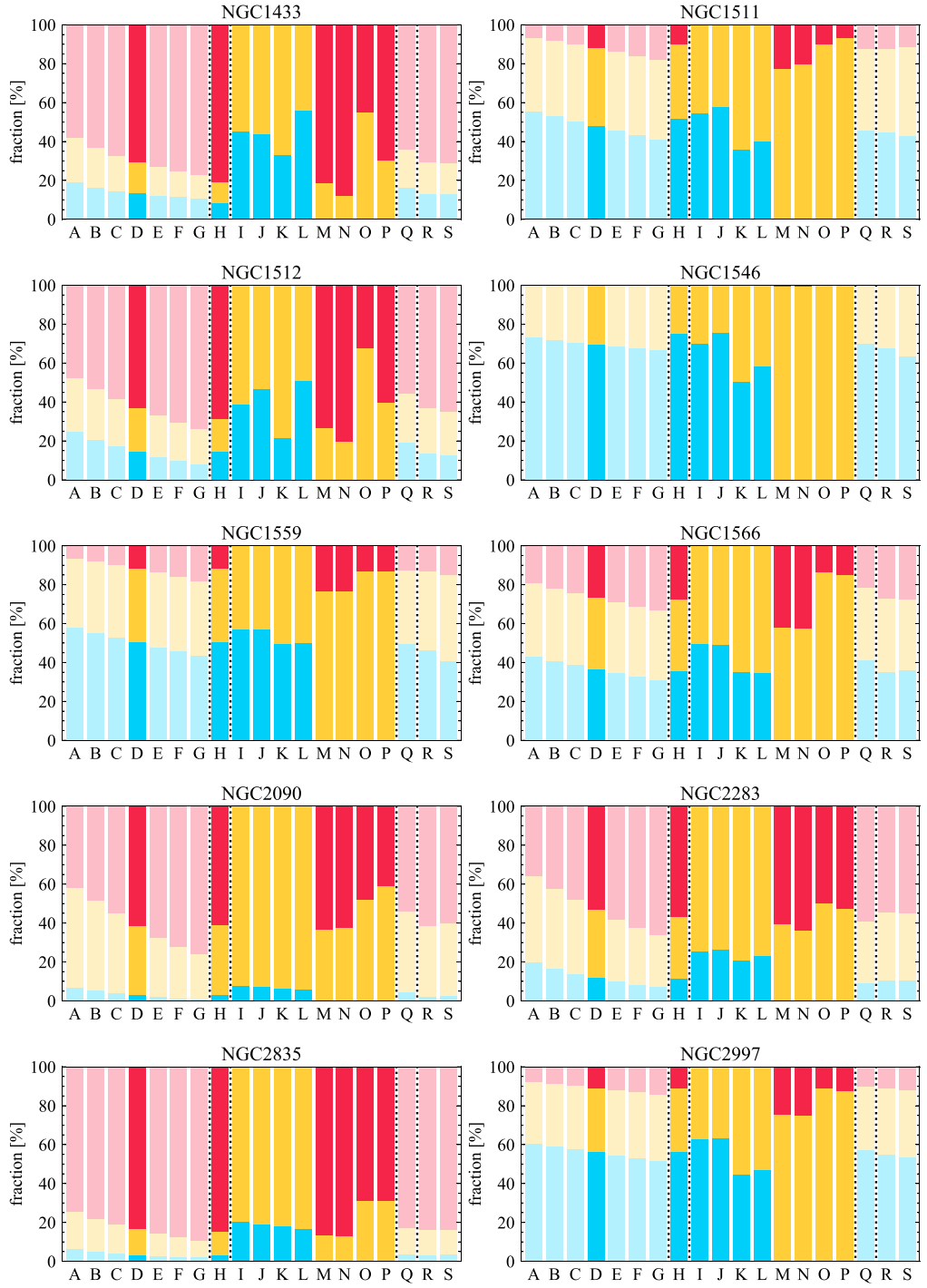

Figure A1. (Continued.)

In the first test, we compare the sight-line fractions estimated in the PHANGS-MUSE Hα images at 150 pc resolution to those measured in the default narrowband images at the same resolution. The PHANGS-MUSE observations are sensitive enough to probe down to H II regions with $\log(L) \approx 36$ erg s^{-1}, about an order of magnitude deeper than the narrowband images. We measure the sight-line fractions for the 15 galaxies that have both observations (hereafter overlapping sample). The MUSE images are treated using the same method as that for the narrowband data for the removal of DIG (see Section 3.1). Namely, the only difference between the two images is the increased sensitivity of the MUSE data.

As an example, Figure A2 shows the sight-line maps for galaxy NGC 0628 based on the narrowband (left) and MUSE (right) images. It can be seen directly that the number of *Hα-only* sight lines increases in the MUSE map as a result of its higher sensitivity. This is accompanied by a decrease in *CO-only* regions. A direct comparison is provided in Figure A3. While most galaxies show differences within a factor of 2, the difference can be up to a factor of 2.5 or even more for those galaxies with the

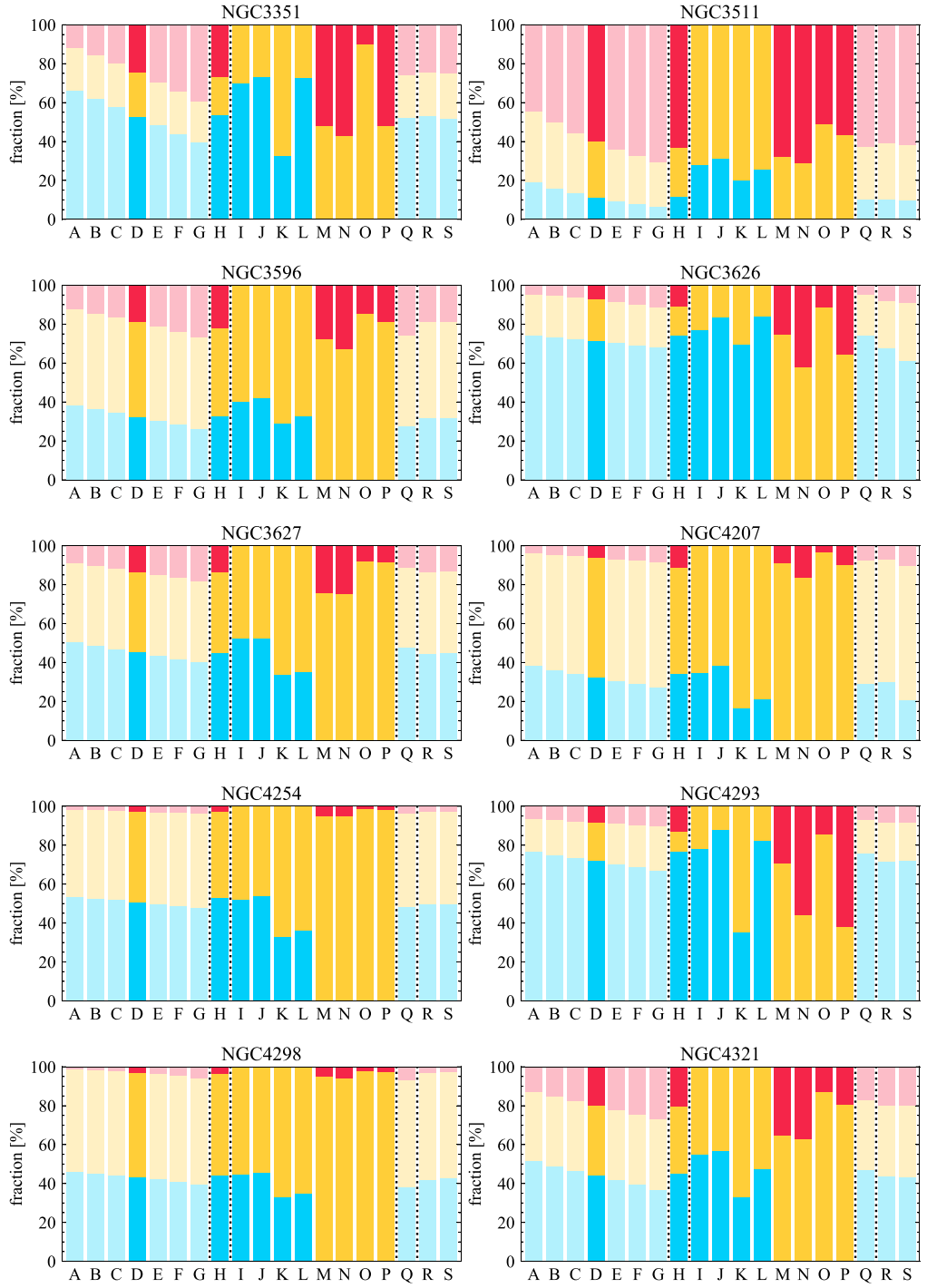

Figure A1. (Continued.)

highest $\log(L_{\mathrm{H\,II\,region}}^{\mathrm{sensitivity}})$ (i.e., the shallowest narrowband observation). The *Overlap* regions show the least difference between narrowband and MUSE. This is because the fluxes of the Hα emission are higher in *Overlap* regions compared to *Hα-only* regions (Section 4.3), so the *Overlap* fraction is less affected by sensitivity.

It is worth noting that the true discrepancy between the MUSE and narrowband sight-line fractions is likely smaller than what is obtained here. The low-Hα-luminosity regions (on the order of $L_{\mathrm{H}\alpha} \approx 10^{36\text{–}37}$ erg s^{-1}) are the main source of the discrepancy between the MUSE and narrowband sight-line fractions as they are not present in the narrowband observations due to the limited sensitivity. Previous studies on the nature of Hα-emitting sources in nearby galaxies show that regions ionized by non–H II sources (e.g., supernova remnants and planetary nebula) tend to have lower Hα luminosity compared to regions powered by H II regions (e.g., Belfiore et al. 2016; Hsieh et al. 2017; Pan et al. 2018). The same characteristic is observed in our MUSE data (e.g., Santoro et al. 2021; Scheuermann et al. 2022), suggesting that a certain fraction of regions missed by the narrowband observations are not H II regions.[35] Therefore, the discrepancy

[35] About ~30% based on the spectroscopic analysis by Santoro et al. (2021).

Figure A1. (Continued.)

between the MUSE and narrowband sight-line fractions reported here is an upper limit.[36]

Further, we find no correlation between the sight-line fractions and global galaxy properties (M_* and Hubble type), no matter which Hα image is used, presumably due to the low number of galaxies available in the overlapping sample. Therefore, we carried out a second test to verify whether the trend between the sight-line fractions and global galaxy properties (Section 4.1.1) still holds when the narrowband $\log(L_{\rm H\,II\,region}^{\rm sensitivity})$ is taken into account.

In the second test, we examine the relation between the sight-line fractions and global galaxy properties at 150 pc resolution using only galaxies with relatively high narrowband sensitivity (i.e., low $\log(L_{\rm H\,II\,region}^{\rm sensitivity})$). Specifically, we replot Figure 4 using only galaxies with $\log(L_{\rm H\,II\,region}^{\rm sensitivity}) < 37.5\,{\rm erg\,s^{-1}}$. Thirty-five

[36] To be in line with the analysis of narrowband data, for this comparison we did not apply a spectroscopic classification (e.g., like a Baldwin–Phillips–Terlevich (BPT) diagram, Baldwin et al. 1981) to the regions identified in the MUSE Hα map, so the non–H II regions remain in our DIG-removed MUSE maps. Such a spectroscopic classification is not possible for our narrowband data.

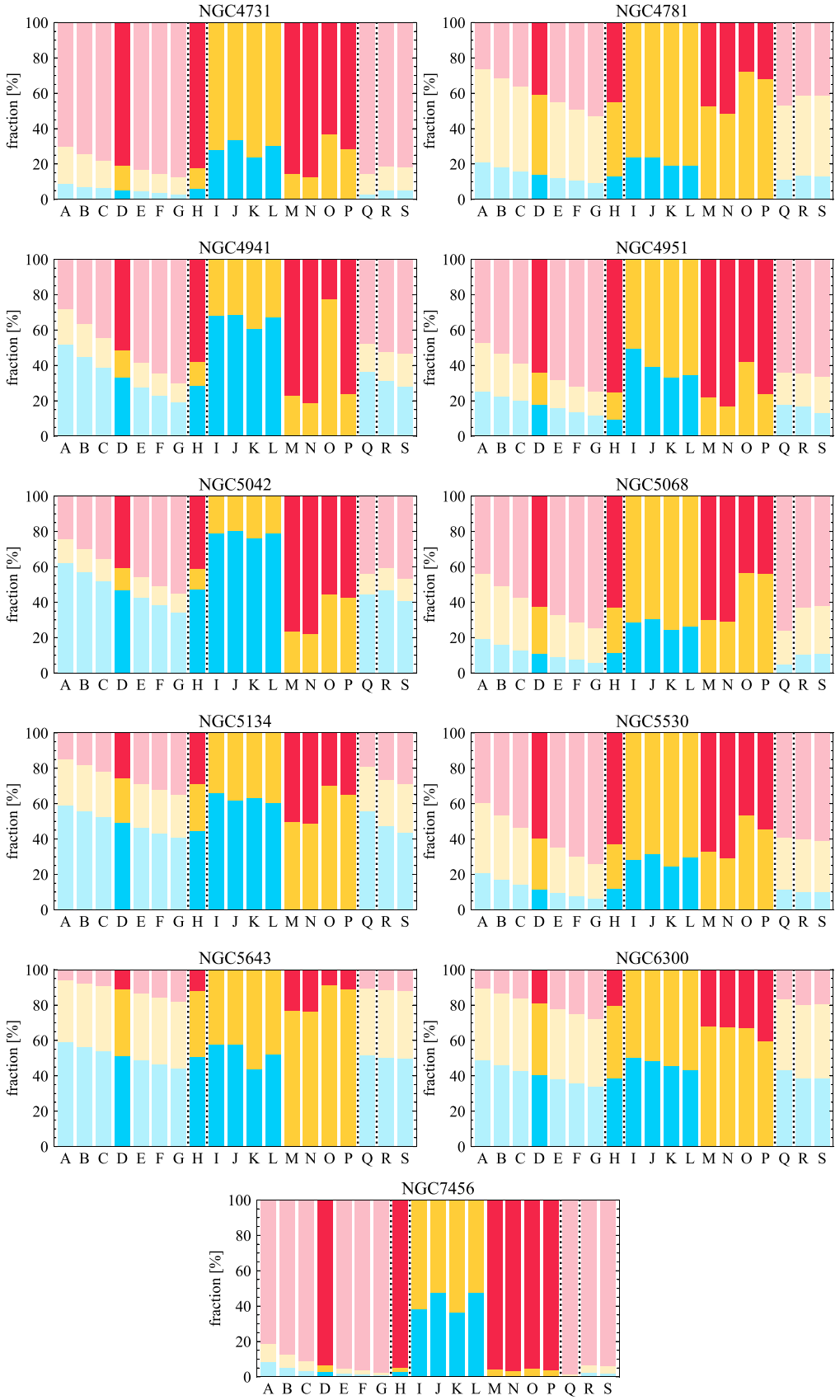

Figure A1. (Continued.)

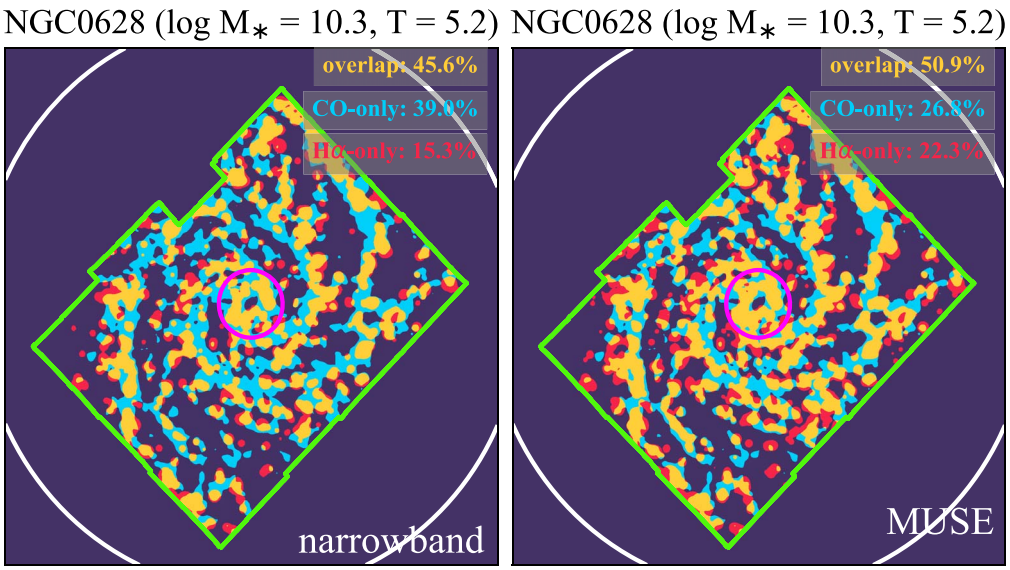

Figure A2. Comparison of the sight-line maps of NGC 0628 at 150 pc resolution produced based on narrowband (left) and MUSE IFS (right) Hα images. The symbols are the same as in Figure 2. The sight-line fractions based on both narrowband and MUSE observations are measured using the regions enclosed within the green box (MUSE FoV). Note that the MUSE FoV is smaller than that of the narrowband, so the narrowband sight-line fractions measured in Section A.4 are not necessarily the same as the fractions listed in Table B1.

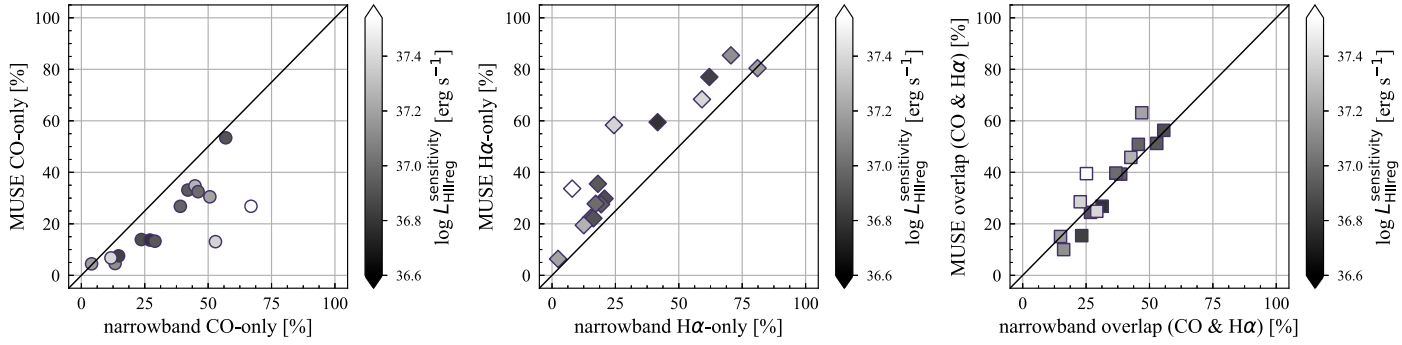

Figure A3. Comparison between the sight-line fractions at 150 pc resolution determined from the narrowband (x-axis) and MUSE (y-axis) observations, color-coded by $\log(L_{\rm H\,II\,region}^{\rm sensitivity})$. The solid line marks the one-to-one relation.

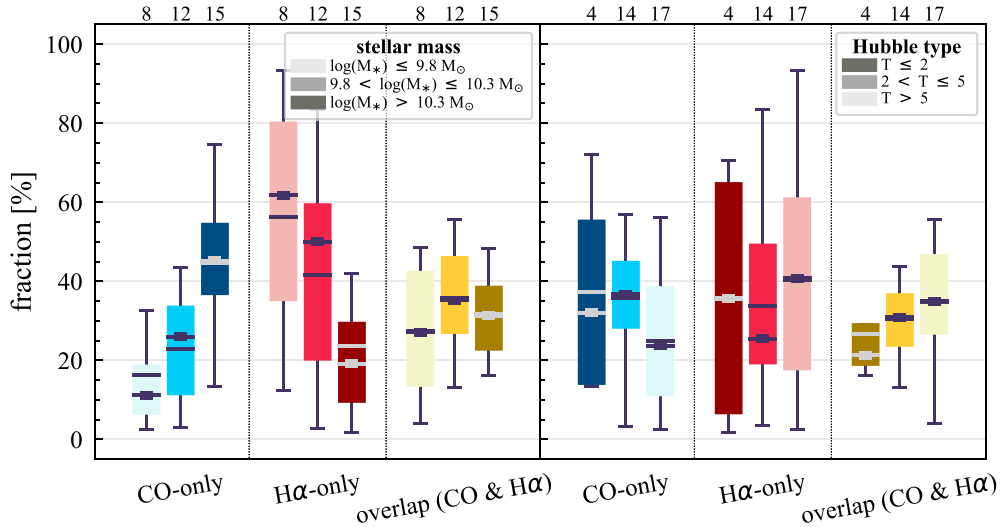

Figure A4. Variations of the global sight-line fractions at 150 pc resolution as a function of M_* (left) and Hubble type (right). The figure is analogous to Figure 4, but only the 35 galaxies with $\log(L_{\rm H\,II\,region}^{\rm sensitivity}) < 37.5$ erg s^{-1} are used.

galaxies satisfy this criterion; the result is shown in Figure A4. We find a good agreement between Figure 4 (full sample) and Figure A4 for M_* (left panel), although the median fractions can differ by a factor of a few between the two samples. For Hubble type, the trends with the *CO-only* and *Hα-only* fractions are no longer obvious when only using galaxies with relatively high narrowband sensitivity. This is partially (or perhaps even completely) due to the low-number statistics in the lowest-T bin as earlier-type galaxies in our sample tend to have less-sensitive Hα images. Despite that, the median *CO-only* and *Hα-only* fractions of the other two T-type bins and the *Overlap* fractions agree well with those derived using the full sample.

In summary, these two tests demonstrate that the Hα threshold is an important factor in the sight-line analysis. Our results remain qualitatively robust once the Hα threshold is accounted for, but further confirmation with high sensitivity and a large sample is required in the future.

A.5. CO (Σ_{H_2}) Threshold

We clip the CO images at our best-matching resolution of 150 pc using a surface-density threshold of 10 $M_\odot$ pc^{-2}. We test the effect of this threshold by varying the threshold from 7 to 13 $M_\odot$ pc^{-2}, $\sim-30\%$ to $+30\%$, with respect to the fiducial threshold. The sight-line fractions for a threshold of 7–13 $M_\odot$ pc^{-2} with an interval of 1 $M_\odot$ pc^{-2} are presented in Figure A1 columns A–G, respectively (column D is the default result of this work).

As somewhat expected, the fractions of the *CO-only* sight lines gradually decrease with increasing threshold in all galaxies, while the *Hα-only* sight lines gradually increase. The fractions of the *CO-only* sight lines show a decrease within a factor of $\sim$3 (with a few exceptions) when the threshold varies from -30% to $+30\%$ with respect to the fiducial threshold. An opposite trend is observed for the *Hα-only* sight lines, but the magnitude of the change is comparable to that of the *CO-only* sight lines. There is no uniform trend between the CO threshold and the fraction of *Overlap* sight lines; both increasing and decreasing trends are seen in our galaxies. Nonetheless, the typical magnitude of the change is smaller than that for the *CO-only* sight lines, not larger than a factor of 2. This is because the flux of CO in the *Overlap* regions tends to be higher than that in the *CO-only* regions (and presumably much higher than the applied threshold); therefore, they are less sensitive to the choice of the surface-density threshold. Overall, we find that the dependence of sight-line fractions on the applied threshold is rather uniform across the sample. For this reason, our results remain qualitatively the same when the CO threshold varies by $\pm30\%$.

Appendix B
Sight-line Maps and Fractions for Individual Galaxies at Different Spatial Scales

This appendix presents an atlas of the sight-line distributions in our 49 galaxies. Figure B1 presents galaxy maps showing *CO-only* (blue), *Hα-only* (red), and *overlapping* CO and Hα emission (yellow) at spatial resolutions of 150, 300, 500, 1000, and 1500 pc. The sight-line fractions measured within $R < 0.6R_{25}$ are listed in Table B1.

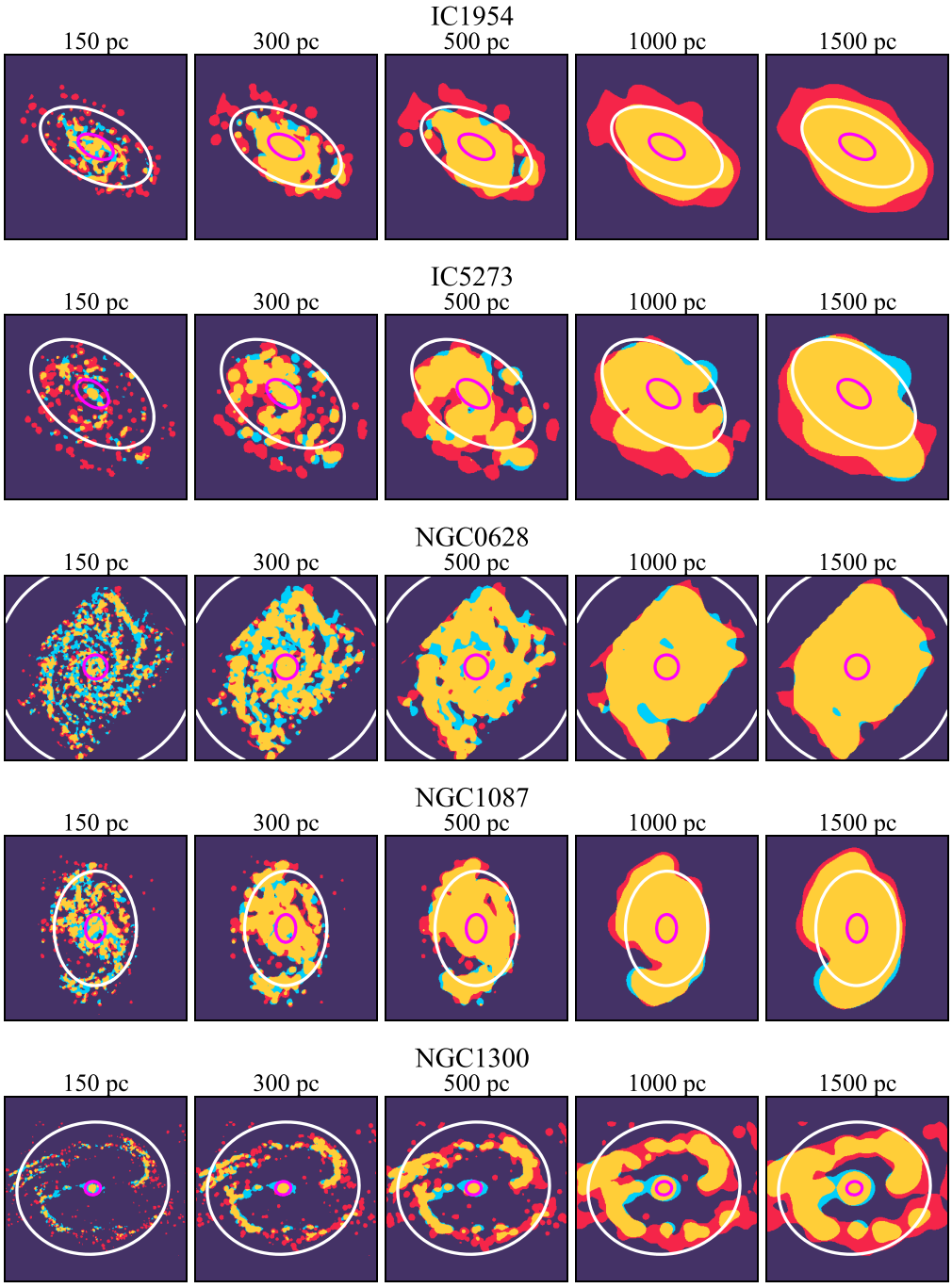

Figure B1. Galaxy maps showing regions with *CO-only* (blue), *Hα-only* (red), and overlapping CO and Hα emission (yellow) at 150, 300, 500, 1000, and 1500 pc resolutions. The inner ellipses (magenta) mark the central region, defined as the central 2 kpc in diameter. The outer ellipses (white) indicate the 0.6 R_{25} regions where we measure the global sight-line fractions.

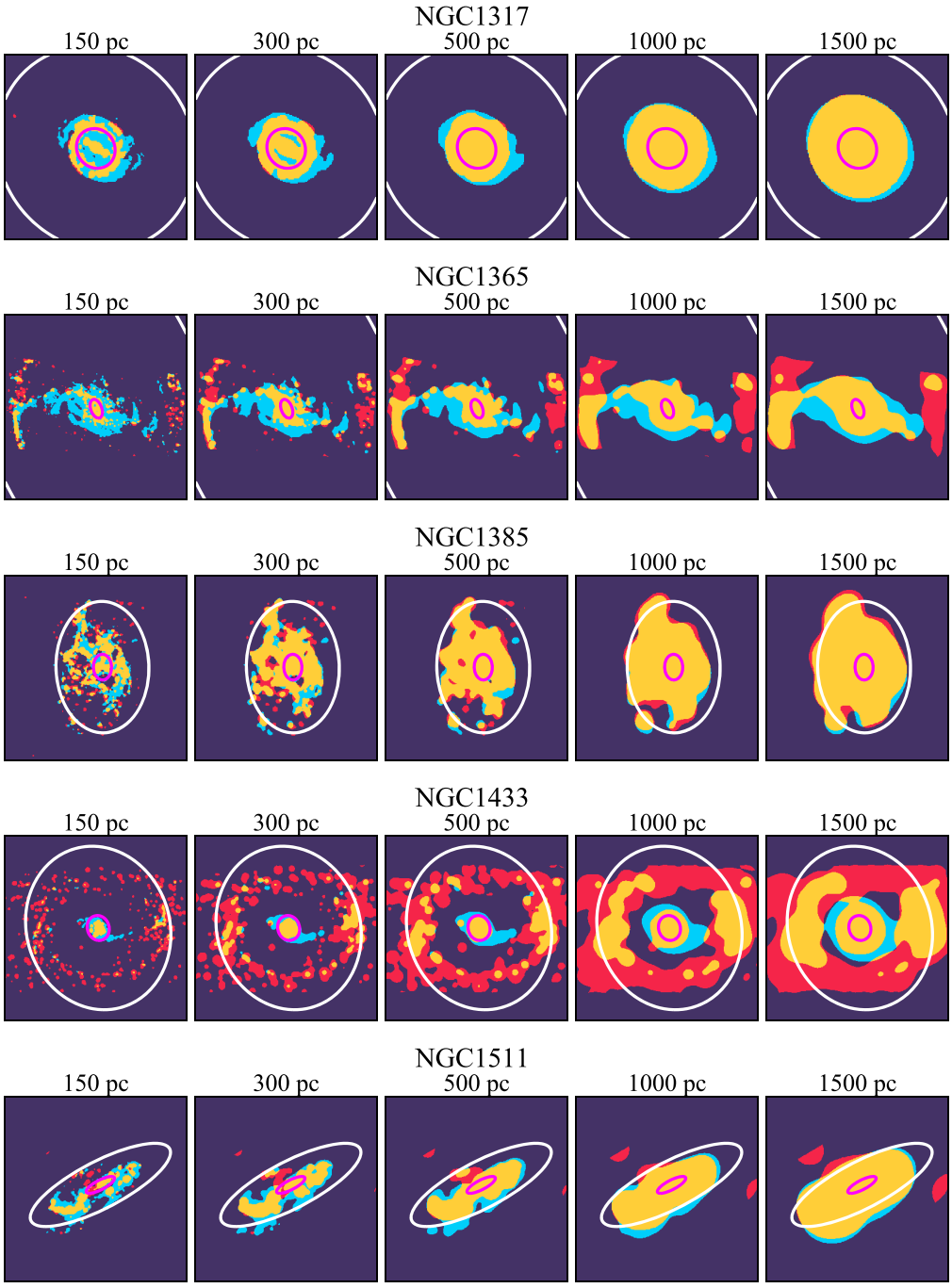

Figure B1. (Continued.)

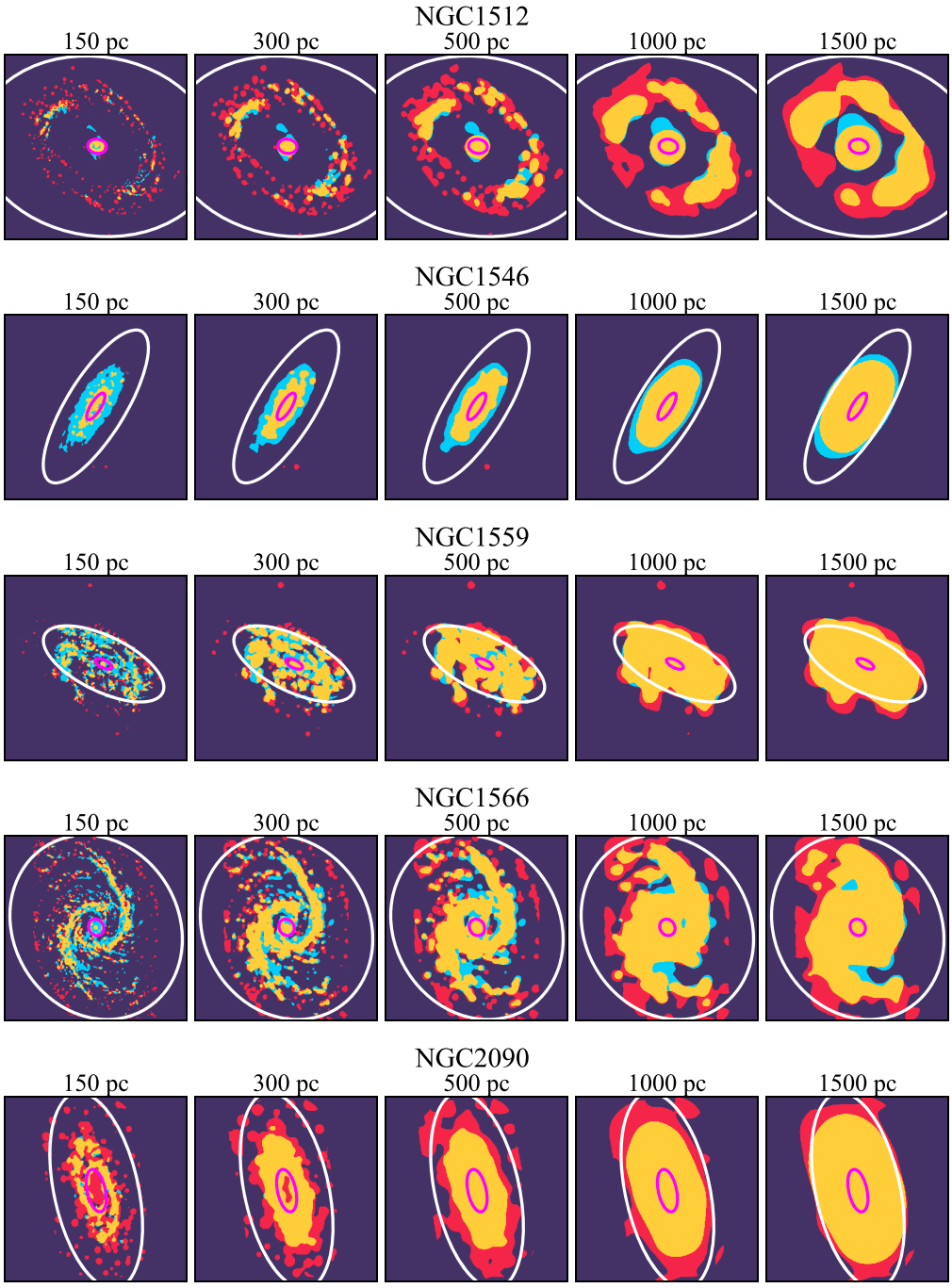

Figure B1. (Continued.)

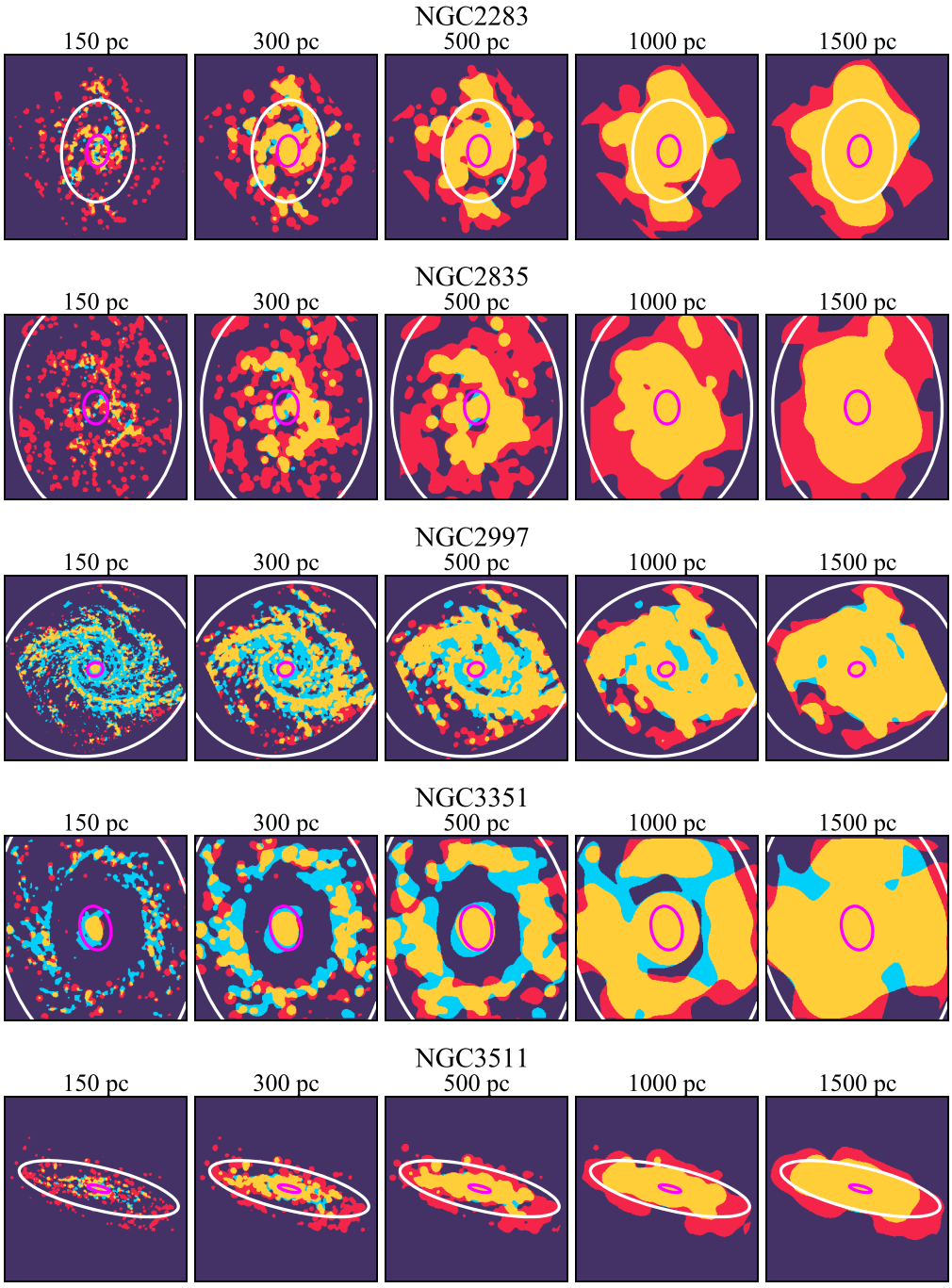

Figure B1. (Continued.)

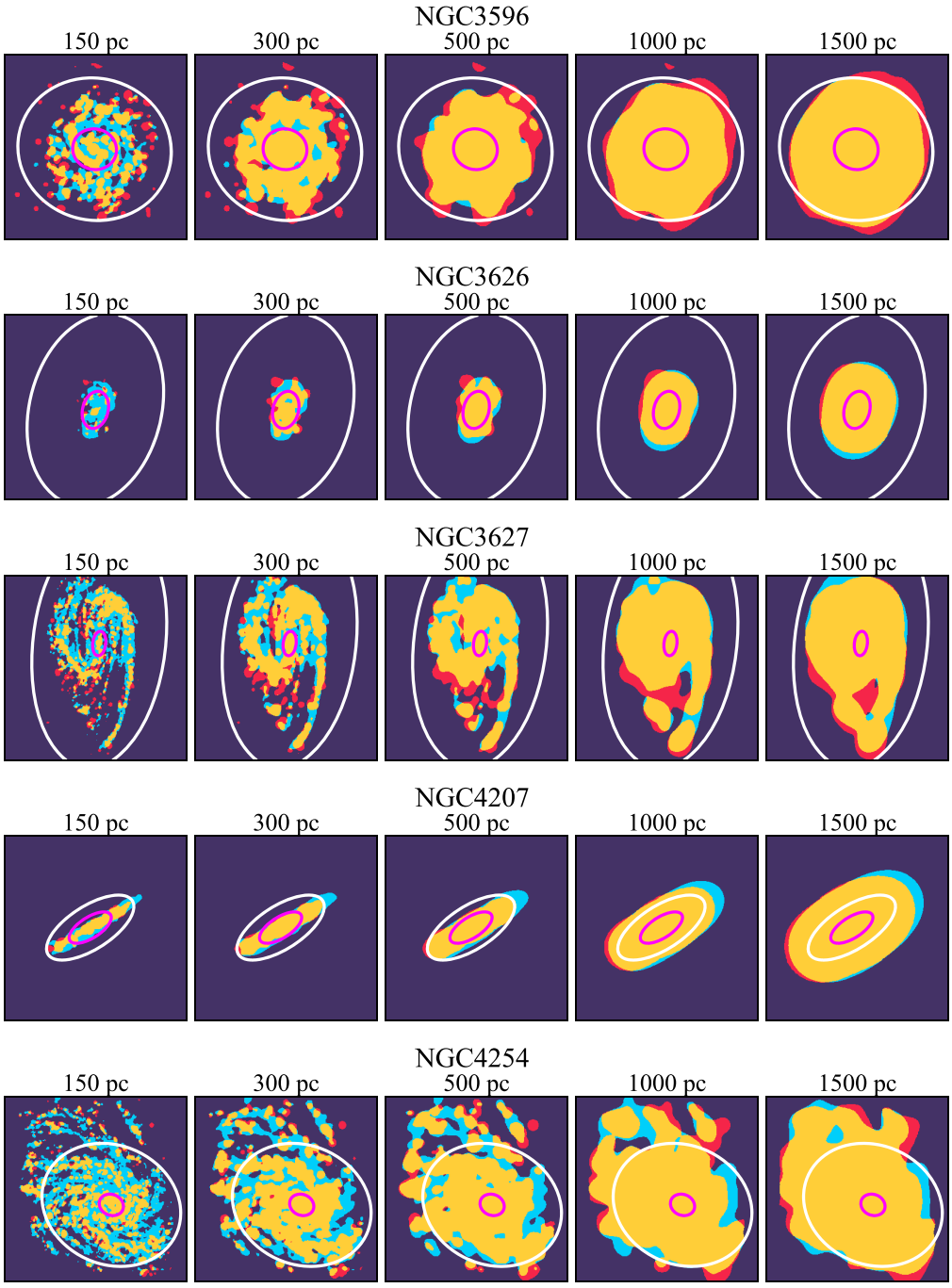

Figure B1. (Continued.)

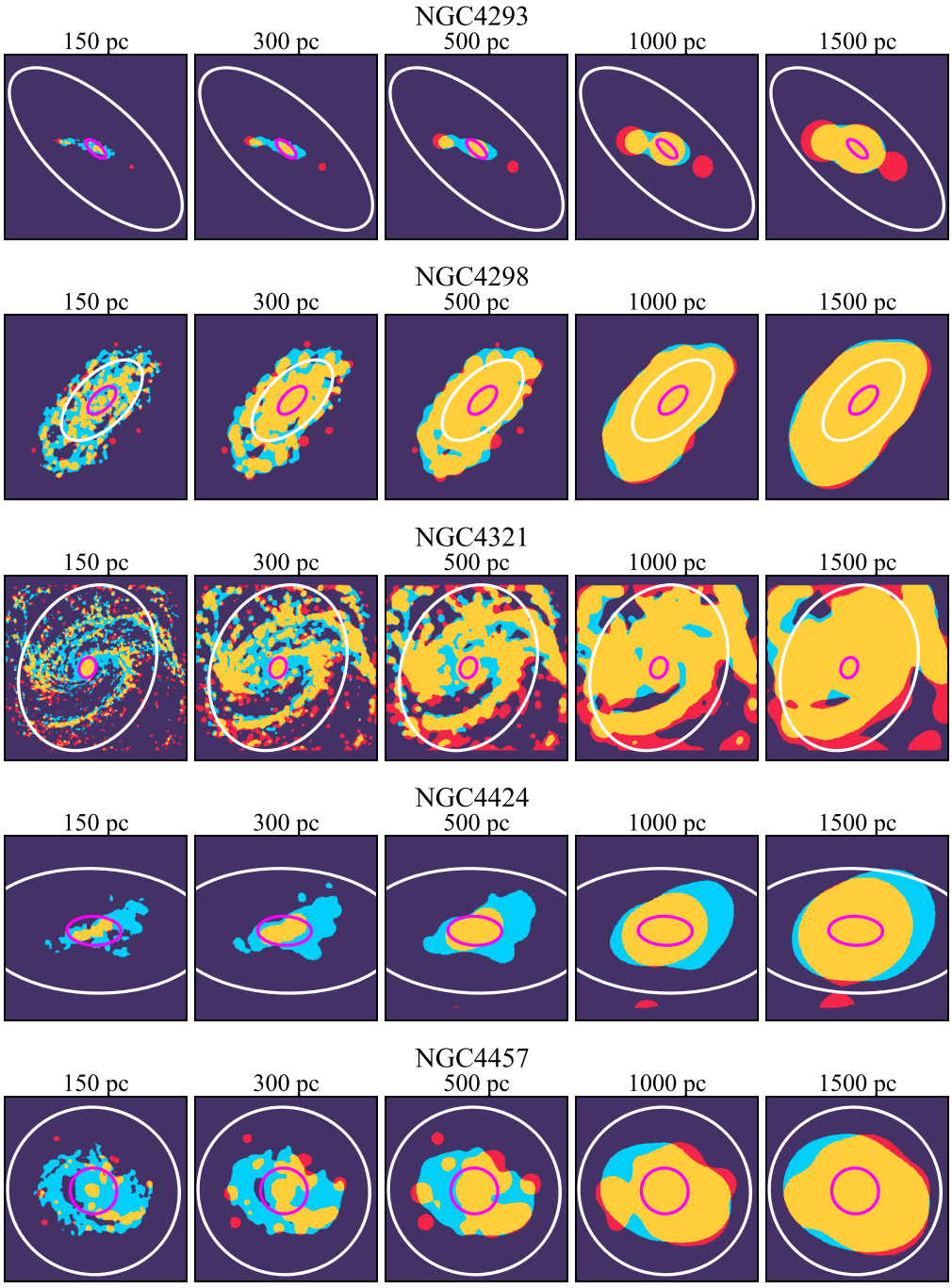

Figure B1. (Continued.)

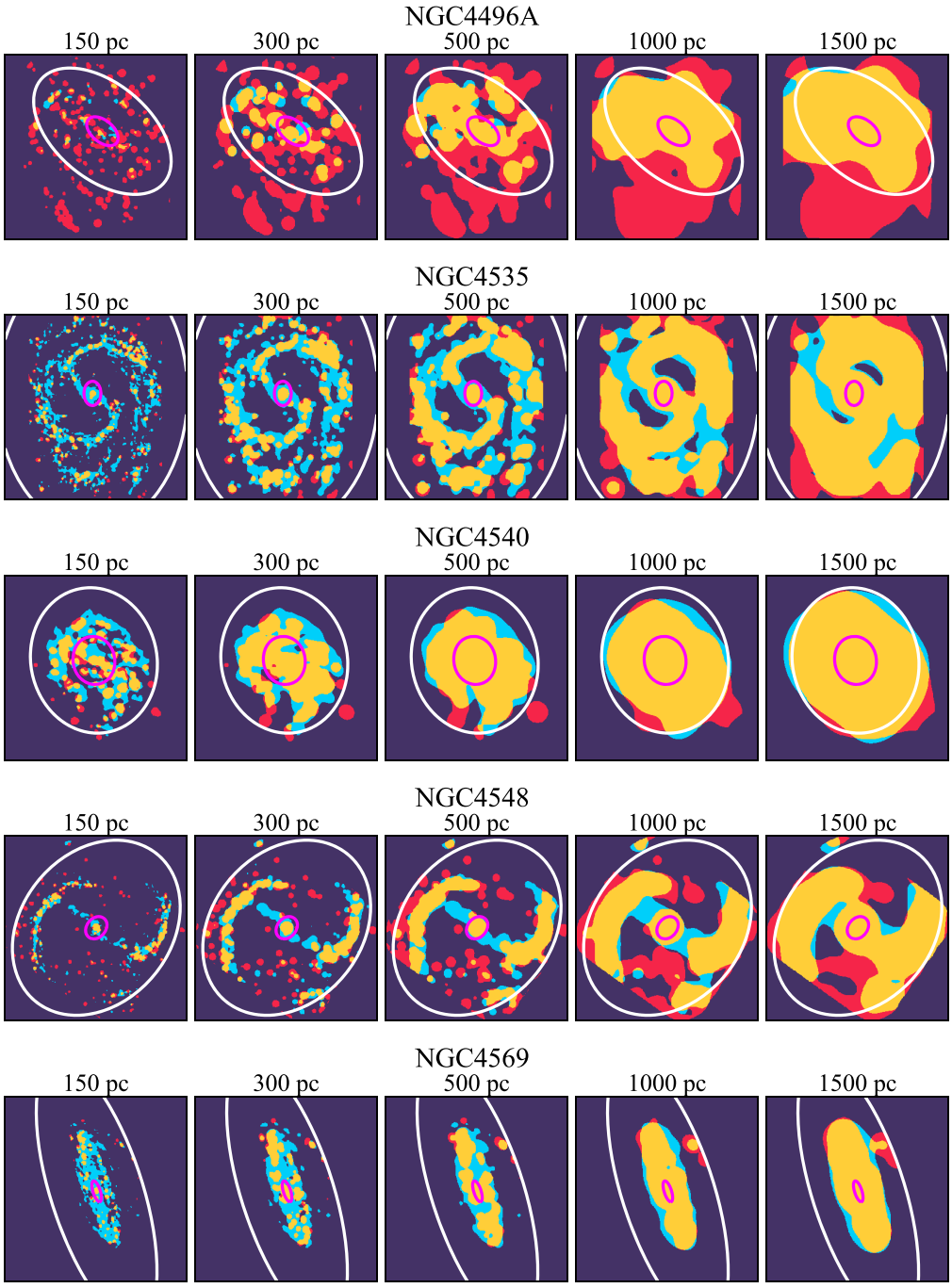

Figure B1. (Continued.)

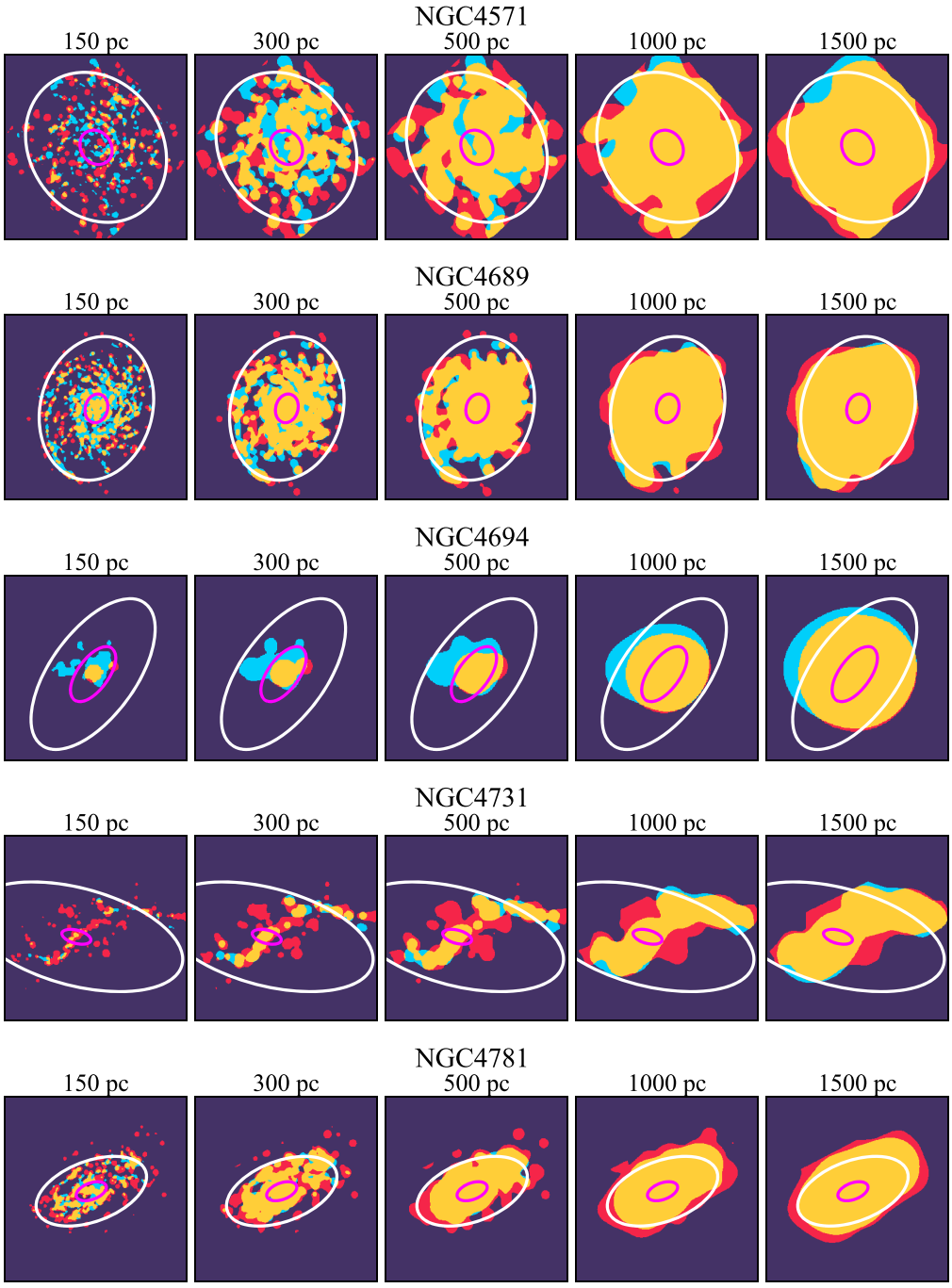

Figure B1. (Continued.)

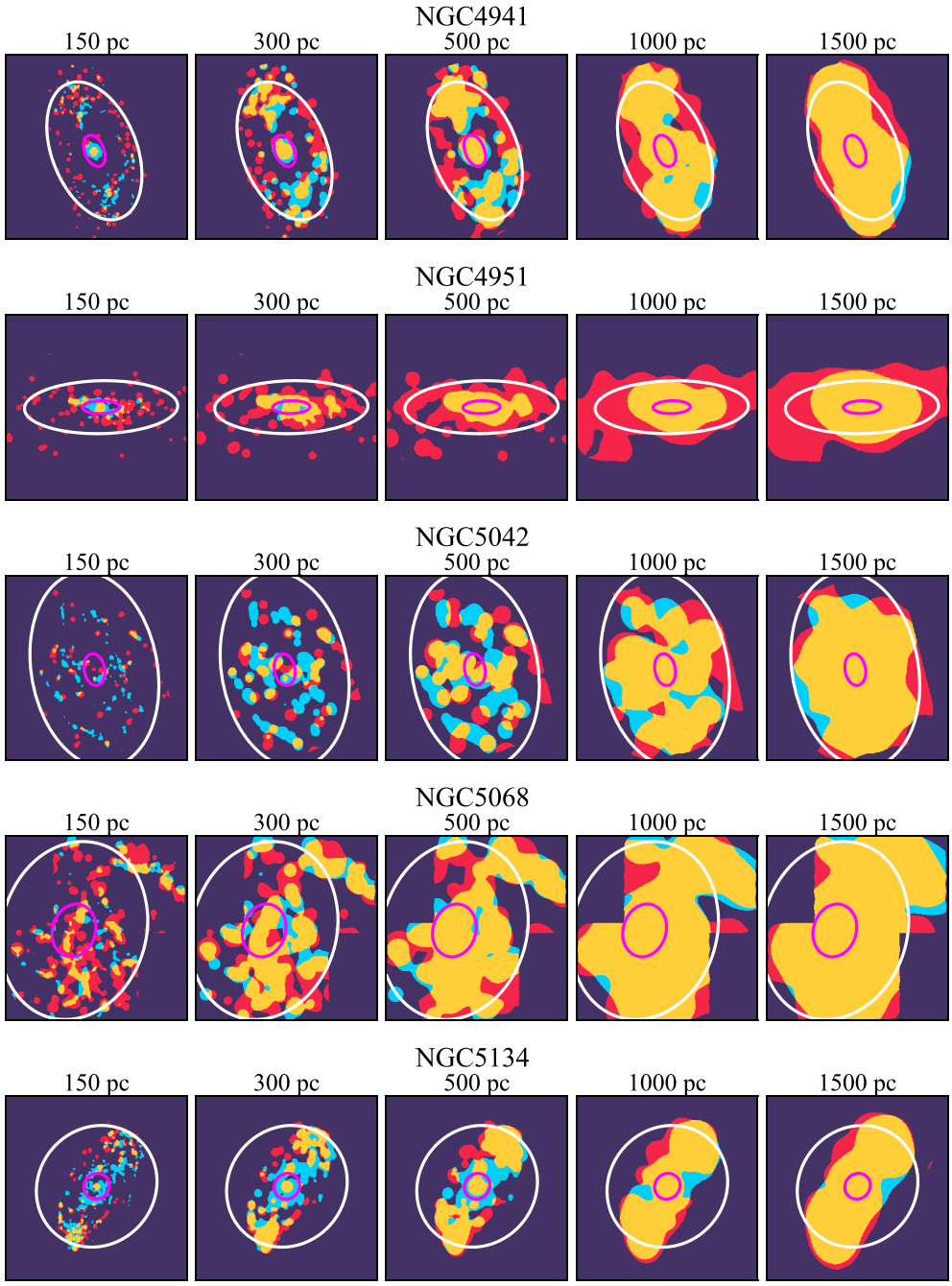

Figure B1. (Continued.)

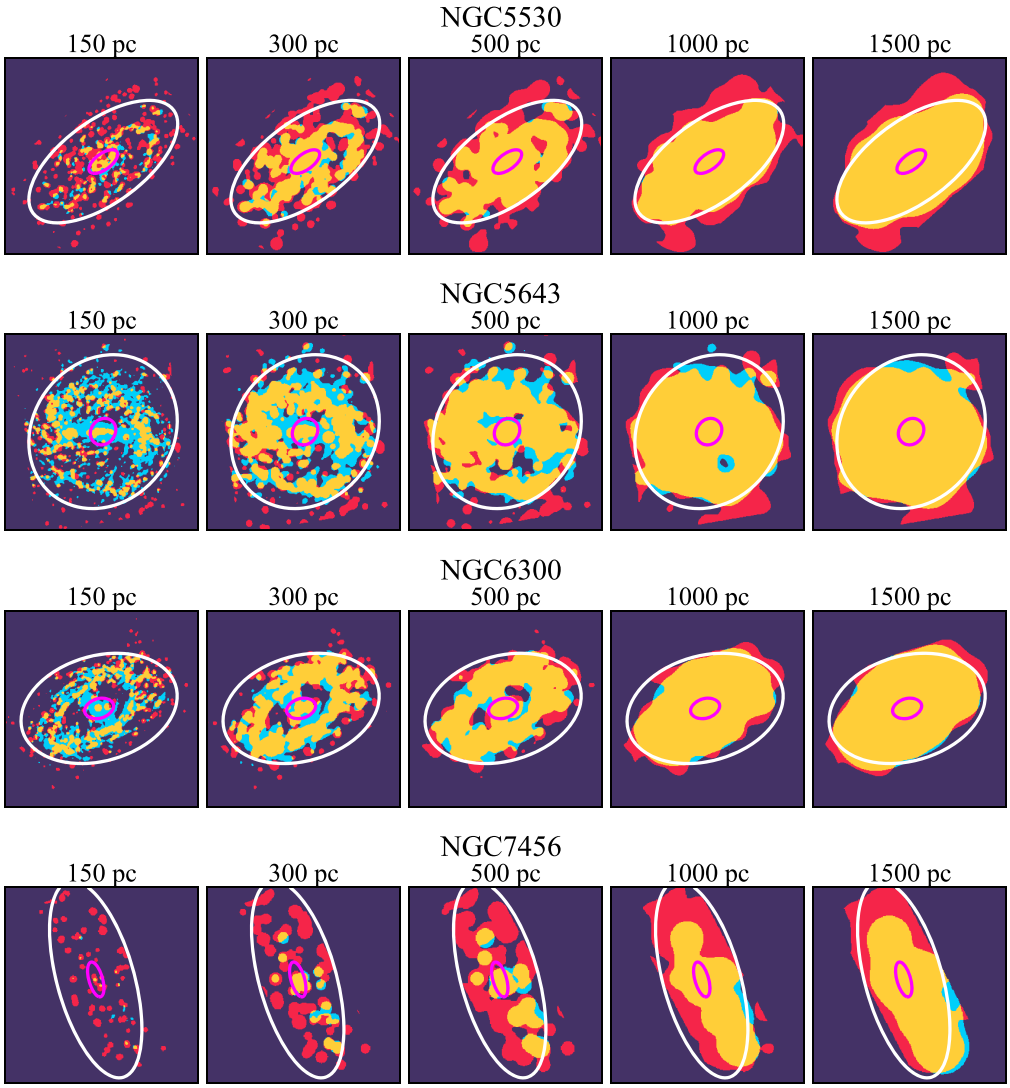

Figure B1. (Continued.)

Table B1
Fractions (%) of Sight Lines (*CO-only*, *Hα-only*, *Overlap*) at 150, 300, 500, 1000, and 1500 pc Resolutions

Galaxy	150 pc	300 pc	500 pc	1000 pc	1500 pc
IC 1954	(19.3, 34.2, 46.5)	(6.1, 19.2, 74.7)	(3.6, 17.0, 79.3)	(0.0, 4.7, 95.3)	(0.0, 0.0, 100.0)
IC 5273	(11.6, 61.0, 27.4)	(8.3, 35.7, 56.1)	(3.9, 23.8, 72.3)	(2.5, 4.9, 92.6)	(1.6, 0.4, 98.1)
NGC 0628	(38.5, 17.7, 43.7)	(24.6, 9.6, 65.8)	(13.7, 7.3, 79.0)	(4.8, 7.0, 88.2)	(1.8, 6.6, 91.6)
NGC 1087	(23.6, 20.7, 55.6)	(8.1, 12.7, 79.2)	(2.0, 9.3, 88.7)	(0.2, 4.2, 95.6)	(0.1, 1.1, 98.8)
NGC 1300	(26.7, 42.1, 31.3)	(14.1, 42.3, 43.6)	(7.8, 41.7, 50.4)	(5.0, 35.8, 59.2)	(4.5, 27.5, 68.0)
NGC 1317	(49.8, 1.7, 48.4)	(30.8, 1.2, 68.0)	(23.8, 0.4, 75.8)	(14.4, 0.0, 85.6)	(9.0, 0.1, 90.9)
NGC 1365	(56.9, 16.4, 26.7)	(40.7, 23.6, 35.6)	(32.4, 25.9, 41.7)	(24.1, 26.9, 49.0)	(19.8, 26.8, 53.4)
NGC 1385	(28.4, 18.7, 52.9)	(12.1, 16.1, 71.8)	(5.7, 12.0, 82.4)	(2.6, 7.8, 89.6)	(2.3, 4.5, 93.3)
NGC 1433	(13.3, 70.6, 16.1)	(9.2, 68.1, 22.7)	(8.0, 63.6, 28.4)	(8.4, 51.3, 40.3)	(8.6, 43.0, 48.4)
NGC 1511	(48.1, 11.7, 40.1)	(29.8, 10.7, 59.4)	(19.5, 7.6, 73.0)	(6.0, 2.5, 91.6)	(2.4, 0.2, 97.5)
NGC 1512	(14.3, 63.0, 22.7)	(11.0, 56.8, 32.2)	(7.2, 54.8, 38.0)	(4.8, 43.6, 51.6)	(4.9, 34.0, 61.1)
NGC 1546	(69.7, 0.2, 30.2)	(48.2, 0.2, 51.7)	(36.9, 0.0, 63.0)	(25.1, 0.0, 74.9)	(16.2, 0.0, 83.8)
NGC 1559	(50.4, 11.6, 38.0)	(22.9, 10.7, 66.4)	(7.5, 8.8, 83.7)	(0.8, 4.7, 94.4)	(0.2, 2.4, 97.5)
NGC 1566	(36.6, 26.5, 36.9)	(22.3, 26.9, 50.8)	(13.7, 28.6, 57.6)	(6.2, 28.9, 64.9)	(3.6, 28.3, 68.1)
NGC 2090	(3.0, 61.4, 35.5)	(0.0, 45.8, 54.1)	(0.0, 45.9, 54.1)	(0.0, 33.0, 67.0)	(0.0, 14.7, 85.3)
NGC 2283	(11.9, 53.2, 34.9)	(5.2, 29.9, 64.9)	(1.5, 20.1, 78.4)	(0.0, 3.6, 96.4)	(0.0, 0.2, 99.8)
NGC 2835	(3.4, 83.4, 13.2)	(2.0, 67.7, 30.3)	(0.7, 61.9, 37.4)	(0.0, 49.9, 50.1)	(0.0, 41.1, 58.9)
NGC 2997	(56.2, 10.8, 33.0)	(35.7, 13.2, 51.1)	(22.3, 15.0, 62.7)	(9.5, 16.0, 74.5)	(3.7, 14.6, 81.8)
NGC 3351	(52.9, 24.4, 22.7)	(42.3, 17.9, 39.8)	(28.6, 15.7, 55.7)	(16.5, 12.4, 71.1)	(8.2, 8.9, 82.9)
NGC 3511	(11.2, 60.1, 28.7)	(5.3, 47.2, 47.4)	(1.5, 41.9, 56.6)	(0.1, 25.1, 74.8)	(0.0, 12.9, 87.1)
NGC 3596	(32.5, 18.8, 48.7)	(9.7, 16.9, 73.5)	(1.6, 15.4, 83.0)	(0.1, 11.6, 88.3)	(0.1, 4.1, 95.8)
NGC 3626	(71.5, 7.2, 21.3)	(22.0, 14.8, 63.2)	(11.4, 12.3, 76.3)	(8.8, 6.3, 85.0)	(8.2, 3.1, 88.7)
NGC 3627	(45.2, 13.3, 41.4)	(27.8, 13.3, 58.9)	(16.1, 12.5, 71.4)	(6.8, 11.2, 82.0)	(4.8, 9.9, 85.2)
NGC 4207	(32.4, 6.0, 61.5)	(16.1, 4.0, 79.9)	(7.4, 1.9, 90.7)	(0.0, 0.0, 100.0)	(0.0, 0.0, 100.0)
NGC 4254	(50.9, 2.4, 46.7)	(29.5, 1.7, 68.8)	(18.0, 1.1, 80.8)	(8.0, 0.9, 91.2)	(4.8, 0.4, 94.9)
NGC 4293	(72.0, 8.2, 19.8)	(52.5, 14.1, 33.4)	(36.5, 20.3, 43.1)	(11.2, 29.0, 59.8)	(1.7, 29.3, 69.1)
NGC 4298	(43.4, 2.9, 53.7)	(14.0, 0.6, 85.4)	(2.0, 0.0, 98.0)	(0.0, 0.0, 100.0)	(0.0, 0.0, 100.0)
NGC 4321	(44.0, 19.7, 36.3)	(29.1, 17.1, 53.8)	(17.2, 16.7, 66.1)	(5.7, 14.2, 80.1)	(1.8, 11.7, 86.6)
NGC 4424	(77.7, 0.2, 22.0)	(74.1, 0.0, 25.9)	(63.6, 0.0, 36.4)	(40.0, 0.1, 59.9)	(24.5, 1.2, 74.3)
NGC 4457	(76.9, 3.3, 19.8)	(55.1, 6.4, 38.6)	(35.7, 10.7, 53.5)	(12.7, 10.2, 77.2)	(8.8, 5.8, 85.3)
NGC 4496A	(6.9, 79.9, 13.2)	(7.9, 54.4, 37.7)	(4.3, 37.5, 58.2)	(1.1, 21.1, 77.8)	(1.0, 13.0, 86.0)
NGC 4535	(65.0, 9.9, 25.1)	(50.0, 8.0, 42.0)	(34.1, 8.9, 57.0)	(15.5, 11.9, 72.6)	(10.1, 12.8, 77.1)
NGC 4540	(46.3, 12.3, 41.5)	(26.0, 6.7, 67.3)	(14.8, 6.2, 79.0)	(8.6, 4.2, 87.2)	(4.1, 1.9, 94.0)
NGC 4548	(37.0, 32.5, 30.5)	(29.4, 28.6, 42.1)	(20.4, 30.5, 49.1)	(12.4, 27.0, 60.6)	(5.2, 19.4, 75.4)
NGC 4569	(74.5, 3.6, 21.9)	(52.0, 5.4, 42.7)	(34.3, 5.2, 60.5)	(16.6, 6.9, 76.5)	(10.2, 7.9, 81.9)
NGC 4571	(29.7, 48.5, 21.8)	(22.7, 22.9, 54.4)	(10.7, 18.6, 70.7)	(3.5, 8.5, 88.0)	(3.2, 3.9, 92.9)
NGC 4689	(35.4, 20.7, 43.9)	(16.5, 14.3, 69.2)	(8.1, 10.2, 81.7)	(1.6, 5.5, 92.9)	(0.3, 2.7, 97.0)
NGC 4694	(69.7, 6.8, 23.5)	(62.6, 4.1, 33.3)	(48.8, 3.1, 48.2)	(19.4, 1.4, 79.3)	(6.0, 1.0, 93.0)
NGC 4731	(5.4, 81.0, 13.7)	(6.8, 58.6, 34.6)	(6.7, 49.4, 43.9)	(4.0, 32.4, 63.7)	(2.4, 19.1, 78.4)
NGC 4781	(14.1, 40.8, 45.2)	(3.9, 27.0, 69.1)	(0.7, 21.4, 77.9)	(0.0, 9.4, 90.6)	(0.0, 0.5, 99.5)
NGC 4941	(33.0, 51.7, 15.3)	(27.6, 36.5, 35.9)	(18.5, 30.1, 51.4)	(5.2, 18.6, 76.2)	(2.0, 9.5, 88.5)
NGC 4951	(17.9, 64.0, 18.2)	(3.3, 60.7, 36.0)	(0.0, 60.8, 39.1)	(0.0, 39.9, 60.1)	(0.0, 21.9, 78.1)
NGC 5042	(47.0, 40.6, 12.4)	(47.9, 26.1, 26.1)	(32.6, 24.1, 43.3)	(12.3, 17.8, 69.9)	(6.4, 11.1, 82.6)
NGC 5068	(10.7, 62.5, 26.8)	(12.9, 30.3, 56.7)	(6.4, 17.9, 75.6)	(2.4, 8.2, 89.4)	(0.5, 5.0, 94.5)
NGC 5134	(49.2, 25.4, 25.4)	(40.1, 17.3, 42.6)	(26.6, 16.8, 56.6)	(9.1, 13.5, 77.4)	(4.1, 10.4, 85.5)
NGC 5530	(11.5, 59.3, 29.2)	(6.3, 33.2, 60.5)	(1.2, 22.5, 76.2)	(0.1, 8.3, 91.7)	(0.0, 1.2, 98.8)
NGC 5643	(51.4, 11.2, 37.5)	(30.6, 8.5, 60.9)	(15.6, 6.4, 78.0)	(5.9, 3.5, 90.6)	(3.5, 2.3, 94.2)
NGC 6300	(40.6, 19.1, 40.4)	(19.8, 16.4, 63.9)	(8.5, 15.4, 76.1)	(1.7, 8.0, 90.3)	(1.0, 3.4, 95.5)
NGC 7456	(2.6, 93.3, 4.1)	(5.6, 72.3, 22.1)	(4.4, 63.4, 32.1)	(1.8, 43.4, 54.8)	(0.6, 29.0, 70.4)

Appendix C
Sight-line Fractions versus Properties of Galaxies and Observations

Here we present the scatter plots of the galaxy and observational properties against the three sight-line fractions in Figure C1. The properties we explore are (a) stellar mass, (b) Hubble type, (c) galaxy distance, (d) optical size indicated by R_{25}, (e) disk inclination, (f) effective H II region sensitivity ($\log(L_{\mathrm{H\,II\ region}}^{\mathrm{sensitivity}})$, Section 3.1, (g) native resolutions of Hα observation, (h) DIG fraction, (i) effective sensitivity of CO observation (1σ sensitivity in $\Sigma_{\mathrm{H_2}}$ at 150 pc resolution), (j) native resolution of CO observation, (k) specific SFR (sSFR), and (l) offset from the star-forming main sequence, ΔMS. The discussion can be found in the main text in Section 4.1.1. The correlation coefficients of each relation shown in Figure C1 are provided in Table 5 in the main text.

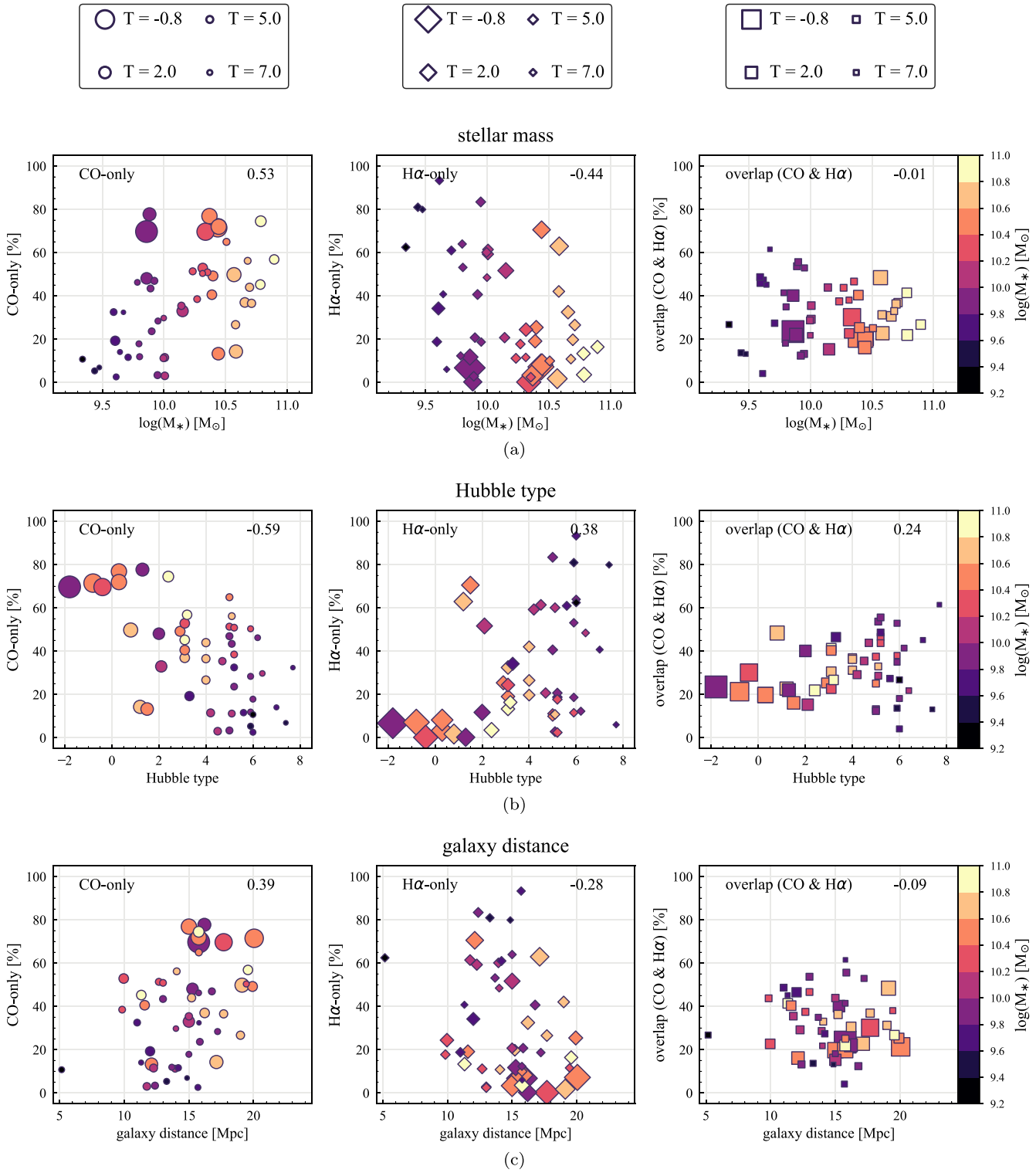

Figure C1. Sight-line fractions as a function of (a) stellar mass, (b) Hubble type, (c) galaxy distance, (d) optical size indicated by R_{25}, (e) disk inclination, (f) effective H II region sensitivity ($\log(L_{\rm H\,II\,region}^{\rm sensitivity})$, Section 3.1, (g) DIG fraction, (h) native resolutions of the Hα observation, (i) effective sensitivity of the CO observation (1σ sensitivity in $\Sigma_{\rm H_2}$ at 150 pc resolution), (j) native resolution of the CO observation, (k) specific SFR, and (l) offset from the star-forming main sequence, ΔMS. Galaxies are color-coded by M_*. The symbol size indicates Hubble type, with larger symbols for earlier types. Examples of symbol sizes for different Hubble types are given in the top rows. The correlation coefficient of each pair of properties is given in the upper-right corner of each plot.

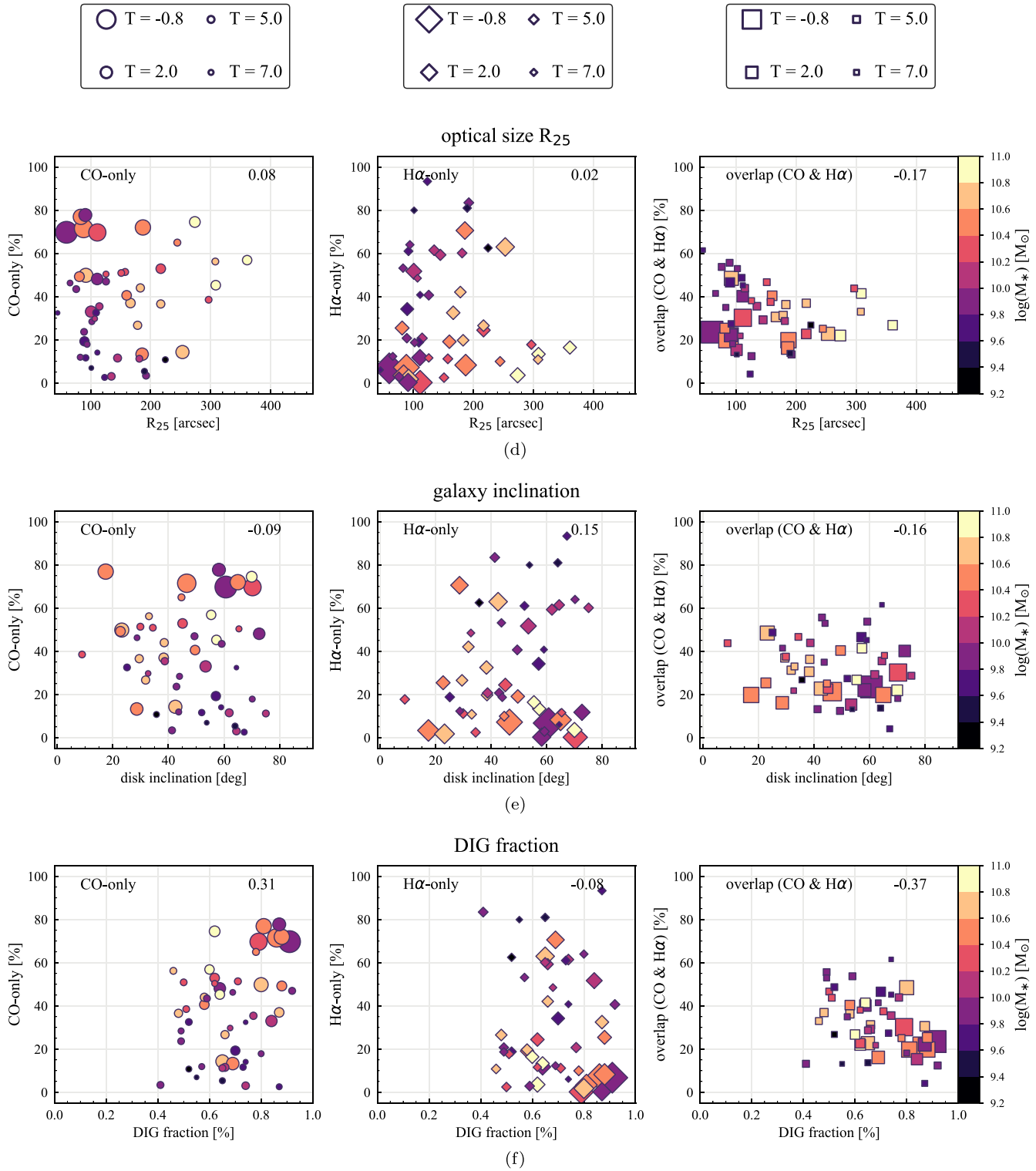

Figure C1. (Continued.)

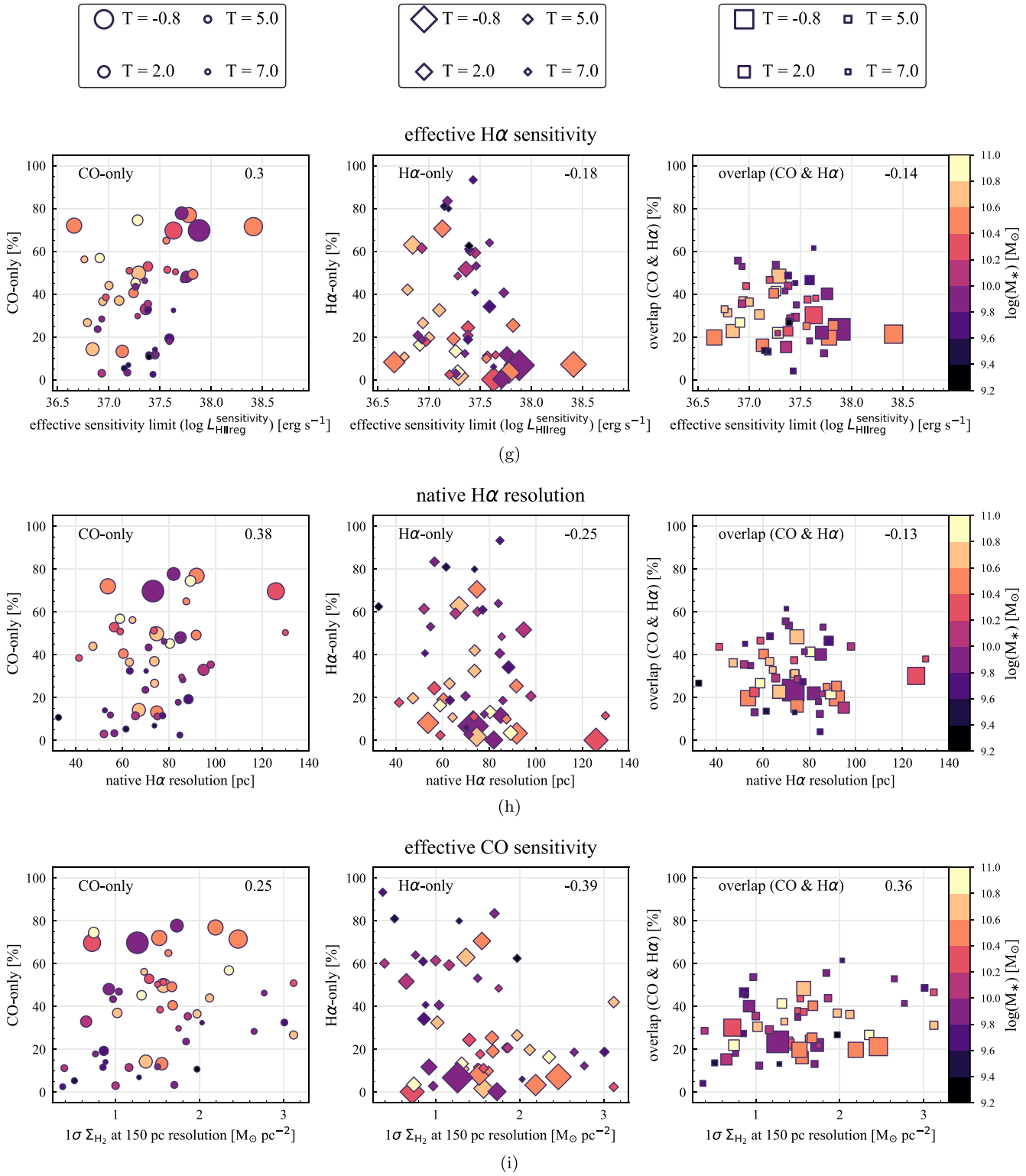

Figure C1. (Continued.)

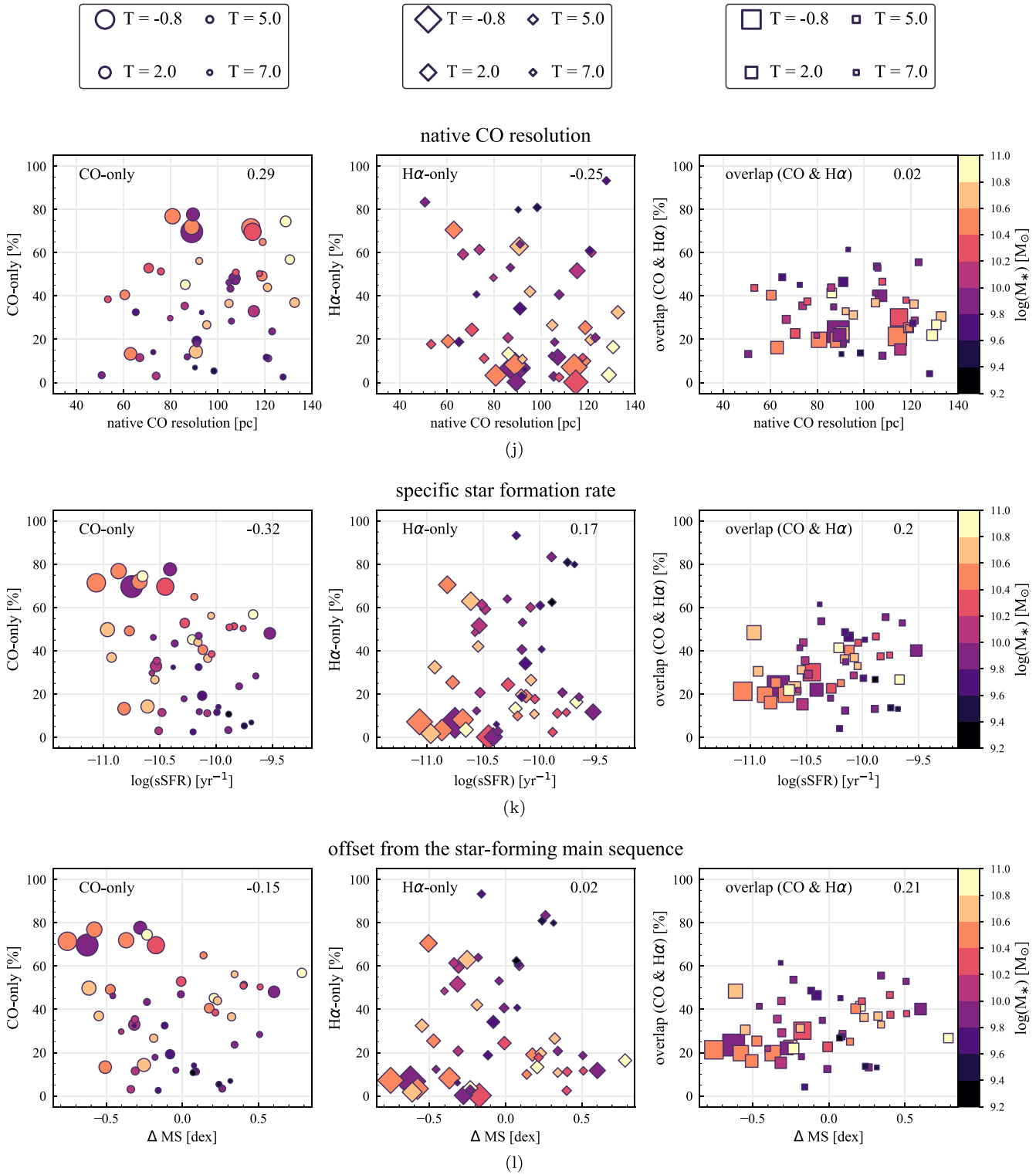

Figure C1. (Continued.)

Appendix D
Comparison of Cloud Visibility Time with Chevance et al. (2020)

Here we directly compare the radial variation in the cloud visibility time derived from our analysis ($t_{\rm gas}$) with the GMC lifetime during which CO is visible ($t_{\rm GMC}$) measured by Chevance et al. (2020) for the seven galaxies analyzed in both studies. The results from the two studies are compared in Figure D1. Overall, the two studies show similar results, particularly in regard to the absolute $t_{\rm gas}$ (or $t_{\rm GMC}$) for most radial bins. The relative $t_{\rm gas}$ (or $t_{\rm GMC}$) among different galaxies also shows reasonable agreement. The robustness to the

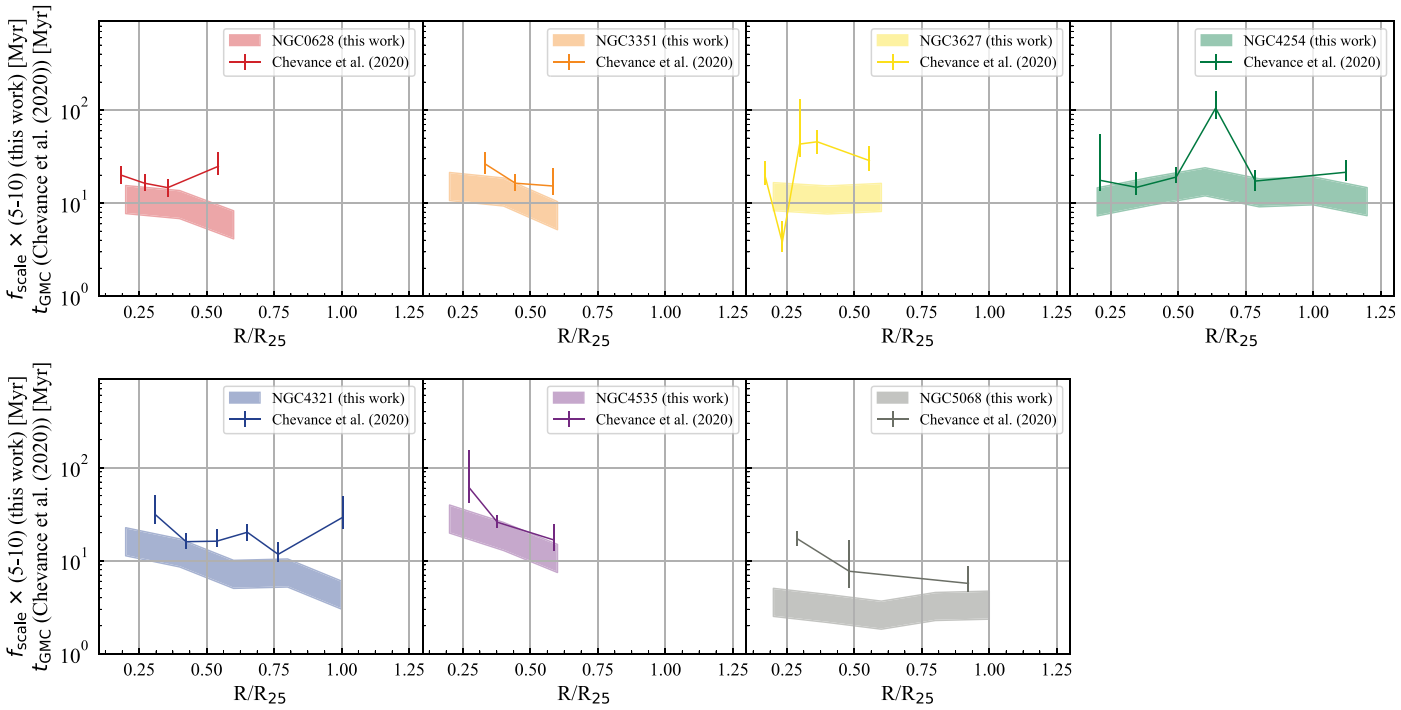

Figure D1. Comparison of our radial cloud visibility time ($t_{gas} = f_{scale} \times t_{H\alpha}$) (thick shaded curve) with the GMC lifetime during which CO is visible (t_{GMC}) measured by Chevance et al. (2020) (thin curve with error bars). In this work, we assume the fiducial timescale $t_{H\alpha}$ to be 5–10 Myr. Note that the radial bins adopted by the two studies are slightly different.

adopted methodology suggests that both results indeed reflect the visibility time of the molecular cloud traced by CO emission. Larger discrepancies are seen in regions where the emission (either CO or Hα) is relatively sparse and/or weak, such as the larger-radius and lower-M_* galaxy (NGC 5068), suggesting that the sensitivity and completeness of the observation are important factors in estimating the cloud visibility time.

ORCID iDs

Hsi-An Pan (潘璽安) https://orcid.org/0000-0002-1370-6964
Eva Schinnerer https://orcid.org/0000-0002-3933-7677
Annie Hughes https://orcid.org/0000-0002-9181-1161
Adam Leroy https://orcid.org/0000-0002-2545-1700
Brent Groves https://orcid.org/0000-0002-9768-0246
Ashley Thomas Barnes https://orcid.org/0000-0003-0410-4504
Francesco Belfiore https://orcid.org/0000-0002-2545-5752
Frank Bigiel https://orcid.org/0000-0003-0166-9745
Guillermo A. Blanc https://orcid.org/0000-0003-4218-3944
Yixian Cao https://orcid.org/0000-0001-5301-1326
Mélanie Chevance https://orcid.org/0000-0002-5635-5180
Enrico Congiu https://orcid.org/0000-0002-8549-4083
Daniel A. Dale https://orcid.org/0000-0002-5782-9093
Eric Emsellem https://orcid.org/0000-0002-6155-7166
Christopher M. Faesi https://orcid.org/0000-0001-5310-467X
Simon C. O. Glover https://orcid.org/0000-0001-6708-1317
Kathryn Grasha https://orcid.org/0000-0002-3247-5321
I-Ting Ho https://orcid.org/0000-0002-0757-9559
Ralf S. Klessen https://orcid.org/0000-0002-0560-3172
J. M. Diederik Kruijssen https://orcid.org/0000-0002-8804-0212
Philipp Lang https://orcid.org/0000-0002-5681-3575
Daizhong Liu https://orcid.org/0000-0001-9773-7479
Sharon E. Meidt https://orcid.org/0000-0002-6118-4048
Eric J. Murphy https://orcid.org/0000-0001-7089-7325
Jérôme Pety https://orcid.org/0000-0003-3061-6546
Miguel Querejeta https://orcid.org/0000-0002-0472-1011
Erik Rosolowsky https://orcid.org/0000-0002-5204-2259
Toshiki Saito https://orcid.org/0000-0002-2501-9328
Francesco Santoro https://orcid.org/0000-0002-6363-9851
Jiayi Sun https://orcid.org/0000-0003-0378-4667
Neven Tomičić https://orcid.org/0000-0002-8238-9210
Antonio Usero https://orcid.org/0000-0003-1242-505X
Dyas Utomo https://orcid.org/0000-0003-4161-2639
Thomas G. Williams https://orcid.org/0000-0002-0012-2142

References

Accurso, G., Saintonge, A., Catinella, B., et al. 2017, MNRAS, 470, 4750
Anand, G. S., Lee, J. C., Van Dyk, S. D., et al. 2021, MNRAS, 501, 3621
Arimoto, N., Sofue, Y., & Tsujimoto, T. 1996, PASJ, 48, 275
Asplund, M., Grevesse, N., Sauval, A. J., et al. 2009, ARA&A, 47, 481
Azimlu, M., Marciniak, R., & Barmby, P. 2011, AJ, 142, 139
Baldwin, J. A., Phillips, M. M., & Terlevich, R. 1981, PASP, 93, 5
Barnes, A. T., Glover, S. C. O., Kreckel, K., et al. 2021, MNRAS, 508, 5362
Barnes, A. T., Longmore, S. N., Dale, J. E., et al. 2020, MNRAS, 498, 4906
Battersby, C., Bally, J., & Svoboda, B. 2017, ApJ, 835, 263
Belfiore, F., Maiolino, R., Maraston, C., et al. 2016, MNRAS, 461, 3111
Belfiore, F., Santoro, F., Groves, B., et al. 2021, arXiv:2111.14876
Beuther, H., Meidt, S., Schinnerer, E., et al. 2017, A&A, 597, A85
Bigiel, F., Leroy, A., Walter, F., et al. 2008, AJ, 136, 2846
Blanc, G. A., Heiderman, A., Gebhardt, K., et al. 2009, ApJ, 704, 842
Bolatto, A. D., Wolfire, M., & Leroy, A. K. 2013, ARA&A, 51, 207
Bradley, T. R., Knapen, J. H., Beckman, J. E., et al. 2006, A&A, 459, L13
Brinchmann, J., Charlot, S., White, S. D. M., et al. 2004, MNRAS, 351, 1151
Buta, R. J., Sheth, K., Athanassoula, E., et al. 2015, ApJS, 217, 32
Calzetti, D., Kennicutt, R. C., Engelbracht, C. W., et al. 2007, ApJ, 666, 870
Carles, C., Martel, H., Ellison, S. L., et al. 2016, MNRAS, 463, 1074
Catinella, B., Saintonge, A., Janowiecki, S., et al. 2018, MNRAS, 476, 875

Chevance, M., Kruijssen, J. M. D., Hygate, A. P. S., et al. 2020, MNRAS, 493, 2872
Chevance, M., Kruijssen, J. M. D., Krumholz, M. R., et al. 2022, MNRAS, 509, 272
Chung, A., van Gorkom, J. H., Kenney, J. D. P., et al. 2009, AJ, 138, 1741
Colombo, D., Hughes, A., Schinnerer, E., et al. 2014, ApJ, 784, 3
Colombo, D., Kalinova, V., Utomo, D., et al. 2018, MNRAS, 475, 1791
Corbelli, E., Braine, J., Bandiera, R., et al. 2017, A&A, 601, A146
Crocker, A. F., Bureau, M., Young, L. M., et al. 2011, MNRAS, 410, 1197
Davis, T. A., Young, L. M., Crocker, A. F., et al. 2014, MNRAS, 444, 3427
den Brok, J. S., Chatzigiannakis, D., Bigiel, F., et al. 2021, MNRAS, 504, 3221
Díaz-García, S., Moyano, F. D., Comerón, S., et al. 2020, A&A, 644, A38
Donohoe-Keyes, C. E., Martig, M., James, P. A., et al. 2019, MNRAS, 489, 4992
Egusa, F., Kohno, K., Sofue, Y., et al. 2009, ApJ, 697, 1870
Egusa, F., Sofue, Y., & Nakanishi, H. 2004, PASJ, 56, L45
Ellison, S. L., Viswanathan, A., Patton, D. R., et al. 2019, MNRAS, 487, 2491
Emsellem, E., Schinnerer, E., Santoro, F., et al. 2021, arXiv:2110.03708
Engargiola, G., Plambeck, R. L., Rosolowsky, E., et al. 2003, ApJS, 149, 343
Feldmann, R., Gnedin, N. Y., & Kravtsov, A. V. 2011, ApJ, 732, 115
Fitzpatrick, E. L. 1999, PASP, 111, 63
Gaia Collaboration, Brown, A. G. A., Vallenari, A., et al. 2018, A&A, 616, A1
González Delgado, R. M., García-Benito, R., Pérez, E., et al. 2015, A&A, 581, A103
Gratier, P., Braine, J., Rodriguez-Fernandez, N. J., et al. 2012, A&A, 542, A108
Haffner, L. M., Dettmar, R.-J., Beckman, J. E., et al. 2009, RvMP, 81, 969
Haydon, D. T., Kruijssen, J. M. D., Chevance, M., et al. 2020, MNRAS, 498, 235
Herrera-Endoqui, M., Díaz-García, S., Laurikainen, E., et al. 2015, A&A, 582, A86
Hilmi, T., Minchev, I., Buck, T., et al. 2020, MNRAS, 497, 933
Hoopes, C. G., & Walterbos, R. A. M. 2003, ApJ, 586, 902
Hoopes, C. G., Walterbos, R. A. M., & Rand, R. J. 1999, ApJ, 522, 669
Hsieh, B. C., Lin, L., Lin, J. H., et al. 2017, ApJL, 851, L24
Hughes, A., Meidt, S. E., Colombo, D., et al. 2013, ApJ, 779, 46
Indebetouw, R., Whitney, B. A., Kawamura, A., et al. 2008, AJ, 136, 1442
James, P. A., Bretherton, C. F., & Knapen, J. H. 2009, A&A, 501, 207
Jeffreson, S. M. R., Keller, B. W., Winter, A. J., et al. 2021, MNRAS, 505, 1678
Jeffreson, S. M. R., & Kruijssen, J. M. D. 2018, MNRAS, 476, 3688
Jeffreson, S. M. R., Kruijssen, J. M. D., Keller, B. W., et al. 2020, MNRAS, 498, 385
Katz, N. 1992, ApJ, 391, 502
Kawamura, A., Mizuno, Y., Minamidani, T., et al. 2009, ApJS, 184, 1
Kelvin, L. S., Driver, S. P., Robotham, A. S. G., et al. 2014, MNRAS, 444, 1647
Kennicutt, R. C. 1998, ARA&A, 36, 189
Kennicutt, R. C., & Evans, N. J. 2012, ARA&A, 50, 531
Kim, E., Hwang, H. S., Chung, H., et al. 2017, ApJ, 845, 93
Kim, J., Chevance, M., Kruijssen, J. M. D., et al. 2021, MNRAS, 504, 487
Klessen, R. S., & Hennebelle, P. 2010, A&A, 520, A17
Kreckel, K., Blanc, G. A., Schinnerer, E., et al. 2016, ApJ, 827, 103
Kreckel, K., Faesi, C., Kruijssen, J. M. D., et al. 2018, ApJL, 863, L21
Kruijssen, J. M. D., & Longmore, S. N. 2014, MNRAS, 439, 3239
Kruijssen, J. M. D., Schruba, A., Chevance, M., et al. 2019, Natur, 569, 519
Kruijssen, J. M. D., Schruba, A., Hygate, A. P. S., et al. 2018, MNRAS, 479, 1866
Lacerda, E. A. D., Cid Fernandes, R., Couto, G. S., et al. 2018, MNRAS, 474, 3727
Laine, J., Laurikainen, E., & Salo, H. 2016, A&A, 596, A25
Lang, P., Meidt, S. E., Rosolowsky, E., et al. 2020, ApJ, 897, 122
Lee, J. C., Whitmore, B. C., Thilker, D. A., et al. 2022, ApJS, 258, 10
Leroy, A. K., Bigiel, F., de Blok, W. J. G., et al. 2012, AJ, 144, 3
Leroy, A. K., Bolatto, A., Gordon, K., et al. 2011, ApJ, 737, 12
Leroy, A. K., Hughes, A., Liu, D., et al. 2021a, ApJS, 255, 19
Leroy, A. K., Rosolowsky, E., Usero, A., et al. 2021b, arXiv:2109.11583
Leroy, A. K., Sandstrom, K. M., Lang, D., et al. 2019, ApJS, 244, 24
Leroy, A. K., Schinnerer, E., Hughes, A., et al. 2021c, ApJS, 257, 43
Leroy, A. K., Walter, F., Brinks, E., et al. 2008, AJ, 136, 2782
Leroy, A. K., Walter, F., Sandstrom, K., et al. 2013, AJ, 146, 19
Louie, M., Koda, J., & Egusa, F. 2013, ApJ, 763, 94
Mac Low, M.-M., & Klessen, R. S. 2004, RvMP, 76, 125
Martinet, L., & Friedli, D. 1997, A&A, 323, 363
McKee, C. F., & Ostriker, E. C. 2007, ARA&A, 45, 565
McMullin, J. P., Waters, B., Schiebel, D., et al. 2007, in Astronomical Data Analysis Software and Systems XVI ASP Conf. Ser. 376 (San Francisco, CA: ASP), 127
Meidt, S. E., Leroy, A. K., Rosolowsky, E., et al. 2018, ApJ, 854, 100
Meidt, S. E., Rand, R. J., & Merrifield, M. R. 2009, ApJ, 702, 277
Meidt, S. E., Schinnerer, E., García-Burillo, S., et al. 2013, ApJ, 779, 45
Menéndez-Delmestre, K., Sheth, K., Schinnerer, E., et al. 2007, ApJ, 657, 790
Mizuno, N., Rubio, M., Mizuno, A., et al. 2001, PASJ, 53, L45
Momose, R., Koda, J., Kennicutt, R. C., et al. 2013, ApJL, 772, L13
Oey, M. S., Meurer, G. R., Yelda, S., et al. 2007, ApJ, 661, 801
Oey, M. S., Parker, J. S., Mikles, V. J., et al. 2003, AJ, 126, 2317
Onodera, S., Kuno, N., Tosaki, T., et al. 2010, ApJL, 722, L127
Pan, H.-A., & Kuno, N. 2017, ApJ, 839, 133
Pan, H.-A., Lin, L., Hsieh, B.-C., et al. 2018, ApJ, 854, 159
Pessa, I., Schinnerer, E., Belfiore, F., et al. 2021, A&A, 650, A134
Pettini, M., & Pagel, B. E. J. 2004, MNRAS, 348, L59
Pety, J., Schinnerer, E., Leroy, A. K., et al. 2013, ApJ, 779, 43
Pour-Imani, H., Kennefick, D., Kennefick, J., et al. 2016, ApJL, 827, L2
Querejeta, M., Schinnerer, E., Meidt, S., et al. 2021, A&A, 656, A133
Querejeta, M., Schinnerer, E., Schruba, A., et al. 2019, A&A, 625, A19
Reynaud, D., & Downes, D. 1998, A&A, 337, 671
Rosolowsky, E., Hughes, A., Leroy, A. K., et al. 2021, MNRAS, 502, 1218
Rousseau-Nepton, L., Robert, C., Martin, R. P., et al. 2018, MNRAS, 477, 4152
Saintonge, A., Catinella, B., Cortese, L., et al. 2016, MNRAS, 462, 1749
Saintonge, A., Catinella, B., Tacconi, L. J., et al. 2017, ApJS, 233, 22
Saintonge, A., Kauffmann, G., Kramer, C., et al. 2011, MNRAS, 415, 32
Sakamoto, K., Okumura, S. K., Ishizuki, S., et al. 1999, ApJ, 525, 691
Sakamoto, S., Hasegawa, T., Handa, T., et al. 1997, ApJ, 486, 276
Sakamoto, S., Hayashi, M., Hasegawa, T., et al. 1994, ApJ, 425, 641
Salim, S., Rich, R. M., Charlot, S., et al. 2007, ApJS, 173, 267
Sánchez, S. F., Barrera-Ballesteros, J. K., López-Cobá, C., et al. 2019, MNRAS, 484, 3042
Sánchez, S. F., Kennicutt, R. C., Gil de Paz, A., et al. 2012, A&A, 538, A8
Sánchez, S. F., Rosales-Ortega, F. F., Iglesias-Páramo, J., et al. 2014, A&A, 563, A49
Santoro, F., Kreckel, K., Belfiore, F., et al. 2021, arXiv:2111.09362
Schaye, J., Crain, R. A., Bower, R. G., et al. 2015, MNRAS, 446, 521
Scheuermann, F., Kreckel, K., Anand, G. S., et al. 2022, MNRAS, in press
Schinnerer, E., Hughes, A., Leroy, A., et al. 2019, ApJ, 887, 49
Schinnerer, E., Meidt, S. E., Pety, J., et al. 2013, ApJ, 779, 42
Schlafly, E. F., & Finkbeiner, D. P. 2011, ApJ, 737, 103
Schmidt, M. 1959, ApJ, 129, 243
Schruba, A., Kruijssen, J. M. D., & Leroy, A. K. 2019, ApJ, 883, 2
Schruba, A., Leroy, A. K., Walter, F., et al. 2010, ApJ, 722, 1699
Schruba, A., Leroy, A. K., Walter, F., et al. 2011, AJ, 142, 37
Schruba, A., Leroy, A. K., Walter, F., et al. 2012, AJ, 143, 138
Sheth, K., Vogel, S. N., Regan, M. W., et al. 2005, ApJ, 632, 217
Sun, J., Leroy, A. K., Ostriker, E. C., et al. 2020a, ApJ, 892, 148
Sun, J., Leroy, A. K., Schinnerer, E., et al. 2020b, ApJL, 901, 8
Teyssier, R. 2002, A&A, 385, 337
Tomičić, N., Ho, I.-T., Kreckel, K., et al. 2019, ApJ, 873, 3
Tomičić, N., Kreckel, K., Groves, B., et al. 2017, ApJ, 844, 155
Tomičić, N., Vulcani, B., Poggianti, B. M., et al. 2021, ApJ, 907, 22
Utomo, D., Sun, J., Leroy, A. K., et al. 2018, ApJL, 861, L18
Verley, S., Combes, F., Verdes-Montenegro, L., et al. 2007, A&A, 474, 43
Walter, F., Brinks, E., de Blok, W. J. G., et al. 2008, AJ, 136, 2563
Whitmore, B. C., Chandar, R., Kim, H., et al. 2011, ApJ, 729, 78
Wilson, C. D. 1995, ApJL, 448, L97
Wolfire, M. G., Hollenbach, D., & McKee, C. F. 2010, ApJ, 716, 1191
Yajima, Y., Sorai, K., Miyamoto, Y., et al. 2021, PASJ, 73, 257
Zhang, K., Yan, R., Bundy, K., et al. 2017, MNRAS, 466, 3217
Zurita, A., Relaño, M., Beckman, J. E., et al. 2004, A&A, 413, 73